ON THE ROLE OF INTERNAL ATMOSPHERIC VARIABILITY IN ENSO DYNAMICS

A Dissertation

by

LI ZHANG

Submitted to the Office of Graduate Studies of
Texas A&M University
in partial fulfillment of the requirements for the degree of

DOCTOR OF PHILOSOPHY

August 2005

Major Subject: Oceanography

ON THE ROLE OF INTERNAL ATMOSPHERIC VARIABILITY IN ENSO DYNAMICS

A Dissertation

by

LI ZHANG

Submitted to the Office of Graduate Studies of
Texas A&M University
in partial fulfillment of the requirements for the degree of

DOCTOR OF PHILOSOPHY

Approved by:

Chair of Committee,	Ping Chang
Committee Members,	Benjamin Giese
	Gerald North
	M. Cécile Penland
	R. Saravanan
Head of Department,	Wilford D. Gardner

August 2005

Major Subject: Oceanography

ABSTRACT

On the Role of Internal Atmospheric Variability
in ENSO Dynamics. (August 2005)
Li Zhang, B.S., Peking University
Chair of Advisory Committee: Dr. Ping Chang

In the first part of this dissertation we use an Intermediate Coupled Model to develop a quantitative test to validate the null hypothesis that low-frequency variation of ENSO predictability may be caused by stochastic processes. Three "perfect model scenario" prediction experiments are carried out, where the model is forced either solely by stochastic forcing or additionally by decadal-varying backgrounds with different amplitudes. These experiments indicate that one can not simply reject the null hypothesis unless the decadal-varying backgrounds are unrealistically strong.

The second part of this dissertation investigates the extent to which internal atmospheric variability (IAV) can influence ENSO variation, and examines the underlying physical mechanisms linking IAV to ENSO variability with the aid of a newly developed coupled model consisting of an atmospheric general circulation model and a Zebiak-Cane type of reduced gravity ocean model. A novel noise filter algorithm is developed to suppress IAV in the coupled model.

A long control coupled simulation, where the filter is not employed, demonstrates that the coupled model captures many statistical properties of the observed ENSO behavior. It further shows that the development of El Niño is linked to a boreal spring phenomenon referred to as the Pacific Meridional Model (MM). The MM, characterized by an anomalous north-south SST gradient and anomalous surface circulation in the northeasterly trade regime with maximum variance in boreal spring, is inherent

to thermodynamic ocean-atmosphere coupling in the Intertropical Convergence Zone latitude. The Northern Pacific Oscillation provides one source of external forcing to excite it. This result supports the hypothesis that the MM works as a conduit for extratropical atmospheric influence on ENSO.

A set of coupled simulations, where the filter is used to suppress IAV, indicate that reducing IAV in both wind stress and heat flux substantially weakens ENSO variance. Furthermore, the resultant ENSO cycle becomes more regular and no longer shows strong seasonal phase locking. The seasonal phase locking of ENSO is strongly tied to the IAV in surface heat flux. The ENSO cycle is strongly tied to IAV in surface wind stress.

ACKNOWLEDGMENTS

First, I would like to thank my advisor Dr. Ping Chang, for his guidance, encouragement, patience and generosity over these last few years. Without his perceptive insight into the topic of this project, this dissertation might never have come into being, and certainly not in its present form. His passion and curiosity about science, and his responsible attitude towards scientific research have inspired me and benefited my research.

Second, I would like to thank my other committee members: Dr. Moritz Flügel for his guidance and support during the early period of my study; Dr. Cécile Penland and Dr. Saravanan for their warm encouragements, mathematical and statistical skills; Dr. Ben Giese and Dr. Gerald North for their inspiring discussions and useful suggestions.

I would also like to thank Dr. Ji Link for her help with computer programming, and Dr. Hank Seidel for his technical support. He also carefully read my manuscript and corrected my English grammar.

In the midst of my research, my son unexpectedly arrived into the world and added excitement and challenge, but mostly joy to my daily life.

Last but foremost, I am indebted to my parents and my husband. My parents came here from China to offer their help in taking care of my baby son. Without their emotional support and unconditional love, I feel there would have been no way for me to finish this work on time.

TABLE OF CONTENTS

CHAPTER Page

LIST OF FIGURES

FIGURE Page

FIGURE Page

FIGURE Page

FIGURE Page

FIGURE Page

CHAPTER I

INTRODUCTION

A. Motivation

The El Niño/Southern Oscillation (ENSO) has long been recognized as the most important climate phenomenon on interannual time scales. Although ENSO originates in the tropical Pacific Ocean, it affects the global climate through atmospheric teleconnections, which in turn impacts the economies of various countries (Philander, 1999). A comprehensive understanding of ENSO and its predictability is therefore of both scientific and practical interest. Over the past three decades, considerable progress has been made in our understanding of ENSO. Nevertheless, there are still some fundamental issues that are not well understood. Among them are two issues that have been the subject of considerable recent debate:

1. The cause of decadal ENSO modulation: The occurrence and strength of ENSO apparently have decadal variations. The most noted change in recent decades took place in the mid 70s. Before 1976 warm ENSO events occurred less often and had a smaller amplitude than those after 1976 (Graham, 1994; Latif and Barnett, 1994; Zhang et al., 1997; Philander, 1999);

2. The cause of low-frequency variation in ENSO predictability: The performance of many ENSO prediction models vary on decadal time scales. Both 1970s (Balmaseda et al., 1995) and 1990s (Chen et al., 1995; Ji et al., 1996) appear to be less predictable than in 1980s. Flügel and Chang (1998) found that while the 50s and 80s are relatively predictable, the 60s and 70s are less predictable.

This dissertation follows the style and format of *Journal of Climate*.

> Recently, Chen et al. (2004) noted that the predictability of ENSO varies over significant ranges during the past 148 years. Their study suggests that high (low) skill scores during certain periods are associated with the frequent (rare) occurrence of strong warm and cold ENSO events. In that case, low-frequency modulation of ENSO would be closely linked to low-frequency variations in ENSO predictability.

Currently, the underlying mechanisms that are responsible for low-frequency fluctuations in ENSO variation and prediction are not fully understood. Two competing hypotheses that have been put forward to explain low-frequency ENSO modulation are (1) a stochastic mechanism where uncoupled atmospheric "weather noise" with short decorrelation timescales acts as an external forcing that drives drive the coupled system, causing the modulation of ENSO (Penland and Sardeshmukh, 1995; Flügel and Chang, 1999; Neelin et al., 1999; Roulston and Neelin, 2000; Thompson and Battisti, 2001; Yeh et al., 2004), and (2) a deterministic mechanism in which a slowly varying mean state in the tropical Pacific Ocean causes modulation in coupled air-sea feedback and thus ENSO (Wang, 1995; Zhang et al., 1997; Gu and Philander, 1997; Kirtman and Schopf, 1998; Kleeman et al., 1999).

Which of these hypotheses is most likely to be the explanation for the observed low-frequency ENSO modulation is highly controversial and needs further investigation. In particular, there is a need to develop a set of quantitative tests to further validate these hypotheses. Since the stochastic mechanism requires no explicit ocean dynamics, it can be regarded as a null hypothesis against which other mechanisms must be validated. This leads to the objective of the first part of this study, which is to develop a methodology to explicitly test the null hypothesis.

In addition to the issue concerning the decadal modulation of ENSO, there are fundamental issues with regard to identifying the physical mechanism of stochastic forcing. Although internal atmospheric variability has also been proposed to provide a major source of stochastic forcing that drives ENSO (Lau, 1985; Lau and Chan, 1986, 1988; Vallis, 1988; Penland and Sardeshmukh, 1995; Penland, 1996; Flügel and Chang, 1996; Kleeman and Moore, 1997; Blanke et al., 1997; Eckert and Latif, 1997; Moore and Kleeman, 1999a,b; Thompson and Battisti, 2000, 2001; Penland et al., 2000; Philander and Fedorov, 2003; Flügel et al., 2004), there is little coherent understanding of the underlying physical processes that link internal atmospheric variability to ENSO. Therefore, the main objective of the second part of this dissertation is to address this issue. Some of the important questions to be addressed are: through what physical mechanism does stochastic forcing exert its influence on ENSO? In particular, can a stochastically induced trigger mechanism be identified as a precursor to ENSO?

Several other mechanisms have also been speculated as precursors of ENSO. Sporadic westerly wind bursts (WWBs) have long been identified as important triggers of El Niño (Busalacchi and O'Brien, 1981; Philander, 1981; Rasmusson and Carpenter, 1982; Luther et al., 1983; Philander, 1985; Giese and Harrison, 1991; Delcroix et al., 1993; Kerr, 1998; McPhaden and Yu, 1999). A variety of phenomena have been studied as possible causes of WWBs, including the frequently-cited intraseasonal Madden-Julian Oscillation (MJO) (Madden and Julian, 1972, 1994; Kleeman and Moore, 1997; Hendon et al., 1998; Woolnough et al., 2000), the twin or individual tropical cyclones in the west-central Pacific (Keen, 1982, 1988) or in Philippine Sea (Wang et al., 2001), cold surges from extratropics (Lim and Chang, 1981; Lau et al., 1986), or the combination of all the three processes (Yu and Rienecker, 1998), east propagation of South Asia monsoon (Yasunari, 1985, 1990; Gutzler and Harrison, 1986), or stochastic noise forcing composed of the stochastic optimals (Moore

and Kleeman, 1999b). But Yu et al. (2003) showed that WWBs are not effective in triggering ENSO if the atmosphere over the western tropical Pacific is not properly pre-conditioned; other researchers indicate that the ocean heat content over the central Pacific also has to be pre-conditioned such that Kelvin waves initiated by WWBs can effectively alter the surface temperature structure (Perigaud and Cassou, 2000; Fedorov, 2002). Thus far, much of the discussions on the effect of noise on ENSO has been focused on WWBs near the equator around the dateline. There is a need for a more complete study of these random atmospheric disturbances (Philander and Fedorov, 2003).

Tourre and White (1995) discussed the sequencing between the first and second empirical orthogonal function (EOF) of interannual variability in the tropical and north Pacific Ocean, and identified the second EOF as a precursor mode leading the first EOF by 6-9 months. Giese and Carton (1999) also showed the second EOF of SST distinctly leading the first EOF in the interannual timescale (Fig.6 in their paper) using an ocean data assimilation product. But they emphasize that the meridional movement of wind pattern plays an important role in this sequencing (Fig.11 in their paper). A northward displacement of the atmospheric circulation allows westerly wind to develop and thus warm SST and deepen the thermocline in the eastern quatorial Pacific.

Penland and Sardeshmukh (1995) and Penland (1996) proposed an optimal initial condition, a boreal spring basin-scale SST pattern (Fig.6a in their paper) forced by a surface heat flux anomaly associated with anomalous winds north of the ITCZ, that leads to intrinsic ENSO growth over the following 7-9 months. They argue that this pattern of SST can be viewed as a precursor to ENSO, although the underlying physics for the formation of the initial optimal is not explored in detail.

Clarke and Gorder (2001) used a simple statistical model and claimed that the zonal wind stress anomaly in the far western equatorial Pacific (130°E-160°E) is a precursor to ENSO. This anomalous equatorial westerly wind is quasi-biennial (Rasmusson et al., 1990; Clarke and Gorder, 1999; Weiss and Weiss, 1999) and typically begins in about November prior to the El Niño year and then slowly moves eastward to a maximum in the central Pacific in about the following October based on the last 8 El Niños (Clarke and Shu, 2000).

Chang et al. (2004) in a theoretical study suggested that high predictability will be attained in those periods when the noise forcing projects more favorably onto the optimal noise that maximizes the predictability. Flügel et al. (2004) further identified the spatial structure of the optimal noise forcing for ENSO variability that has a maximum variability located in the western Pacific at about 8°N. The noise forcing can maximize the system's predictability up to 1 year in advance.

The previous diverse views may suggest that no single mechanism is solely responsible for onset of ENSO, and invite further investigations.

The most recent work (Czaja et al., 2002; Vimont et al., 2003b; Chiang and Vimont, 2004; Barnett et al., 1999; Pierce et al., 2000), emphasizes a connection between extratropical variability and ENSO. The second part of this dissertation is motivated by these recent studies, especially from (Chiang and Vimont, 2004), where a Pacific "meridional mode" (MM) is identified from the observations. The MM related SST has a strong resemblance to the optimal initial condition of SST shown in (Penland and Sardeshmukh, 1995). Chiang and Vimont (2004) proposed the MM an effective conduit for extratropical atmospheric influence on the tropics, but did not actually establish any link between the Pacific MM and ENSO.

B. Objective

The main objectives of this study are two-fold:

1. To develop a methodology to test the null hypothesis that low-frequency variation of ENSO predictability may be caused by stochastic forcing. Specifically that this null hypothesis will be validated against the deterministic mechanism in which a slowly varying mean state in the tropical Pacific Ocean causes modulation in coupled air-sea feedback and thus ENSO.

2. To identify physical mechanisms that link extratropical variability to ENSO, and to further reveal the extent to which internal atmospheric variability can affect ENSO variation.

C. Main Hypothesis and Approach

The main hypotheses of this study are 1) The stochastically induced ENSO low-frequency variability remains a viable mechanism for explaining decadal modulation of ENSO and its predictability, and 2) The Pacific MM is an effective conduit for extratropical atmospheric internal variability and ENSO and a potential trigger for ENSO development, as well as a key player in determining ENSO seasonal phase-locking.

To test the first hypothesis, we employ an ICM that includes externally specified stochastic forcing and a decadal varying mean background. We then conduct a set of prediction experiments where we systematically vary the strength of the mean background variation while keeping the strength of the stochastic forcing unchanged. From these experiments, we determine the strength of the mean background variation that will give changes in model forecast skills comparable to those induced by

stochastic forcing. By comparing this strength to that estimated from observations, we determine whether the null hypothesis can be rejected.

To test the second hypothesis, we first analyze available observations to reach for evidence that ENSO is related to the Pacific MM. We then develop a new coupled model that combines a state-of-art Atmospheric General Circulation Model (AGCM) and a Cane-Zebiak type of reduced gravity ocean. In this modeling framework, internal atmospheric variability is self-determined by the coupled model and can affect ocean-atmosphere interaction via both surface heat fluxes and wind stresses. A multi-century coupled integration is conducted and used to examine the behavior of model ENSO and of the Pacific MM, as well as the relationship between them. A detailed analysis, combined with other model experiments, is conducted to examine the physics of the MM and its role as a triggering mechanism of ENSO. Finally, a novel noise filter is developed and used to suppress the internal variability in a set of coupled experiments to further validate the findings.

D. Organization of the Chapters

Chapter II is devoted to the first objective. It introduces the issues to be addressed and describes the prediction experiments and analysis techniques to test the null hypothesis. Chapter III begins with a brief review of the current work on the Pacific MM and ENSO connection. It then presents further observational analysis and introduces the new coupled model. The results of the multi-century coupled simulation are presented at the end of the Chapter III. Chapter IV further examines the findings of the experiment described in Chapter III by conducting stand-alone ocean model experiments. Chapter V specifically addresses the role of internal atmospheric variability in ENSO by conducting noise filtered experiments. Finally, Chapter VI

summarizes the major conclusions and discusses future works.

CHAPTER II

TESTING STOCHASTIC ENSO HYPOTHESIS USING AN INTERMEDIATE COUPLED SYSTEM

A. Introduction

It has been noted previously that the overall performance in many ENSO forecast models varies on decadal timescales. The 1980s, for instance, appear to be more predictable than both the 1970s (Balmaseda et al., 1995) and the 1990s (Chen et al., 1995; Ji et al., 1996). Flügel and Chang (1998) also noted that while the 1950s and 1980s are relatively predictable, the 1960s and 1970s are unpredictable. Up to present, the underlying mechanisms which cause these low-frequency fluctuations are not fully understood. Understanding how and why these changes in model forecast skills occur from decade to decade is impeded by lack of a clear understanding about the underlying mechanisms of ENSO irregularity.

As a null hypothesis, Flügel and Chang (1999) proposed, along with other investigators, a stochastic mechanism for low-frequency variability of ENSO predictability. In this mechanism, low-frequency variability of ENSO predictability is hypothesized to be caused by the stochastic processes in the atmosphere. By conducting "perfect model scenario" ENSO prediction experiments, they demonstrated that a similar low-frequency variation to observations occurs for the simulated ENSO. Thus far, this stochastic mechanism has not been tested against other mechanisms which involve a decadal varying mean state. This study represents an attempt to develop a quanti-

---

*Reprinted with permission from "Testing the stochastic mechanism for low-frequency variations in ENSO predictability" by Zhang L., M. Flügel and P. Chang, *Geophys. Res. Lett.*, 30(12), 1630, doi:10.1029/2003GL017505, 2003. Copyright 2003 by the American Geophysical Union.

tative test for the null hypothesis. Following a brief description of the coupled model and prediction experiments in Section B, results of the prediction experiments are presented in Section C. In Section D we discuss the potential of background changes to affect ENSO predictability.

B. Perfect Model Scenario Forecast Experiments With an ICM

To gain understanding of low-frequency variability of ENSO predictability, several investigators (Kirtman and Schopf, 1998; Flügel and Chang, 1999) have suggested to carry out perfect model forecast scenarios in which predictions were made to verify against a long synthetic time series generated by forcing an ENSO model with stochastic wind forcing. The advantages of conducting the "perfect model scenario" ENSO prediction are two-fold: 1) it eliminates initial condition errors in the model so that the limit of the predictability can be attributed to noise in the atmosphere; 2) it allows predictions to be carried out over a long time period so that reliable statistics can be derived.

In (Flügel and Chang, 1999), the synthetic time series was generated by forcing a regional intermediate coupled model with stochastic wind forcing, so that the model does not include any explicit decadal dynamics. The ICM consists of a reduced gravity ocean coupled to an empirical atmospheric feedback model. The oceanic component is a derivative of the Lamont model (Cane et al., 1986; Zebiak and Cane, 1987) and was modified by Chang (1994) to include surface heat flux forcing for predicting changes in the total SST field. The model domain extends over the tropical Pacific Ocean from 30^oS to 30^oN in latitude and from 120^oE to 80^oW in longitude. The spatial patterns of the stochastic forcing were derived in a fashion similar to that of (Blanke et al., 1997); that is, from the leading EOFs of the difference field between the observed

and the empirical wind stress obtained by forcing the statistical atmosphere with observed SST. The time-coefficients were constructed by a Monte Carlo generator with a Gaussian deviate.

Three 1000-year forecast experiments were carried out. The first experiment, which is referred to as the reference case, has a time-invariant mean background. In this experiment, the ICM is first run for more than 1000 years in its coupled mode forced by the wind-stress noise. Then, an ensemble of 12000 predictions were carried out using the same coupled model, but without the noise forcing. A prediction was initialized at every month from model year 50 to 1050 with the output of the 1000-year simulation and had a two-year duration. The characteristics of the stochastically-induced ENSO changes in the reference is studied in details by (Flügel et al., 2004), where they found several transitions from less predictable periods to more predictable periods. The other two experiments carried out had the same experimental set up, except that a decadal-varying background was introduced into the ICM.

By taking advantage of the simple formulation of the ICM, we introduced the varying background into our coupled system by a linear superposition of a slowly varying perturbation to the mean thermocline depth of the reduced gravity ocean. The added perturbation field is derived from the 20^oC isotherm depth (a proxy for the thermocline depth) of an ocean data assimilation product by (Giese et al., 2002). Taking the data from 1968 to 1999 when the data density of the subsurface observation is sufficiently high and the agreement with the assimilation and observation is reasonably good, we low-pass filtered the yearly-averaged thermocline anomalies for the 32 years by summing up the first three Fourier harmonics. The reconstructed perturbation captures some basic aspects of the observed low-frequency thermocline depth variations over the recent three decades.

In order to study the sensitivity of the thermocline perturbation to ENSO pre-

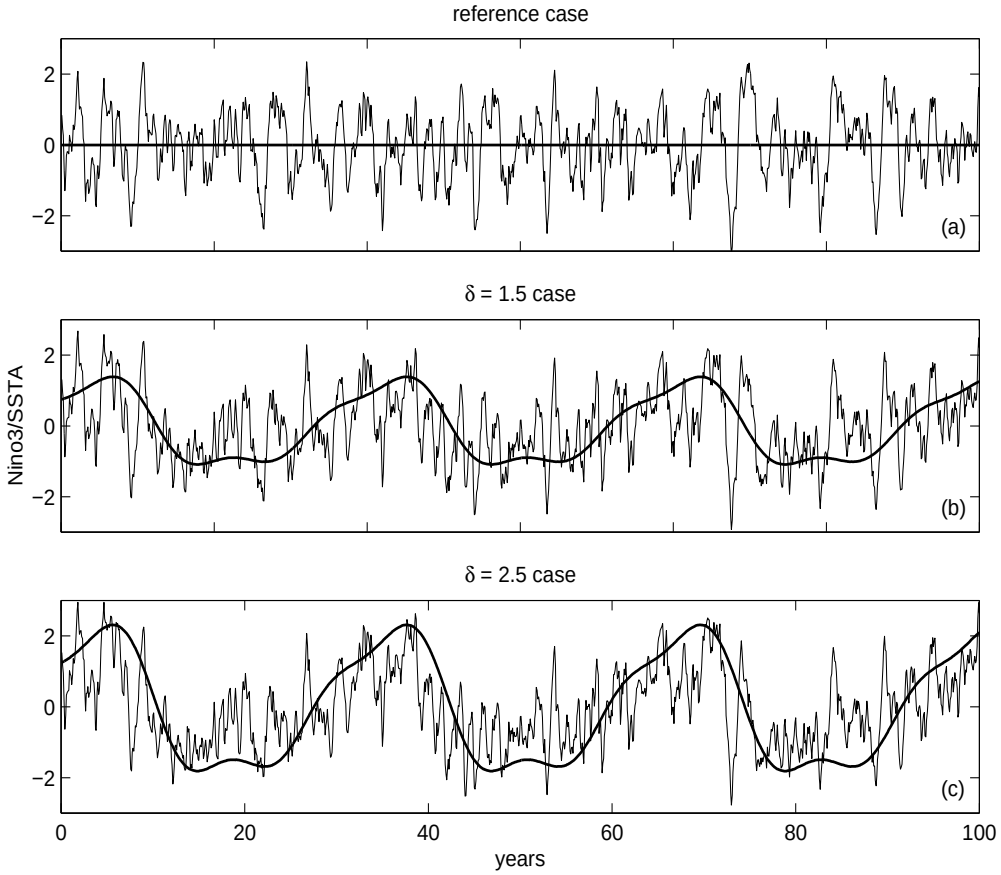

Fig. 1. Time evolutions during first 100 years (out of 1000 years) of simulated NINO3 SSTA for a) δ=0.0, b) δ=1.5, and c) δ=2.5. Thick solid lines indicate time evolution of the imposed decadal-varying background.

dictability, a scaling factor δ was introduced such that δ=1.0 corresponds to the "realistic" value derived from the assimilated run mentioned above. According to the assimilated run the slow variation of the thermocline averaged over the whole tropical Pacific is on the order of $\pm$4m. With such a strength, it turns out that the decadal-varying background has little effect on the simulated ENSO variability. The simulated NINO3 SSTA barely shows any difference from the corresponding time series in the reference case (Fig. 1a). Therefore, we exaggerated the strength of the decadal-varying mean state by using two larger-than-one values of the scaling factor δ=1.5 and δ=2.5, respectively (Fig. 1b and 1c). Obviously, with increasing amplitude, the time evolutions of simulated NINO3/SST anomalies are modulated more and more by the decadal-varying oceanic background (Fig. 1b and 1c thick solid lines). When the thermocline depth is deep (shallow), the prevailing SST anomalies tend to be more positive (negative). As can be seen in Fig. 1c, several such "deep" and "shallow" periods occur. Therefore, two ensembles of 1000-year predictions were carried out with δ=1.5 and δ=2.5. These predictions will be compared to those of the reference case to test the importance of the decadal-varying background in affecting ENSO predictability in the model.

C. Predictability Analysis

As predictability measures, we computed both correlation and RMSE between predicted and "synthetic" NINO3 SSTA. The skill scores for each of the three cases δ= 0.0, 1.5 and 2.5 were computed based on exactly the same periods. In order to compare the range of fluctuation in ENSO predictability among each other, we subdivided the 12000 individual predictions for each case into two groups, each of which has 31 subensembles and each subensemble contains 16 years of monthly SST.

The first group corresponds to the decades when the perturbed thermocline is deep and the second group corresponds to those decades when the thermocline is shallow. In the reference case, even though there is no decadal varying background, we still divided the data in the same fashion as in the other two cases, so that a direct comparison can be made.

Fig. 2 shows the individual score curves for the reference case (a&b), δ=1.5 case (c&d) and δ=2.5 case (e&f). The two groups correspond to the deep and shallow thermocline periods and are indicated by red and green. As the amplitude δ of the decadal-varying background gradually increases, its impact on skill scores becomes more and more evident. At δ=1.5 (Fig. 2c and 2d), the individual skill curves corresponding to deep thermocline periods (red) can be seen to be higher than their counterparts for shallow thermocline periods (green). This separation between the deep and shallow thermocline periods becomes more significant and obvious at δ=2.5 (Fig. 2e and 2f).

Are the changes of ENSO predictability induced by the decadal varying background significant enough to reject the null hypothesis? As an attempt to address this question, we calculated the double standard deviations (2σ) based on the 62 subensembles shown in Fig. 2 for all three cases at each lead time. Assuming the distribution is normal, the double standard deviation gives a statistical measure on how far an individual subensemble of the predictions is expected to deviate from the mean. More specifically, one can say that there is a likelihood of 95% chance that an individual skill curve shown in Fig. 2 lies within $\pm 2\sigma$ from the ensemble mean of all the skill curves. Since the predictability change in the reference case is stochastically induced, the 2σ computed from this case can serve as a yardstick against which the other two experiments can be compared. In order to reject the null hypothesis, the range of ENSO predictability changes induced by a decadal-varying background must

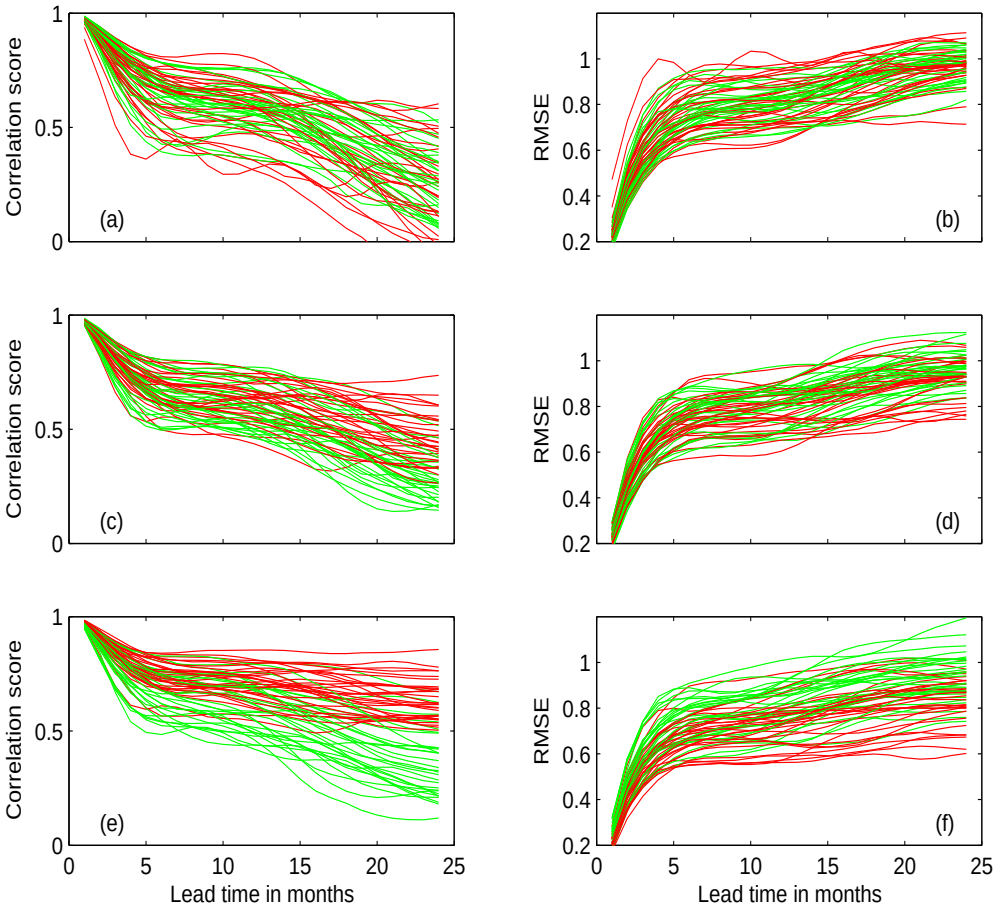

Fig. 2. Individual NINO3 SSTA, a) correlation scores and b) RMSE for the reference case. c) and d): Same, but for δ=1.5 case. e) and f): Same, but for δ=2.5 case. Red (green) curves are based on deep (shallow) thermocline periods.

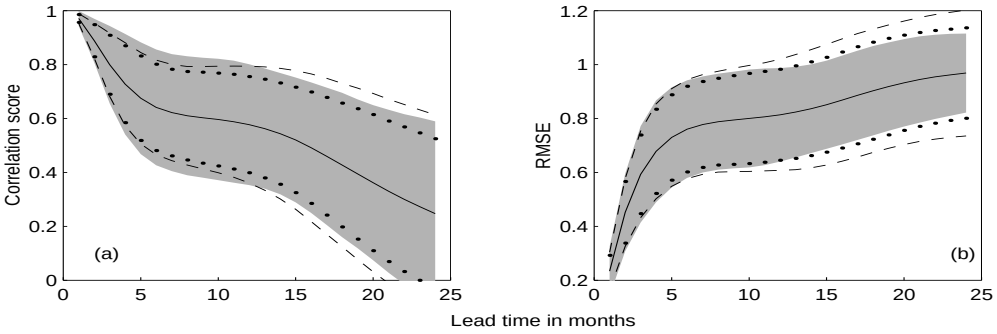

Fig. 3. Comparison of range of fluctuation in a) correlation score and b) RMSE between the reference case (shaded areas), δ=1.5 case (dotted lines) and δ=2.5 case (dashed lines)

lie outside the intervals given by the 2σ of the reference case (indicated by the shaded area in Fig. 3).

For comparison, included into Fig. 3 are the 2σ values in the δ=1.5 and δ=2.5 cases. Since the mean scores (based on all 62 subensembles) for all three cases are similar to one another, we only plotted the mean score of the reference case (solid middle lines in Fig. 3) along with these 2σ values. It is shown that 2σ of the correlation scores for the δ=1.5 case is systematically smaller than the corresponding standard deviation of the reference case. For δ=2.5, the 2σ value exceeds the value of the reference case at lead times beyond one year. Similar behavior is seen for the double standard deviations of the RMSE, except that the lead times at which 2σ value exceeds the reference value appear to be somewhat shorter than those in the correlation scores. Therefore, these results lead to the conclusion that only when the amplitude of the decadal-varying background is sufficiently large ($\delta \geq 2.5$), can one reject the null hypothesis that decadal variation of ENSO predictability may be stochastically induced.

D. Summary and Discussion

In this study, we attempt to test the stochastic mechanism of decadal variation of ENSO predictability in the framework of an intermediate coupled model. By conducting perfect model scenario forecast experiments with and without decadal-varying background, we show that the presence of a decadal-varying background does not substantially modify the characteristics of the low-frequency ENSO variation induced by stochastic processes, unless the amplitude of the background variation is increased to an unrealistically large value. This result suggests that the stochastic forcing may be a leading contributor to the low-frequency modulation of ENSO. More detailed analysis is obviously needed to shed light on how the background change can affect the ENSO predictability. One way to address this issue is to examine the leading ENSO mode in different periods to see how its behavior may be altered by the different mean background. The working hypothesis is that the oscillatory characteristics of the leading ENSO mode is intimately tied to the mean state of the coupled system, so that a change in the mean state may make the ENSO mode to become more damped or less damped, thereby affecting its predictability. To test this idea, we have performed a Principal Oscillation Pattern (POP) analysis (von Storch et al., 1995) on the 1000-year simulation of the δ=2.5 case. The POP analysis is an effective statistical technique for extracting dominant temporal and spatial characteristics of oscillating patterns in a multivariate time series. We applied POP to all 31 deep thermocline periods and to all 31 shallow thermocline periods. The leading POP modes in both periods show a connatural ENSO pattern similar to what is observed in nature (not shown). However, the POP mode in the deep thermocline periods has a higher ratio (r=0.62) between the damping time scale and oscillation period than the POP in the shallow thermocline periods (r=0.51), suggesting that ENSO in the deep thermocline

periods tend to be more oscillatory than in the shallow periods. Interestingly, the ratio for the reference case has a value of 0.57, which is in between the values of the deep and shallow thermocline periods. This result could offer an explanation as to why the ENSO events in the deep thermocline periods tend to be more predictable than those in the shallow periods. It suggests that the mean background change, if it is sufficiently large, can have an important effect on the dynamical properties of ENSO. However, in our coupled system this effect is quite small even when the amplitude of the varying background is exaggerated.

The robustness of this result needs to be further tested since we have so far considered only decadal changes for the thermocline depth in our experiments. This does not take into account slowly varying variations in the stratification of the real ocean. Therefore, further sensitivity studies are planned in which we will introduce into our model decadal changes for both temperature and temperature gradient at the base of the mixed layer.

Finally, it is worth noting that the result presented here may be sensitive to the parameter regime where the model ENSO resides. In our coupled model, ENSO resides in a damped regime. If the model is tuned to a slightly unstable regime as in (Kirtman and Schopf, 1998), then one expects the change in the mean background has a more important impact on ENSO and its predictability. For our system, the simulation in the damped regime gives the most realistic ENSO behavior. However, this does not mean that ENSO in reality resides in a damped regime. Given that it remains highly controversial on the issue where in the parameter regime ENSO resides in reality, our result should be viewed with some caution when applied to reality.

This result should be interpreted within the context of the simple model. A particular concern in this model is the empirical statistical atmosphere, i.e. the absence of atmospheric internal variability. The weather noise here is based on statistical

reconstruction from the observed wind stresses and SST, and introduced into the coupled system as an external forcing.

Another shortcoming of this model is that ICM has oversimplified thermodynamical air-sea coupling. Here the net surface heat flux is assumed to be proportional to the negative of the SST anomaly.

To overcome this shortcoming of the ICM, a preferred approach is to use a more complete atmosphere model, such as an AGCM, where the stochastic processes are internally generated. One major difficulty in using this type of model for the study of stochastic ENSO mechanism is the issue of how to separate the deterministic component of the coupled feedbacks from the stochastic component internal to the atmosphere. We will address these two issues in the next chapter and Chapter V, respectively.

CHAPTER III

INVESTIGATING PHYSICAL MECHANISMS FOR FORCING ENSO VIA INTERNAL ATMOSPHERIC VARIABILITY – A REDUCED-PHYSICS COUPLED GCM STUDY

A. Introduction

The El Niño/Southern Oscillation (ENSO) is one of the most prominent modes of climate variability at seasonal-to-interannual timescales in the earth climate system. Considerable progress has been made to document and gain a fundamental understanding of this important natural climate fluctuation over the last several decades. We now know that ENSO occurs about every two to seven years, it has strong seasonal phase locking and peaks in boreal winter, it is an inherent coupled mode of the tropical ocean-atmosphere system, and it can disrupt weather pattern globally. In terms of our theoretical understanding of this phenomenon, we have learned that the onset of ENSO involves a positive ocean-atmosphere feedback between the wind, Sea Surface Temperature (SST) and thermocline depth known as the Bjerknes feedback (Bjerknes, 1969), and its decay involves negative feedbacks due to subsurface oceanic adjustment known as the ocean memory mechanism (Neelin et al., 1999). The combined affect of the positive ocean-atmosphere feedback and the delayed oceanic negative feedback are key elements of the delayed oscillator theory (Suarez and Schopf, 1988; Battisti and Hirst, 1989) and the related recharge oscillator theory of ENSO (Jin, 1997). These advancements in our understanding of ENSO have laid a theoretical basis for predicting this phenomenon. We now have developed a predictive capability of ENSO, and operational ENSO forecasts are issued routinely by various prediction centers around the world. However, each ENSO event behaves differently

and our ability to forecast them also varies from event to event. It is this diversity and variation in ENSO behavior that is not completely understood and deserves further study. In particular, the onset mechanisms of ENSO remain unclear.

The delayed oscillator and recharged oscillator ENSO theories portray ENSO as a quasi-periodic self-sustained oscillatory phenomenon (Jin et al., 1994; Chang, 1994; Wang et al., 1999; Tziperman et al., 1998) which implies a long predictable time scale of up to one year (Latif et al., 1998) or even two years (Chen et al., 2004) in advance. In practice, however, the useful forecast scales are limited to about 6 months which is considerably shorter than the predicted, theoretical oscillation period of ENSO which is approximately 3-4 years. Although many factors contribute to limit the ENSO forecast timescale, one alternative hypothesis to the self-sustained ENSO oscillator theory, that is more consistent with the ENSO predictive limit, is that ENSO is a combination of damped oscillations excited by and sustained by the internal variability of the atmosphere (Penland and Sardeshmukh, 1995; Flügel and Chang, 1996; Blanke et al., 1997; Kleeman and Moore, 1997; Moore and Kleeman, 1999a,b; Thompson and Battisti, 2000, 2001; Philander and Fedorov, 2003; Flügel et al., 2004). This hypothesis proposes that weather fluctuations at all timescales, independent of ENSO coupled dynamics, provide a major source of stochastic forcing that drives ENSO. This idea offers an appealing natural explanation as to why each El Niño is different (Kessler, 2002) and why it is so difficult to predict (Landsea and Knaff, 2000; Fedorov, 2003), since it incorporates atmospheric "noise" into a theoretical framework of ENSO dynamics. Central questions in this stochastic ENSO theory are: What is the source of stochastic forcing? How can stochastic forcing physically trigger ENSO?

Although answers to the above questions are not entirely clear, several mechanisms that have been speculated as sources of stochastic forcing include the Madden-

Julian Oscillation (MJO) (Kleeman and Moore, 1997; Zhang et al., 2001), and mid-high latitude atmospheric variability (Barnett et al., 1999; Pierce et al., 2000; Vimont et al., 2003a).

The observations that strong intraseasonal oscillations over the western tropical Pacific tend to occur during the onset of El Niño has led to considerable discussion of the relationship between the MJO and ENSO (Kessler et al., 1995; Moore and Kleeman, 1999a; McPhaden, 1999; Kessler and Kleeman, 2000; Kessler, 2002). On the one hand, some studies argue that the westerly wind bursts associated with the MJO can contribute to the genesis and evolution of El Niño through oceanic advection and wave processes (Kessler and Kleeman, 2000; McPhaden, 1999; McPhaden and Yu, 1999). Kessler and Kleeman (2000) show, using an ocean model forced with wind fluctuations similar to those induced by the MJO, that high frequency wind fluctuations can interact constructively with the ENSO cycle through nonlinear ocean dynamics and latent heat fluxes producing rectified SSTs that conceivably can feedback to the atmosphere and influence ENSO evolution. On the other hand, several studies (Slingo et al., 1999; Hendon et al., 1998) point out that there is a lack of overall correlation between the indices of MJO activity and of ENSO. MJO activity occurs over the western Pacific nearly every year, but only some appear to be related to ENSO. Coupled modeling studies (Zebiak, 1989; Roulston and Neelin, 2000) show that the intraseasonal fluctuations within 30-60 day frequency band do not have a major impact on either ENSO statistics or evolution. Kessler and Kleeman (2000) attempts to reconcile these two schools of thought by noting that the most energetic component of the MJO which is characterized by a zonally stationary pattern is indeed uncorrelated to ENSO, but there is a less energetic, eastward propagating component that is connected to ENSO. They further suggest that the latter component is not a cause, but a consequence of warming in the west-central Pacific during

an El Niño event, which is consistent with the study by Fink and Speth (1997). Nevertheless, they argue that this weaker component can interact with ENSO through the rectifying mechanism.

While the detailed role of air-sea feedback in the MJO and the mechanism of active MJO-ENSO interactions remain to be ironed out, there is increasing observational and modeling evidence that climate noise originating outside the tropical Pacific may play an important role in stochastic forcing. In particular, a physical connection between the winter time, intrinsic atmospheric variability in the north Pacific and ENSO has been proposed. In series of studies by (Vimont et al., 2001, 2002, 2003a,b), a so-called Seasonal Footprinting Mechanism (SFM) has been put forward as a way of bringing extratropical influence on ENSO via a phenomenon during the boreal spring. Their studies suggest that northern hemisphere wintertime sea-level pressure variability over the extratropics initiates an SST footprint onto the ocean via changes in the net surface heat flux. These SST anomalies then persist until summer and can subsequently force the overlying atmosphere, resulting in zonal wind stress anomalies that are conducive to initiating and maintaining the Kelvin-wave structure necessary for ENSO variability in the tropical Pacific. This mechanism is diagnosed in their model (Vimont et al., 2001, 2003a) and appears to be in the observed system as well (Vimont et al., 2003b). They further argue that the summer SST footprint in the subtropics bears a resemblance to the optimal SST initial condition (Penland and Sardeshmukh, 1995), thereby lending support to the stochastic ENSO theory. It has been suggested that a similar forcing mechanism operates in Atlantic sector, where the North Atlantic Oscillation (NAO) is a major external influence to tropical Atlantic variability (Czaja et al., 2002).

Motived by the work of (Vimont et al., 2001, 2003b) and similar work by Czaja et al. (2002) in the Atlantic, Chiang and Vimont (2004) focused more closely on

the spring phenomenon and identified a Pacific "meridional mode" (MM), similar to the Atlantic meridional mode, characterized by a north-south gradient of SST anomalies along the Intertropical Convergence Zone (ITCZ) latitude and cross-ITCZ surface circulation with maximum variance in late winter and boreal spring. They further postulate that "the meridional mode is an effective conduit for extratropical atmospheric influence on the tropics". Servain et al. (1999) demonstrated that the Atlantic meridional mode is linked to the Atlantic equatorial mode (often called the Atlantic ENSO mode). Similarly connection in the Pacific has not been established either in observations or in models. The objective of this study is to explore whether this Pacific meridional mode has any relationship with the onset of ENSO, and if so, how it works.

The chapter is structured in the following way. Section B is devoted to an observational analysis aimed at delineating the relationship between the Pacific meridional mode and ENSO and between the Pacific meridional mode and the Northern Pacific Oscillation (NPO). Section C discusses a new coupled model developed to explore the relationship between the meridional mode and ENSO. The numerical experiments and datasets used in this study are also discussed in Section C. Section D compares the coupled model simulation ENSO with observations. Section E explores the relationship between the Pacific MM and ENSO in the long coupled simulation. Section F investigates the physics of the MM. Secion G examines the different onset characteristics of the simulated El Niño events and attempts to classify ENSO events into different categories according to the differences in their onset and relationship to the MM. Section H summarizes and discusses the major results.

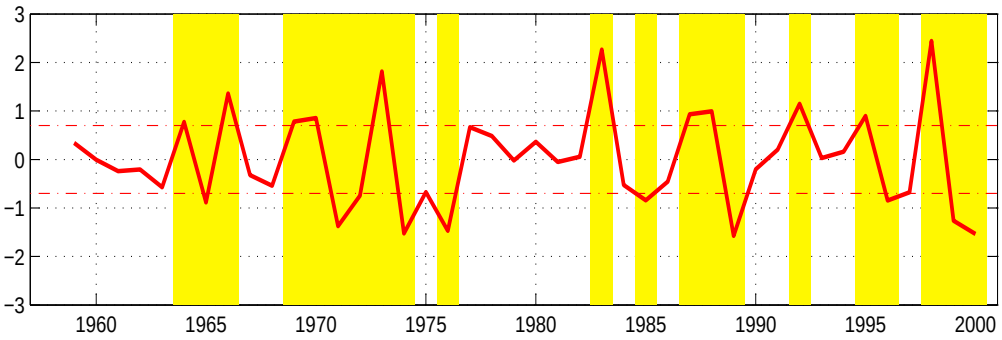

Fig. 4. Time series of normalized NDJ CTI (red solid line). The red dash lines are 70% of the one standard deviation of the CTI. A value greater than it can be considered as an ENSO event, and the corresponding year is an ENSO year. The years removed from the original monthly data are denoted by the yellow shading.

B. Observational Evidence and Hypotheses

Based on observational analysis, Vimont et al. (2003b) propose a SFP mechanism that connects the NPO to ENSO via a phenomenon during the boreal spring. Following this work, Chiang and Vimont (2004) showed that the leading patterns of variability, after removing ENSO-related variabilities using a linear regression, in the tropical Pacific and Atlantic shares same features. Both exhibit the MM structure. They further postulate that the MM is an effective conduit for extra-tropical atmospheric influence on the tropics, but stop short of showing whether there is actually a relationship between the MM and ENSO.

We attempt to follow up on their claim to search for a relationship between the MM and ENSO in observational data. One of difficult issues in this analysis is how to remove the ENSO signal cleanly from such a relatively short observational record. Chiang and Vimont (2004) used a linear regression method. We use a different approach. Since we know that the MM is a spring phenomenon, we first take all

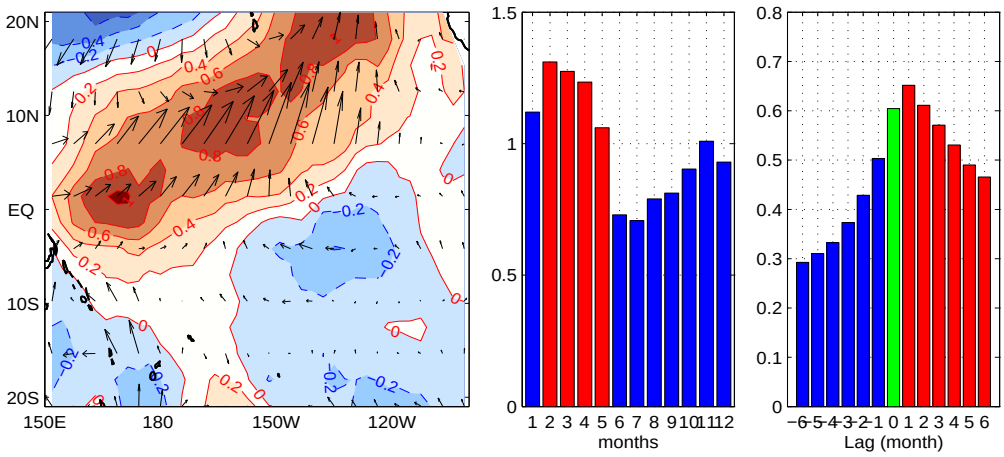

Fig. 5. Spatial (left) and temporal (middle and right) properties of the leading SVD mode between the observed wind stress and observed SST anomaly, using only 21 non-ENSO years. The monthly τ_x and SST anomalies are projected onto the spatial pattern Two monthly time series are obtained and defined as MM τ_x and MM SST index. The seasonal dependence of the MM τ_x index in the middle. Lag-correlation between the MM τ_x index and the MM SST index on the right. Positive lag month signifies that the MM τ_x index leads.

the boreal spring (March-April-May or MAM) surface wind stresses anomalies from ECMWF and SST anomaly from Reynolds (Reynolds and Smith, 1994) from 1958 to 2000. We then remove the anomalies that immediately follow an ENSO event, based on November-December-January (NDJ) cold tongue index (CTI) which is the averaged SST anomaly over the region 180°-90°W and 6°S-6°N. These are the MAM of 1964, 65, 66, 69, 70, 71, 72, 73, 74, 76, 83, 85, 87, 88, 89, 92, 95, 96, 98, 99, 2000, indicated by the shading in Fig. 4. The remaining 21 years out of total 42 years are defined as non-ENSO years. Singular Value Decomposition (SVD) analysis is then performed on the 21-year non-ENSO MAM data and pattern of the first SVD over the domain between 150°E-100°W and 20°S-20°N is shown in Fig. 5. This pattern bears a very close resemblance to the MM pattern identified by Chiang and Vimont (2004). It explains 47% of total co-variance between the residual winds and SSTs and is well separated from the second SVD mode (33%). This pattern is characterized by anomalously warm SST in the northern tropical Pacific region, anomalously cold SSTs in the eastern tropical Pacific, and a southwestly atmospheric flow over the anomalous warm SSTs around the mean ITCZ region. We then project the monthly zonal wind stress τ_x and SST anomalies onto the spatial patterns of the wind and SSTs of the first SVD mode, respectively, and obtain two monthly time series which we define as MM τ_x and MM SST index. The seasonal dependence of the MM τ_x index and lag-correlation between the MM τ_x and the MM SST index are also shown in Fig. 5. The MM τ_x displays maximum variance during the boreal spring (February-March-April-May, or FMAM) and there is a significant correlation between the MM τ_x and the MM SST index from lag of -6 to 6 month with a maximum correlation of 0.65 when the MM τ_x index leads the MM SST index by one month. This lag-correlation relationship is indicative of an air-sea feedback.

To explore the relationship between the MM and ENSO, we derive a boreal spring

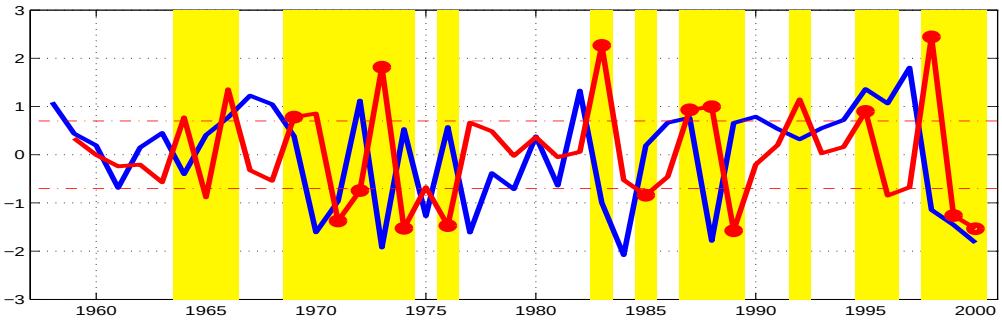

Fig. 6. Time series of normalized observed NDJ CTI (red solid line) and MAM MM τ_x index (blue solid line). The red dash lines are 70% of the one standard deviation of the CTI. The red dots indicate that the ENSO events are preceded by MM events.

MM τ_x index by averaging the monthly MM τ_x index over FMAM, shown as the blue line in Fig. 6. The ENSO variability is gauged by the NDJ CTI indicated by the red ine in Fig. 6. The correlation between the FMAM MM τ_x and the NDJ CTI is 0.65. About 70% of observed El Niño events are preceded by a Pacific MM event. We interpret this result as promising evidence for the MM as a potential triggering mechanism for ENSO.

How robust is our analysis? Is the result sensitive to datasets and analysis technique? We repeated the analysis by using NCEP data and results remain essentially the same. We tested the result by varying the domain size from 175°E to 95°W and from 120°E to 75°W. We also compared our result to that obtained by using linear regression technique (Chiang and Vimont, 2004), and found that the two methods gave very similar results. In fact, the monthly MM τ_x and the MM SST indices are correlated above 0.8. Therefore, the meridional mode is a robust feature, insensitive to the domain, analysis techniques and data sets, in spite of the limited record length (1958-2000).

However, the short observational record does pose a difficulty of further delineating the physics of the MM and its relationship with ENSO. Therefore, there is need of a modeling investigation where the underlying physical processes can be further examined. The model needs to be capable of simulating not only ENSO, but also Pacific MM variability. Therefore, the major objective of this study is to conduct a detailed investigation on the role of the Pacific meridional mode in triggering ENSO using a coupled climate model. The hypotheses that we attempt to test are:

1. Thermodynamic coupling plays an important role in the formation of the MM.
2. The MM can work as a trigger for the onset of ENSO.
3. The relationship between the MM and ENSO is important in determining the seasonal phase-locking of ENSO.

C. A Reduced-Physics Coupled GCM

As stated in the previous section, the objective of this study is to examine, using a coupled climate model, the role of the MM in ENSO dynamics. To achieve this objective, it is necessary that the coupled model is capable of not only simulating ENSO, but also the MM and other related modes of variability internal to the atmosphere, such as NPO. With this objective in mind, we develop a Reduced-Physics Coupled GCM to bridge the gap between fully coupled GCMs and simple intermediate models. The atmospheric component of the model is a state-of-the-art atmospheric global circulation model (AGCM) and oceanic component is a relatively simple reduced gravity ocean model. The advantages of this modeling approach are: (1) The AGCM contains sophisticated physical processes capable of simulating realistic atmospheric response to SST, as well as its internal variability. This overcomes the shortcoming of the ICM

approach in the last chapter, where the atmospheric component has none of its own internal dynamics and is simply a slave to SST, thus internal atmospheric variability must be added as an external forcing. Furthermore, thermodynamical air-sea interaction in the ICM is oversimplified. (2) The ocean model, though simple, contains the essential upper ocean dynamics which are critically important to the air-sea feedback in ENSO. Furthermore, it isolates the upper ocean processes from those below the thermocline, allowing a focused study of the role of the upper ocean in the MM and its relationship to ENSO. (3) It provides a relatively economical modeling tool. Its computational efficiency allows a large number of long numerical simulations to be carried out, from which statistically robust relationships between ENSO and atmospheric internal variability can be sought. In the following, we give a brief discussion of the model and numerical experiments.

1. Atmospheric Model

The atmospheric component is the National Center for Atmospheric Research (NCAR) state-of-the-art Community Climate Model version 3.6.6 (CCM3). It has been widely used in the climate research community and shown to give a realistic simulation of the mean atmospheric circulation and a fairly good simulation of low-frequency atmospheric variability. Global-scale features of the climatology and variability of CCM3 are documented by Hurrell et al. (1998); Saravanan (1998). The version we used has a T42 global spectral horizontal resolution (roughly 2.8° X 2.8° in longitude and latitude) and 18 vertical levels (Kiehl et al., 1998). The integration time step is 20 minutes.

2. Oceanic Model

The ocean component is an extension of Zebiak-Cane type of Reduced Gravity Ocean (RGO) and closely follows to the version of Chang (1994). It is well known that this type of RGO model, which includes the physics of the surface mixed layer, is capable of simulating realistically surface temperature variability. It has successfully been used to forecast ENSO (Zebiak and Cane, 1987). Only a listing of specific modifications is given below, and the additional information about the model can be found in (Chang, 1994; Zhang et al., 2003).

The first modification is made for adaptation to the atmospheric model. Since the atmospheric model is global, the ocean domain is expanded from its original tropical Pacific configuration to a global tropical belt between 30°S to 30°N.

The other major modification is the improved subsurface temperature parameterization. Since the model does not compute the subsurface temperature variation explicitly, it must be parameterized. It is well accepted (Zebiak and Cane, 1987; Battisti and Hirst, 1989; Seager et al., 1988; Chang, 1994) that the temperature anomaly of water entrained into the surface layer can be parameterized in terms of thermocline displacements. That is, the change of entrainment subsurface temperature T' is assumed to be linearly related to the change in the model thermocline depth H', i.e. $T' = \delta H'$, where δ is a matrix of constant coefficients controlling the dependence of subsurface temperature changes on perturbations of thermocline depth. δ is computed as a three-step process: (1) The thermocline fluctuation H' is obtained from the results of the ocean model forced by the ensemble mean wind stresses from the CCM3 Global Ocean Global Atmosphere (GOGA) experiments from January 1980 to December 1994, where the CCM3 is forced with monthly observed SST with slightly different initial conditions for each ensemble member. (2) The subsurface tempera-

ture anomaly T' is derived from an Ocean Data Assimilation (ODA) data product from Geophysical Fluid Dynamics Laboratory (GFDL) (Galanti et al., 2003). Only the portion from January 1980 to December 1994 is used to match the length of the thermocline fluctuation from the RGO simulation. We assume that the T' from GFDL ODA is a good estimate of the observed subsurface temperature variation. (3) The relationship between T' and H' is computed using a multivariable regression. Specifically, δ is computed by linearly regressing the leading five principal components of the subsurface temperature T' onto the five leading principal components of thermocline depth anomaly H'. Once determined, δ is fixed during the entire integration. Therefore, given a H', an estimate of T' is determined statistically from this linear regression relationship.

3. Coupling Strategy

We adopt a coupling strategy where only the anomalous fields of the oceanic and atmospheric component are coupled. This so called anomaly coupled modeling approach has been used in ENSO studies (Yeh et al., 2004). To be more specific, the model mean state is maintained by the observed annual mean surface forcing. To obtain a realistic annual cycle, a flux correction is computed and used. Before the two components are coupled, the ocean model is spun up from a state of rest and integrated for 10 years forced with the observed annual cycle of surface wind stresses and the corrected surface heat flux annual cycle to reach an equilibrium. The annual cycle of SST is defined as the ocean model SST annual cycle. Similarly, we compute the annual cycle of wind stresses and heat fluxes from a 45-year CCM3 GOGA run and define it as the atmospheric model annual cycle. Before exchanging the anomalous fields between the two components, the atmospheric model annual cycle of wind stress and surface heat fluxes are subtracted from the total field to

form anomalous wind stresses and heat fluxes. The observed climatological wind stresses and surface heat fluxes are then added to these anomaly fields to form the complete surface wind and heat flux forcing for the ocean. The ocean model gets this forcing and produces a total SST field in the tropical oceans. Before sending the SST to the atmospheric component, the SST anomaly is computed by removing the ocean model annual cycle of SST, then superimposed onto the observed annual cycle of the global SST. Therefore, outside of the tropics belt of 30°S to 30°N, only the prescribed observed climatological SST is passed to the atmosphere. The oceanic and atmospheric models exchange the anomalous fields once per day.

The inclusion of surface heat fluxes into the coupled model allows us to study the thermodynamic feedback in ENSO physics. As we know, the dynamic feedback in ENSO is relatively well known since it depends primarily on the winds, SST and thermocline variation which are relatively easy to simulate. The thermodynamic feedback, on the other hand, depends on surface heat fluxes which involve a large number of variables (air temperature, SST, relative humidity, cloud cover, and wind speed) and thus contain large uncertainties. Partly for this reason, a flux correction is used in the ocean model SST equation to correct model biases and uncertainties in surface fluxes. We note that this correction term will not have any impact on the anomalous coupling. Here after, we refer this coupled model as CCM3-RGO model.

4. Numerical Simulations and Datasets

We conducted a long control simulation with this CCM3-RGO model (more than 600-years). The analysis presented in this dissertation is based on monthly mean output of the first 400 year simulation. To complement the analysis of the coupled simulation, we also used three other CCM3 simulations. The following is a brief description of each of the model experiments along with their acronyms:

1. CCM3-RGO: A 400-year simulation of CCM3 coupled to the RGO. This serves as baseline data for this study, on which many analysis will be based.

2. CCM3-ML: A 100-year integration of CCM3 coupled to a Mixed Layer (ML) ocean with a specified annual cycle of oceanic heat transport. Please note that here ML is just a slab with spatially varying depth, and the slab ocean does not have ocean dynamics. Therefore, the atmosphere is allowed to interact only thermodynamically with the ML ocean via surface heat fluxes and SST.

3. CCM3-ML-AMIP: An ensemble of six 100-year integrations of CCM3 forced with the SST simulated by the CCM3-ML run. The ensemble members differ slightly from each other in their atmospheric initial conditions. This set of CCM3 runs can be used to identify the atmospheric response to ML ocean SST, and thus to quantify potential feedbacks between the atmosphere and ML ocean.

4. CCM3-SC: A 100-year integration of CCM3 forced with climatological annual cycle of SST. Thereby all the simulated variability is completely generated by atmospheric internal dynamics, and is independent of SST anomalies.

These model simulations are compared to the observations. The observational datasets used in this study consist of:

1. ECMWF: The new reanalysis ERA-40 product provides monthly surface wind stresses, surface heat fluxes and sea level pressure from 1958 to 2000 at the European Centre for Medium-Range Weather Forecasts (http://www.ecmwf.int/research/era).

2. NCEP Reanalysis product: The National Centers for Environmental Prediction

reanalysis data (Reynolds and Smith, 1994; Smith et al., 1996; Kalnay et al., 1996) from January 1950 to December 2000 provide SST anomaly, surface wind stresses and surface heat fluxes.

3. Kaplan SST dataset: The Kaplan dataset contain s monthly data on a 5° latitude x 5° longitude grid over the global oceans dating back to 1856 (Kaplan et al., 1998). Here only the period of January 1901 to December 1949 is used to combine with 50-year NCEP data (1950-2000) for validating the model.

4. GFDL ODA: The subsurface temperature is from the 1980-1999 Ocean Data Assimilation integration carried out at the Geophysical Fluid Dynamics Laboratory (Galanti et al., 2003).

D. Validation of Model ENSO

Before preceding to a detailed study of the relationship between ENSO and meridional mode, it is necessary to demonstrate that the coupled model is capable of realistically simulating ENSO variability and other related modes of variability. Therefore, we devote this section to a comparison of the 400-year CCM3-RGO simulation with observations, using a variety of statistical analysis techniques, such as Empirical Orthogonal Function (EOF) analysis, linear correlation/regression analysis, and composite analysis.

Monthly anomalies are formed by subtracting the long-term monthly means calculated from each calendar month's mean from observations and the 400-year model simulation, respectively. All data are detrended prior to computation of the EOF, regression, correlation and composite maps.

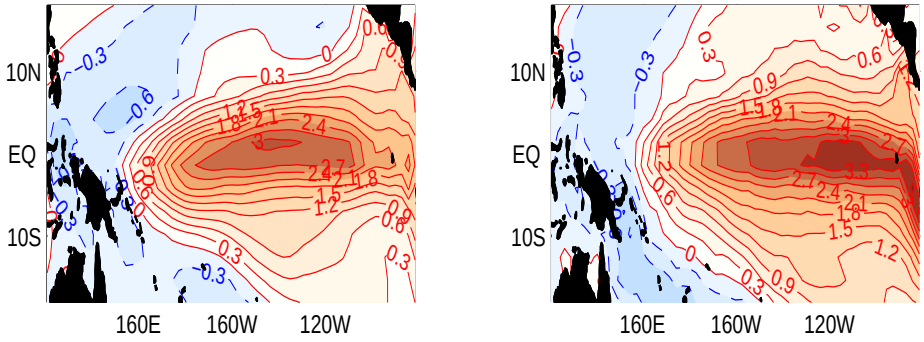

Fig. 7. The first EOF of SST anomaly (left) from the 400-year CCM3-RGO model simulation , and (right) from the observations during 1950-2000.

1. EOFs of SST

The EOF analysis provides an effective way to present the dominant pattern of variability of a dynamic system. The first EOF of SST anomaly over the tropical Pacific region (120°E-80°W, 20°S-20°N) is displayed, respectively, for the model simulation (Fig. 7a) and observations (Fig. 7b). The primary feature of the leading EOF of the modeled SST anomaly in the Pacific shows a close resemblance to that of the observations, with a few exceptions: 1) The simulated SST signature is somewhat more equatorially confined than the observed, especially in the northern tropical Pacific region; 2) The center of the simulated SST maximum variability is slightly shifted westward along the equator, and the large SST variance along the coast of South America in observations is less pronounced in the model; 3) The explained variance of the leading EOF is 45%, compared to 55% in the observations.

The second EOF of the model SST also bears similarity to the second EOF of the observed SST with comparable percent of variance explained (not shown).

These results suggest that the model does capture the basic spatial structure of ENSO related SST variability.

2. Time Series

We now examine the temporal structure of the model ENSO. The NINO3 index, derived by averaging SST anomalies over the region between 5°N - 5°S and 150°-90°W, is often used to characterize temporal variability of ENSO. The time series of the NINO3 index from the CCM3-RGO model simulation is shown in Fig. 8. The corresponding time series from observations for the period of 1901-2000 is shown in Fig. 9. The amplitude of the warm and cold events from the model has a peak-to-peak value of -2.0°C to 2.0°C, which is somewhat weaker than the observed value which ranges from -2.0°C to 3.5°C. The standard deviation of the time series is 0.67 for the model and 0.84 for the observations. The Probability Distribution Function (PDF) of simulated NINO3 SST index (Fig. 10) does not show obvious asymmetry between warm and cold events, whereas the observed PDF is clearly skewed toward positive SST anomalies, that is, there are stronger El Niños than La Niñas in observations. The lack of the skewness in the model SST may be an indication that the model ENSO has less nonlinear dynamics than observations. That said, one can find periods in the 400-year simulation where the SST PDF is more skewed and better agrees with the observations. Overall, we conclude that the model simulates realistic ENSO variability with some periods consisting of more regular warm and cold events (e.g. model year 130-160) than other periods (e.g. model year 245-265).

The low-frequency variability associated with ENSO can be better seen via a wavelet analysis (Torrence and Compo, 1998). To compare directly with observations, a 100-year sample from the CCM3-RGO run is used to demonstrate low frequency variability of the model ENSO cycle. Fig. 11 shows the normalized wavelet power spectrum, for the NINO3 SST anomaly time series for model (upper panel) and observations (lower panel), respectively. For some decades, for instance the decade

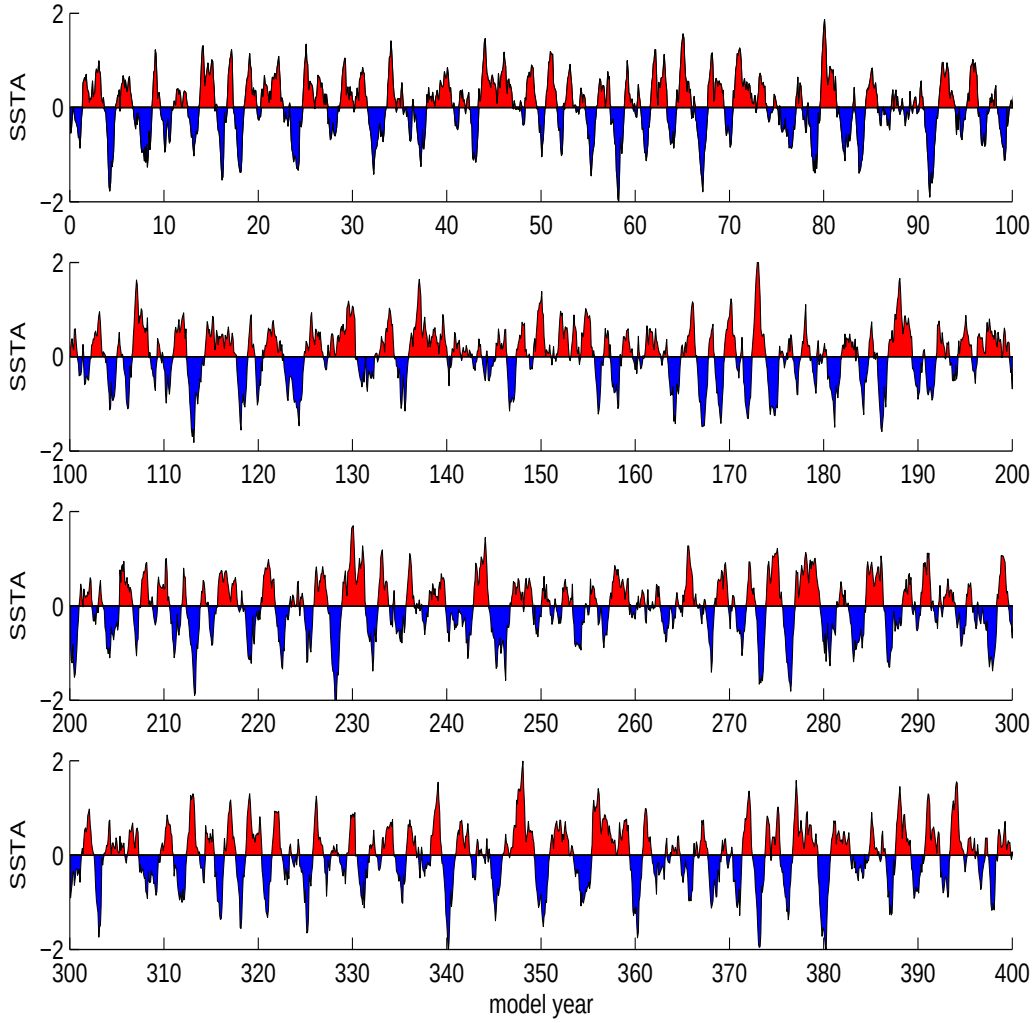

Fig. 8. Time series of the monthly NINO3 SST anomalies (°C) from the 400-year CCM3-RGO model simulation.

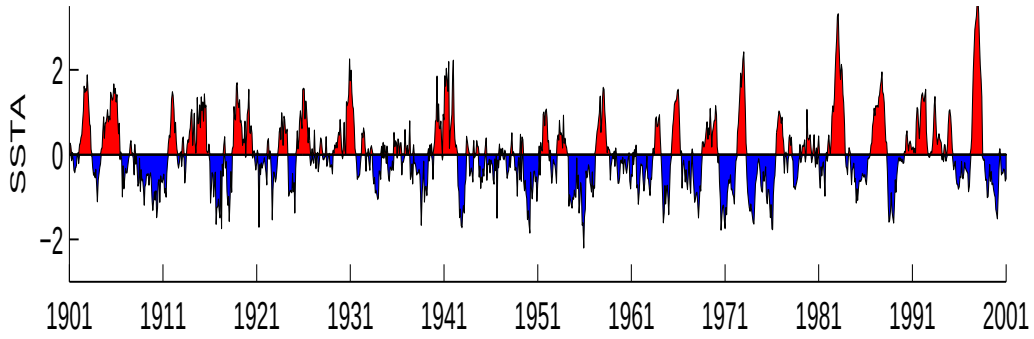

Fig. 9. Time series of the monthly NINO3 SST anomalies (°C) from observations: 1901-1949 from Kaplan data; 1950-2000 from NCEP reanalysis.

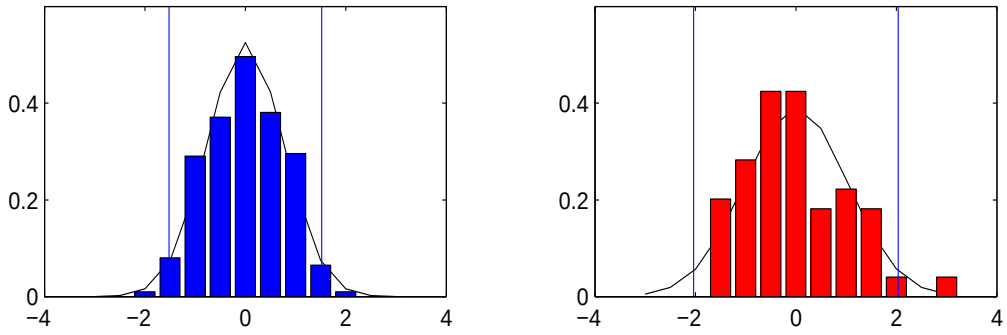

Fig. 10. The PDF of the NINO3 SST index for model simulation (left: blue) and for observations (right: red). The black lines in both panel are the corresponding fitted normal distribution; the two blue lines are the 95% confidence intervals.

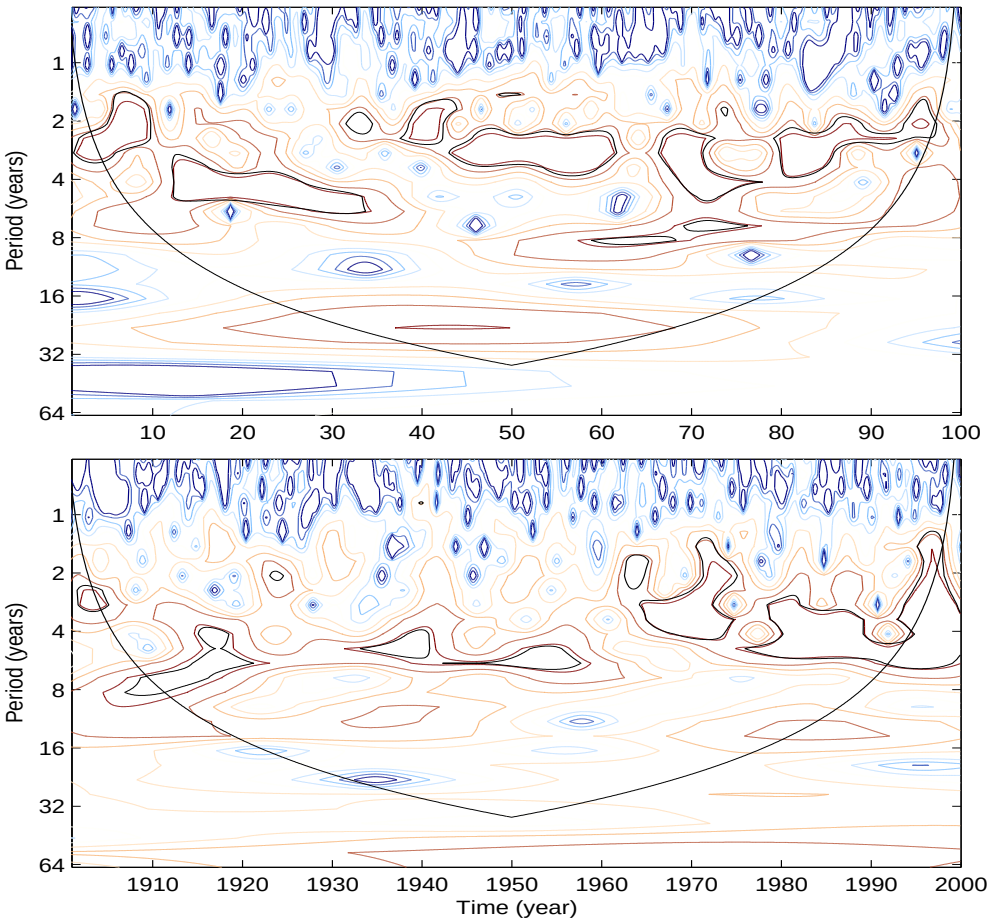

Fig. 11. The wavelet power spectrum of the NINO3 SST anomalies index from 100-year model simulation (upper) and observations (lower). The black contour indicates the 95% confidence level for a red-noise process. Cross-hatched regions indicate the "cone of influence" where edge effects due to finite length of the time series become important.

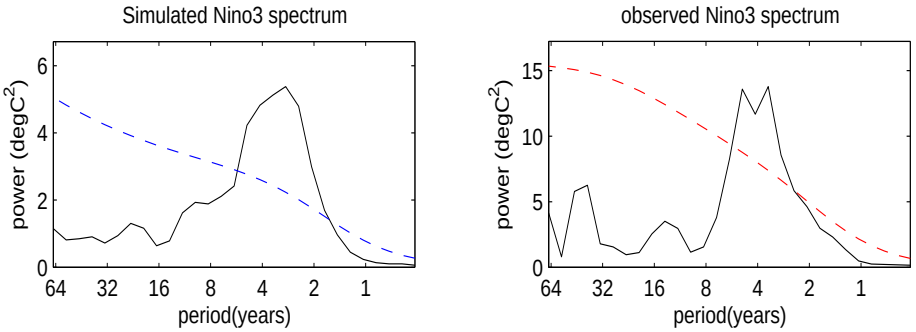

Fig. 12. Power spectra of the simulated (left) and observed (right) NINO3 index. The dashed lines are the 95% confidence level of the NINO3 index for the model (blue) and observations (red).

centered around model year 35 and 65, the simulated ENSO variability is muted. For other decades (model years of 40 to 60), the ENSO variability exhibits a strong three-year oscillation. Most of the power of the model NINO3 is concentrated in the frequency band of 2-8 years as in the observations. However, it is noted that the model ENSO tends to occur at a higher frequency than the observed ENSO. This discrepancy is revealed more clearly in the SST power spectrum (Fig. 12a for the model and Fig. 12b for observations). Here the spectral analysis of the model SST was based on the 400-year time series. As can be seen, the spectrum of the simulated NINO3 SST anomaly reproduces nicely the broad shape of the observed spectral peak with the exception that the spectral peak is at about 3 years in the model and 4 years in the observations.

3. Seasonal Phase-locking

It is well known that the observed ENSO cycle has a tendency to phase-lock to the boreal winter months (Tziperman et al., 1998; Roulston and Neelin, 2000)). This

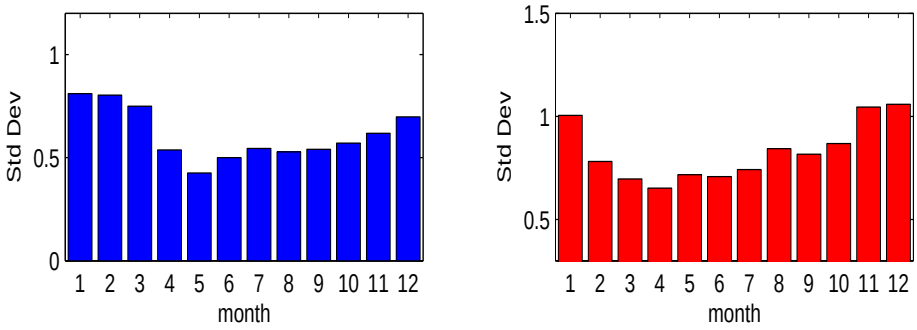

Fig. 13. The seasonal dependence of the standard deviation of the NINO3 index from model simulation (left) and observations (right).

can be inferred by the winter time maximum in the standard deviation of the monthly NINO3 SST anomaly. Fig. 13 shows the standard deviation of the monthly NINO3 index as a function of calendar month for the model (left) and observations (right). Both the simulation and observations share a common feature that the maximum SST anomaly occurs in the boreal winter months (Nov-Dec-Jan) and the minimum occurs in the boreal Spring (Mar-April-May). However, the variance in the observations falls off more rapidly and has its minimum in April, whereas the model's variance falls more gradually and reaches a minimum in May. Additionally, the observations have a slightly larger seasonal change in variance than the model, but the ratio between the maximum and minimum variance remains approximately the same.

4. Lag Correlation Analysis

One of the challenges facing current state-of-the-art coupled general circulation models (CGCMs) is to correctly simulate the atmospheric bridge effect associated with ENSO. To examine the performance of the CCM3-RGO model in this respect within the tropics, we show the lag correlation of ENSO NINO3 index with global

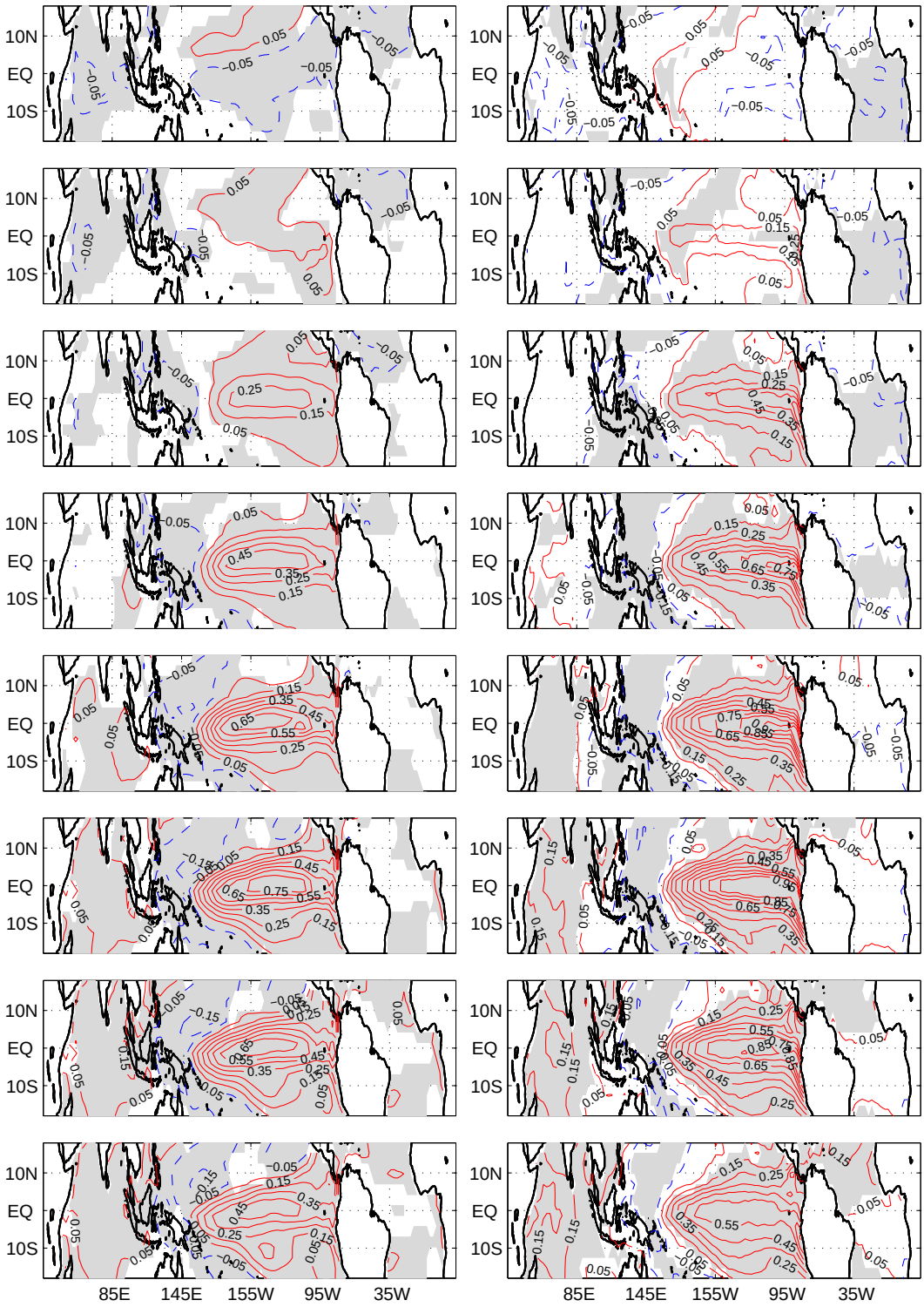

Fig. 14. Lag correlation of the NINO3 index with global tropical SST anomaly between 20°S to 20°N, at different lags -10, -8, -6, -4,-2, 0, 2 and 4 months (from top to bottom), for the model (left-hand column) and for the observations (right-hand column). Negative lags signify that the SST anomaly leads the NINO3 index.

tropical SST anomalies between 20°S to 20°N, at different lags -10, -8, -6, -4, -2, 0, 2 and 4 months, for the model (Fig. 14 left-hand column) and for the observations (Fig. 14 right-hand column), respectively. Negative lags signify that the SST anomaly leads the NINO3 index. The sequence of maps, in a way, reveals the evolution of ENSO, which is a very important aspect of the ENSO cycle. The similarities between the modeled and observed patterns, especially in the Pacific basin are quite striking with the highest regression value in the central and eastern Pacific ocean. Starting at a lag of -10 months, positive SST anomalies can be seen, in both the model and observations, in the northern tropical Pacific just north of the ITCZ; while there is a patch of negative SST anomalies south of the ITCZ. This pattern is reminiscent of the Pacific MM shown in the previous section. At the lag of -8 month, positive SSTs start to appear in the central and eastern equatorial Pacific and along the coast of South America, then subsequently grow in amplitude over the next few months, and finally reach a peak at lag 0. Accompanying the development of warm SST is the simultaneous development of negative SST anomalies in the northwestern and southwestern tropical Pacific. The modeled structure differs from the observations in that it extends less far poleward, especially in the Northern Hemisphere.

The remote influence of ENSO on the other tropical oceans is transmitted through the tropical "atmospheric bridge". This can be detected in the -2 month lag, when the Indian Ocean starts to have warm SST anomalies forming in the entire basin. This warming seems to persist through a lag of 4 months, at which point the observations show a stronger warming in the western Indian ocean while the model shows a more uniform warming. The remote influence of ENSO on the tropical Atlantic Ocean is less well simulated by the model, though the well-known warming in the northern tropical Atlantic after an El Niño is captured by the model.

Overall we conclude that the model reproduces realistic ENSO variability, al-

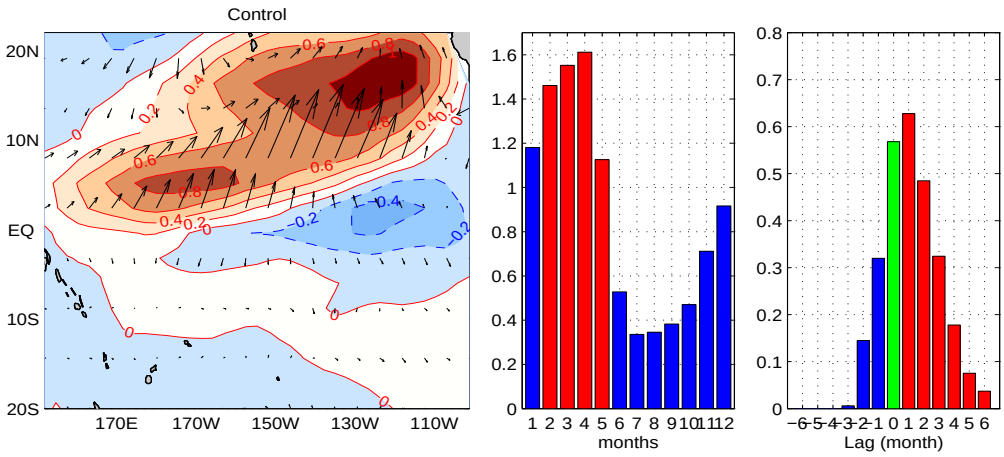

Fig. 15. Spatial (left) and temporal (middle and right) properties of the leading SVD mode between the model simulated wind stress and SST anomaly, using only 198 non-ENSO years (after removing both El Niño and La Niña years). The seasonal dependence of the MM τ_x index in the middle. Lag-correlation between the MM τ_x index and the MM SST index on the right. Positive lag months signify that the MM τ_x index leads.

though it shares some common discrepancies with many other coupled models. These discrepancies include: weak amplitude; westward shift of maximum SST variability, shorter period and seemingly more regular period oscillation than observations.

E. The Simulated MM and Its Relation to ENSO

As shown in Section B, there is a promising observational evidence that the MM may play a role in triggering ENSO. In this section, we examine the MM variability simulated by the model and its relationship to the model ENSO. We further study the relationship between the MM and the NPO.

1. Meridional Mode

Using the same approach as we applied to the observations, we first take the boreal spring (MAM) surface wind stress anomaly and the SST anomaly from the simulated monthly data. We then removed the spring anomalies that immediately follow ENSO events as identified in Section B. A total number of 202 spring anomalies related to El Niño and La Niña events are removed from the 400 spring anomalies of the CCM3-RGO run. An SVD analysis is then applied to the rest of 198 non-ENSO spring anomalies. The resultant pattern (Fig. 15) of the leading SVD shows a close resemblance to the observed pattern. It explains 54% of the total co-variance, which is slightly higher than the observations, suggesting that the MM may be more dominant in the model than in the observations. After this pattern is obtained, the monthly zonal wind stress and SST are projected onto the corresponding patterns respectively, resulting in two monthly time series, i.e., the MM τ_x index and the MM SST index. These indices are used to identify the years when the MM activity is strong. The temporal characteristics of these indices (Fig. 15 middle and right) show striking similarities to the observations: the seasonal variation of the standard deviation of the MM τ_x peaks in the boreal spring (FMAM); the highest lag-correlation between the MM τ_x and the MM SST has a value of 0.65 when the MM τ_x leads the MM SST by one month.

Linear regression is used to test how robust our model result is. This is done by linearly regressing out the variability of the SST and wind stresses that are related to CTI. SVD analysis is then applied to the residual SST and wind stresses in the region between 20°S-20°N and 150°E-95°W. All the fields are detrended, and normalized prior to this analysis. Nearly identical patterns to those of the non-ENSO SVD analysis are produced. The wind expansion coefficient of the first SVD using the

linear regression is correlated with the MM τ_x index at 0.96, and correlation between SST expansion coefficient and the MM SST index is 0.85.

Thus, the Pacific MM is in fact a fairly robust feature in the model, characterized by a positive north-negative south SST gradient and accompanying overlying southwesterly wind regardless of analysis techniques. Furthermore, this Pacific MM is independent of ENSO. A comparison between observations and CCM3-RGO simulation tells us that the model simulation yields very realistic Pacific MM variability during boreal spring. Since the linear regression method and the direct removal of ENSO years method give nearly identical results, we will use these two methods interchangeably in the following discussion.

2. Relation Between Meridional Mode and El Niño

To explore the relationship between the MM and ENSO in the model simulation, we also derive a boreal spring MM index by averaging the monthly MM τ_x index over FMAM, shown as the blue line in Fig. 16. The ENSO variability is represented by the DJF NINO3 index, indicated by the red line in Fig. 16. We choose FMAM for the wind index and DJF for NINO3 SST index as they are the seasons when the behaviors are most pronounced. Please note that here the MM τ_x index is leading SST NINO3 index by 10 months, although we line them together.

The two time series have been normalized by their own standard deviation, so a value greater than one can be considered an El Niño event and an MM event, respectively. About 66% of El Niño events (65 out of 99) in the 400-year model simulation are preceded by the MM (indicated by red dots in Fig. 16). This is especially true for the period of model years 10-70, 300-340, and 370-400.

Using the linear regression method, the residual SST and wind stress anomalies are regressed onto the normalized NINO3 index with different lags. Fig. 17 displays

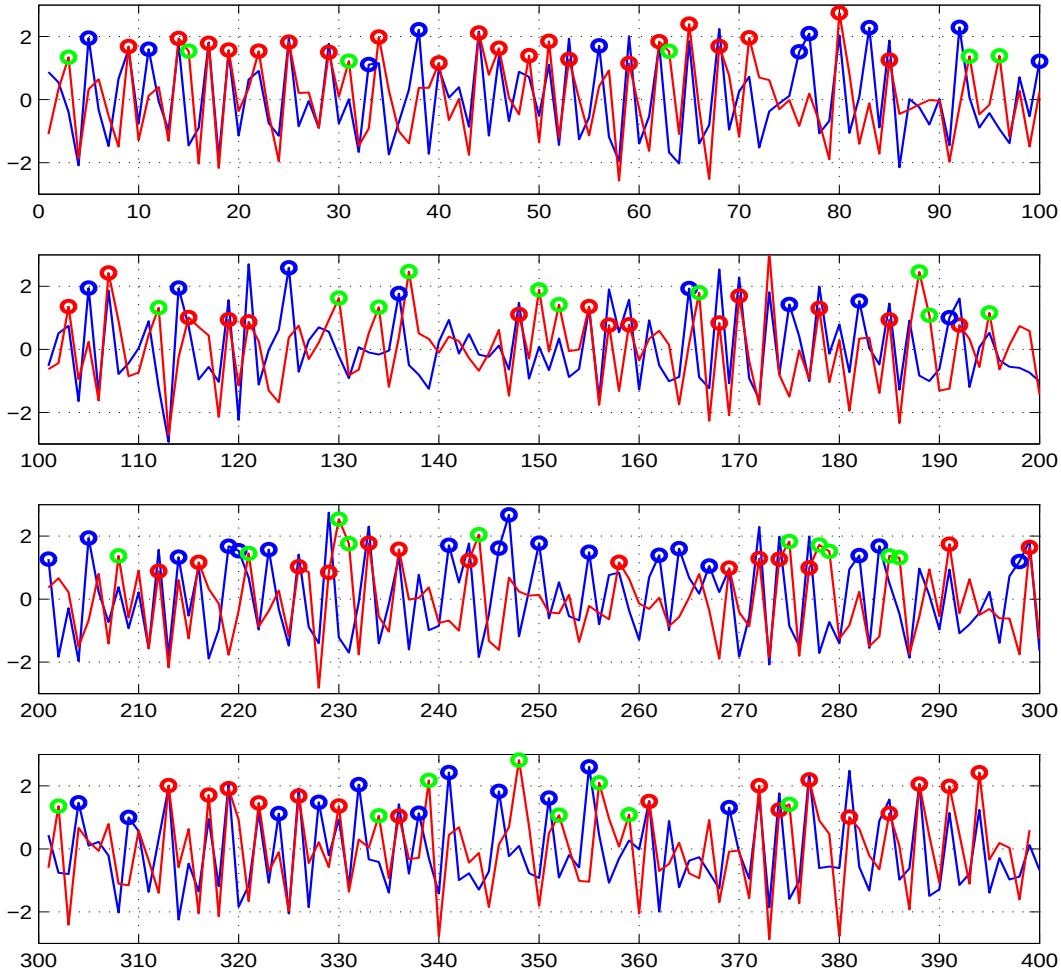

Fig. 16. Normalized MM τ_x averaged over FMAM (blue line) and normalized NINO3 index averaged over DJF (red line) from the 400-year model simulation. Red dots indicate MM-ENSO, green dots indicate ENSO-ONLY, and blue dots indicate MM-ONLY.

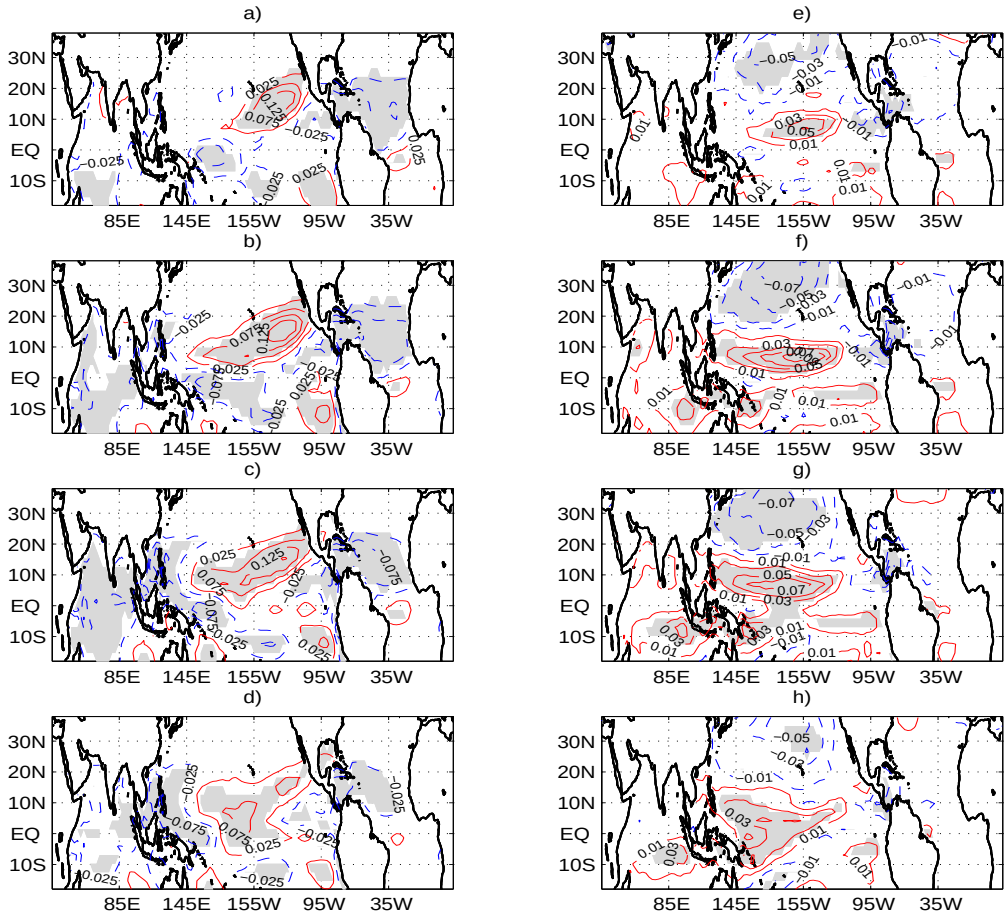

Fig. 17. Lag regression maps of SST (left-hand column) and of τ_x (right-hand column) regressed onto the normalized NINO3 index from the CCM3-RGO simulation at lags of -12 (a, e), -9 (b, f), -6 (c, g) and -3 (d, h) months. Negative lags signify that the NINO3 index lags.

a sequence of lagged regression maps of SST (left-hand column) and of zonal wind stress (τ_x, right-hand column) from the CCM3-RGO simulation at lags of -12, -9, -6 and -3 months. Negative lags signify that NINO3 index lags. This sequence reveals the evolution of the residual wind and SST field. At a lag of -12 month (one year before the peak of ENSO), a tongue of positive SST anomaly appears in the Northern Tropical Pacific (NTP) region. It then moves gradually southwestward and reaches its maximum amplitude at a lag of -9 month (9 months before the peak of ENSO). After that, it weakens somewhat in amplitude but continues to move southwards and eventually reaches to the equator at lag of -3 months (3 months before the ENSO peak). Corresponding to the development of the SST anomalies, the zonal wind stress anomalies show a very similar development. A patch of westerly winds initially appears near the mean ITCZ region around 8°N at a lag of -12 months and intensifies in the subsequent months. It reaches its maximum at a lag of -9 months and then moves to the equatorial region at a lag of -3 months. These regression maps are entirely consistent with the relationship between the MM and ENSO.

3. Relationship Between Meridional Mode and the NPO

How well is the MM variability related to the NPO? How does the relationship between the MM and the NPO in the model compare to the observations? To address these questions, we performed a lag-correlation analysis between the monthly Sea Level Pressure (SLP) anomaly and the monthly MM SST index. The rational of this analysis is to see to what extent the SST variability can be attributed to the NPO related SLP variabilities. The correlation map between SLP and the MM SST index are shown in Fig. 18, with SLP leading the MM SST index by one month, for both the model simulation (left) and the observations (right). The modeled and observed correlation patterns bear remarkable similarity to each other. Both resemble, in many

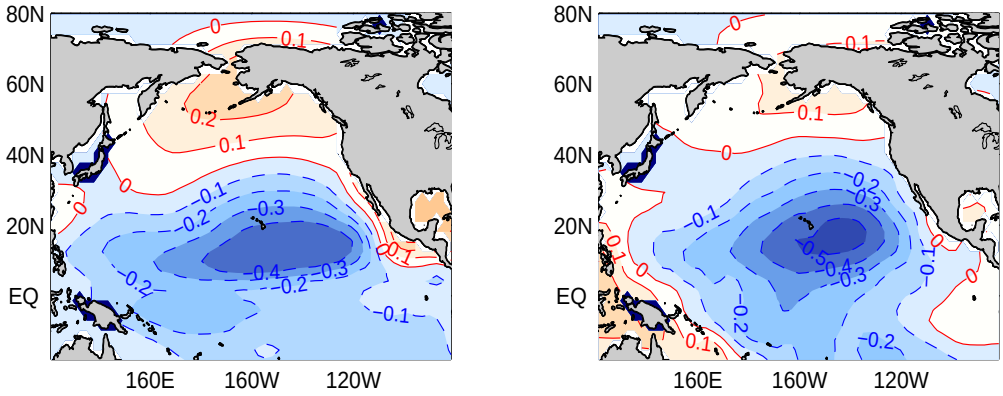

Fig. 18. Lag-correlation between the monthly SLP anomaly and the monthly MM SST index, with SLP leading the MM SST index by one month, for model simulation (left) and for observations (right).

ways, the NPO (Rogers, 1981) pattern, which is considered as an intrinsic mode of the midlatitude atmospheric variability. This suggests that the SST anomalies associated with the Pacific MM in part originate from wintertime atmospheric variability over the north Pacific sector. A detailed look at the correlation map indicates that the north lobe of the SLP fluctuation is not as nearly well correlated with the MM SST index (highest correlation value is 0.2 for the model and 0.1 for the observations) as the southern lobe (highest correlation value is 0.4 for the model simulation and 0.5 for the observations).

To further explore these relationships, two SLP indices are constructed, denoted as NPI and SPI, respectively. The NPI corresponds to the northern lobe of the NPO ,derived by averaging SLP over region 160°E-140°W 50°N-70°N, and SPI corresponds to the southern lobe of the NPO, derived by averaging over region 160°E-140°W and 10°N-30°N. Fig. 19 shows the lag-correlation (upper left panel) between the NPI and the MM SST for the model (dark blue) and for the observations (dark red) and their autocorrelation (upper right panel). The bottom panels show similar analysis

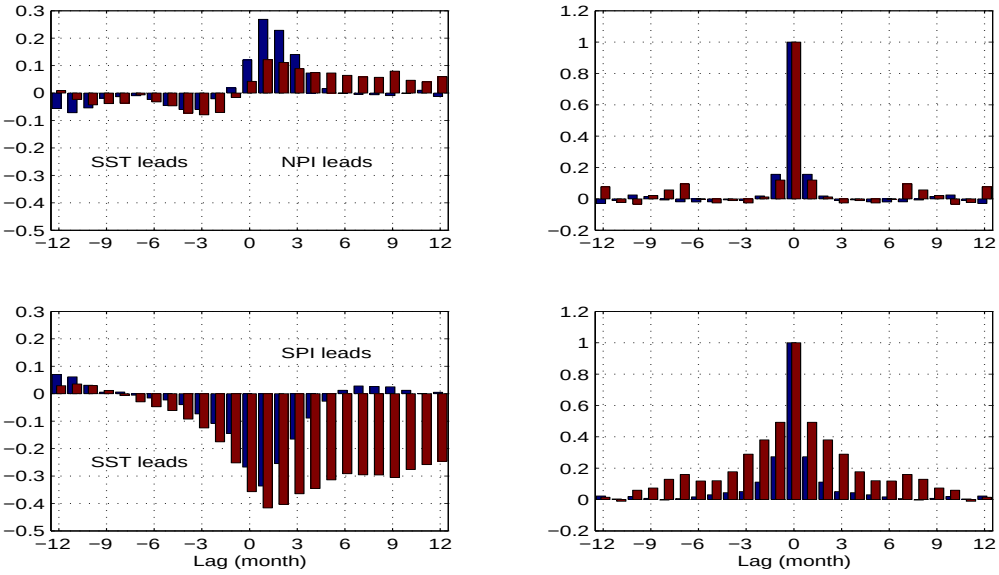

Fig. 19. (Upper panel) lag-correlation (left) between the NPI and the MM SST index, and autocorrelation of NPI (right) for the model (dark blue) and for the observations (dark red). (Bottom panel) lag-correlation (left) between the SPI and the MM SST index, and autocorrelation of SPI (right) for the model (dark blue) and for the observations (dark red).

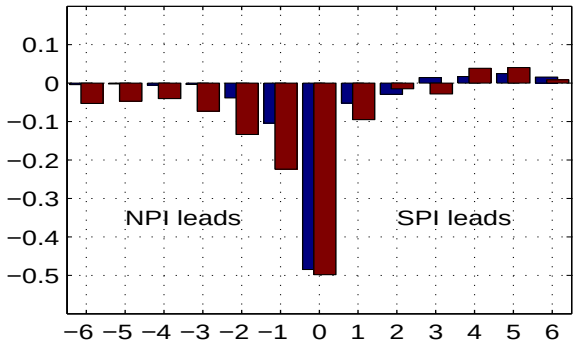

Fig. 20. Lag correlation between the SPI and NPI for the model (dark blue) and for the observations (dark red).

between the SPI and the MM SST. In both cases, the maximum correlation occurs when SLP indices lead the MM SST index by one month, consistent with the idea that the NPO forces the Pacific meridional mode. However, there is a considerable asymmetry in the lag-correlation structure in the southern lobe and its de-correlation time scale is considerably longer the northern counterpart both in the observations (dark red) and in the model (dark blue), suggesting that some ocean-atmosphere coupling may exist between the southern lobe of the NPO and the meridional mode. In other words, the southern component of the NPO is more involved in the formation and the development of the meridional mode than the northern component.

This raises the question of whether the MM is connected to the NPO as a whole or just to its southern component. Fig. 20 shows the lag-correlation between the NPI and the SPI. The highest correlation occurs at zero lag with a value of 0.5, suggesting that these two components are highly coupled to each other both in the observations (dark red) and the model simulation (dark blue). The asymmetry around zero lag may indicate that the NPI has some impact on exciting the SPI. Therefore, a possible scenario for the NPO-MM connection is that the NPO, a seesaw of atmospheric

pressure between Alaska and Hawaii, provides a source of forcing during boreal winter to the MM related SST. Once formed, the MM interacts with the southern component of the NPO, accounting for the long persistence.

F. Thermodynamic Coupling in Meridional Mode

The analysis in the two previous sections suggests that ocean-atmosphere coupling plays a role in the development of the MM. But, what is the nature of this ocean-atmosphere coupling? Does subsurface ocean dynamics play a major role in this ocean-atmosphere interaction? To address these questions, we analyze other sets of CCM3 experiments, each of which differs in the complexity of their ocean physics, and compare them with the 400-year control simulation of the coupled CCM3-RGO model and the observations. These experiments are: 1) 100-year CCM3-ML coupled simulation, 2) 100-year CCM3-SC simulation, and 3) an ensemble of six 100-year CCM3-ML-AMIP runs. Recall that the CCM3-SC run is forced only by the prescribed annual cycle of SST, thereby, the variability in the winds and heat fluxes are generated entirely by atmospheric internal dynamics.

To facilitate comparison, we adopt the following approach to analyze these experiments. First, the EOFs of the boreal spring meridional wind stress are computed. Note that to remove ENSO from the CCM3-RGO simulation and observations, only non-ENSO spring years are used for these cases. For other experiments, since ENSO is not present by design, we use all the spring data. The explained variance is 30%, 26%, 23%, 16%, and 24% for the observations, CCM3-RGO simulation, CCM3-ML, CCM3-SC and CCM3-ML-AMIP, respectively. We then project the SST anomaly (except for CCM3-SC), wind stress and net surface heat flux anomalies from each dataset onto the time series associated with the first EOF of the corresponding meridional wind

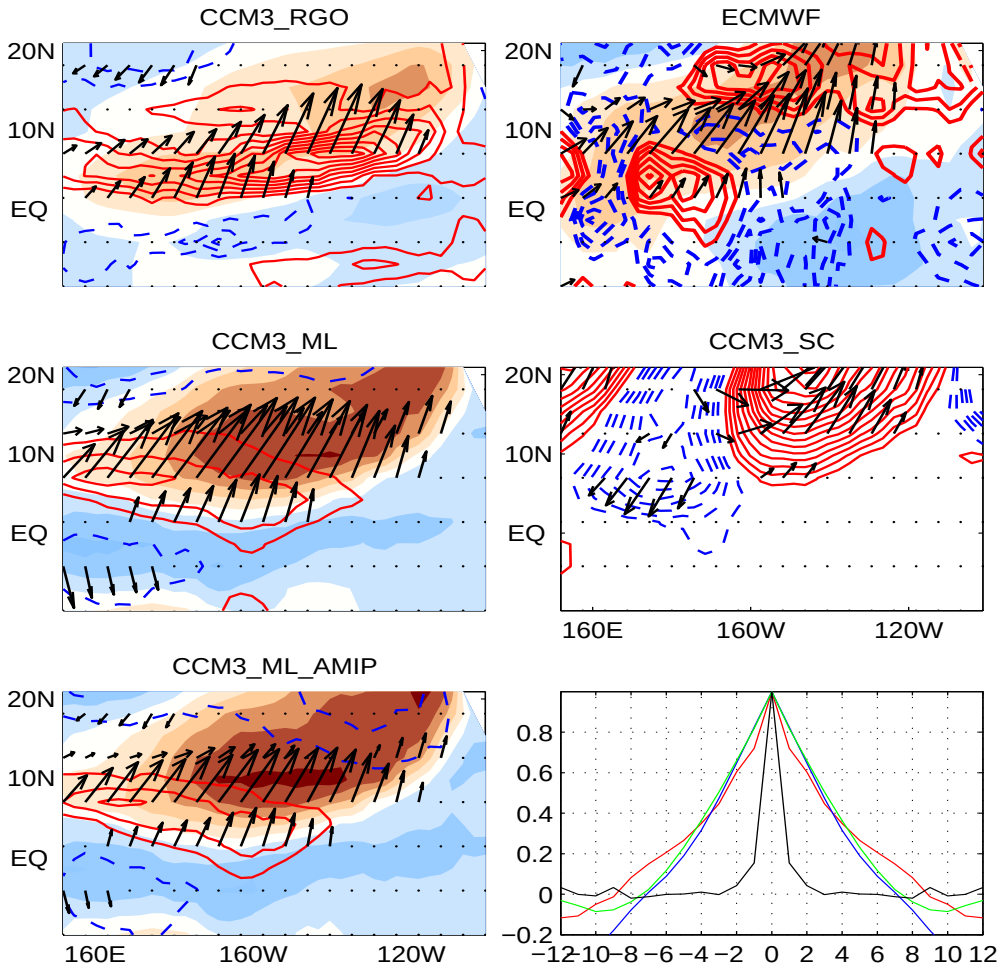

Fig. 21. Resultant projection patterns of SST anomalies (except for CCM3-SC), wind stress and net surface heat flux anomalies onto the time series of the first EOF of the corresponding meridional wind stress for CCM3-RGO, ECMWF, CCM3-ML, CCM3-SC and CCM3-ML-AMIP. Note the CCM3-RGO simulation and observations only use non-ENSO years. The bottom right panel shows the autocorrelations of the time series of the first EOF of τ_y for observations (red), control run (blue), CCM3-ML (green) and CCM3-SC (black), respectively.

stress τ_y, respectively. The resultant projection patterns are shown in Fig. 21 where the SST anomaly is shown shaded, wind stresses in vector and heat flux in contour for CCM3-RGO (a), observations (b), CCM3-ML (c), CCM3-SC (d) and CCM3-ML-AMIP (e). All the patterns, particularly the wind and SST, share great similarity to the structure of the MM, with the only exception being the CCM3-SC. For this later case, the maximum variability in winds and heat flux is in the northern most portion of the domain, suggesting the variability originates from the extratropical region. The presence of the meridional mode in CCM3-ML simulation confirms the earlier finding that its existence does not depend on ENSO. It further suggests that ocean dynamics play a secondary role and the thermodynamic feedback between heat flux and SST in the vicinity of the ITCZ plays a fundamental role in this mode.

These findings are based on the following set of facts: First, we know by its construction that the CCM3-ML simulation allows only thermodynamic ocean-atmosphere feedback, since the ML ocean has no ocean dynamics and thus can not support ENSO. Consequently, this simulation completely eliminates any ENSO-related SST effect, and only those atmospheric responses to non-ENSO SST forcing is permitted. Second, the fact that the CCM3-SC run shows a different pattern of response from the other cases and the fact that the leading EOF in this case explains much less variance than in the other cases tells us that the thermodynamic feedback is fundamentally important for the meridional mode. The absence of the MM in CCM3-SC run reflects the lack of the SST anomaly in the tropics that is critically important in maintaining the right wind stress pattern and thus the MM.

Further support to these finding comes from the differences in persistence of the τ_y anomaly between the CCM3-SC run and other runs. Fig. 21(bottom right) shows the autocorrelation of the time series associated with the leading τ_y EOF for observations (red), control run (blue), CCM3-ML (green) and CCM3-run (black),

respectively. Evidently, the τ_y in the CCM3-SC has a much shorter de-correlation time scale than in the other cases which exhibit similar persistence. This again suggests that the feedback between the ML ocean and atmosphere plays an important role in maintaining the MM.

An examination of the heat flux anomaly provides some direct evidence of this positive thermodynamic feedback. In the northwestern tropical Pacific, we note that the positive heat flux anomaly tends to coincide with the positive SST anomaly in all the experiments, except CCM3-SC, as well as in observations, suggesting a positive feedback between heat flux and SST in this region. Particularly convincing evidence comes from the ensemble of six CCM3-ML-AMIP runs where the positive heat flux anomaly also coincides with a positive SST anomaly in the western tropical Pacific just north of the equator. Since this heat flux anomaly is derived from the ensemble average of the six runs, it should give a good estimate of the response of the atmosphere to the SST anomaly simulated by the CCM3-ML. Therefore, a positive correspondence between the SST and heat flux anomalies in this set of runs is strongly indicative of a positive thermodynamic feedback. This means that at least partially the Pacific MM is a product of thermodynamic coupling between the atmosphere and the ocean. This mode of variability is distinctive from ENSO because it does not involve subsurface ocean dynamics.

In summary, we believe the MM is generated by the following physical process: First the NPO-type internal atmospheric variability during the boreal winter generate a heat flux anomaly in the northern tropics that forces the ML ocean, giving rise to an SST anomaly. Then the atmosphere responds to the SST anomaly by modulating the strength of the northeasterly trade winds in such a way that it produces a heat flux anomaly that reinforces the initial SST, causing the anomaly to persist.

This interpretation is further supported by a lag regression analysis of zonal

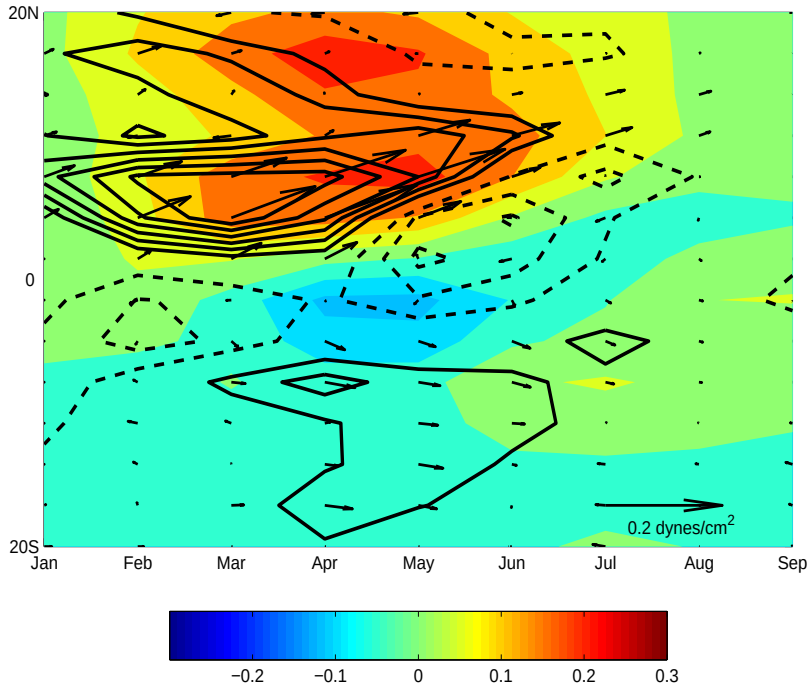

Fig. 22. Lead-lag regression of monthly mean, zonally averaged anomalies onto the normalized FMAM wind expansion coefficient of the leading SVD mode, from Jan to Sep. Colors indicate SST anomalies, vectors are surface wind stress, and contours denote net surface heat flux (contour interval is 3 W m^{-2}).

mean SST, wind and heat flux anomalies, similar to that performed by Czaja et al. (2002) for the Atlantic MM study and also by Chiang and Vimont (2004) for both the Pacific and the Atlantic MM study. Following Czaja et al. (2002) and Chiang and Vimont (2004), we took the normalized FMAM wind expansion coefficient of the first SVD mode from CCM3-RGO and lag-regressed it onto the zonally averaged anomalies of SST, winds, and surface net heat flux across the domain (150°E-90°W, 20°S-20°N). Fig. 22 shows the regression of winds (vector), heat flux (contour) and SST (shaded) as a function of latitude from 20°S to 20°N and a time lag from January through September. The regression of winds shows a maximum southwesterly wind anomaly centered along 8°N in FMAM. This is expected because FMAM are the months where the wind expansion coefficient is derived. The maximum center of the winds coincides with the center of the SST anomaly (shaded), suggesting the winds are forced with the SST. The maximum center of heat flux (contour) is about 2 months ahead of that of the warm SST anomaly during boreal winter/spring, suggesting that the warm SST is initially forced with the heat flux. However, in the later spring and early summer, the positive heat flux tends to follow the positive SSTs, suggesting a positive feedback. This positive feedback causes the wind anomaly to persist from February to June, which is very important for excitation of ENSO warm events, as will be further discussed in the later sections.

G. Classification of ENSO Events

Having established the creditability of our CCM3-RGO model, we next take a close examination of the onset processes of all the El Niño events simulated by the model. Given that the relationship between the MM wind index and NINO3 index is highly significant at the 99% level (higher than 0.50 for the entire 400 years record).

We expect a significant amount of modeled El Niño events that develop following MM events. However, the statistics also tell us that not every MM event is followed by an ENSO event. Thus, we expect to see some El Niño events not preceded by a MM event.

To quantify the relationship between MM and ENSO, we separate all the El Niño and MM events into three groups using the MM index and NINO3 index: (1) El Niño events that are preceeded by a MM event (hereafter MM-ENSO): These are the events that the MM index and NINO3 index are both above their standard deviation and coincide, as indicated by the red dots in Fig. 16. The majority of El Niños fall into this group (66 out of 99 events). (2) El Niño events that are not preceded by a MM event (hereafter ENSO-ONLY): These are the events that the NINO3 index exceeds the standard deviation, but not the MM index as indicated by green dots in Fig. 16. 33% of the simulated El Niños fall into this group (33 out of 99). (3) MM events that are not followed by an El Niño event (hereafter MM-ONLY): These are the events that the MM index exceeds the standard deviation, but not the NINO3 index as indicated by the blue dots in Fig. 16. 41% of the MM events fall into this group (45 out of 111).

To see how the canonical evolution of the events in each group differs, we made a composite analysis of SST anomalies. An El Niño event is identified as follows: the SST anomaly averaged over the NINO3 region exceeds one standard deviation for at least three consecutive months. We only show the composite for El Niño events in these figures because onset mechanisms for El Niño and La Niña are not necessarily symmetric (Delcroix et al., 2000), therefore it may be inappropriate to combine the warm and cold events in a simple manner. Fig. 23 shows the composite of seasonally averaged SST for MM-ENSO (left panel), ENSO-ONLY (middle panel) and MM-ONLY (right panel) from DJF^0 (the first row), MAM^0 (the second row), JJA^0 (the

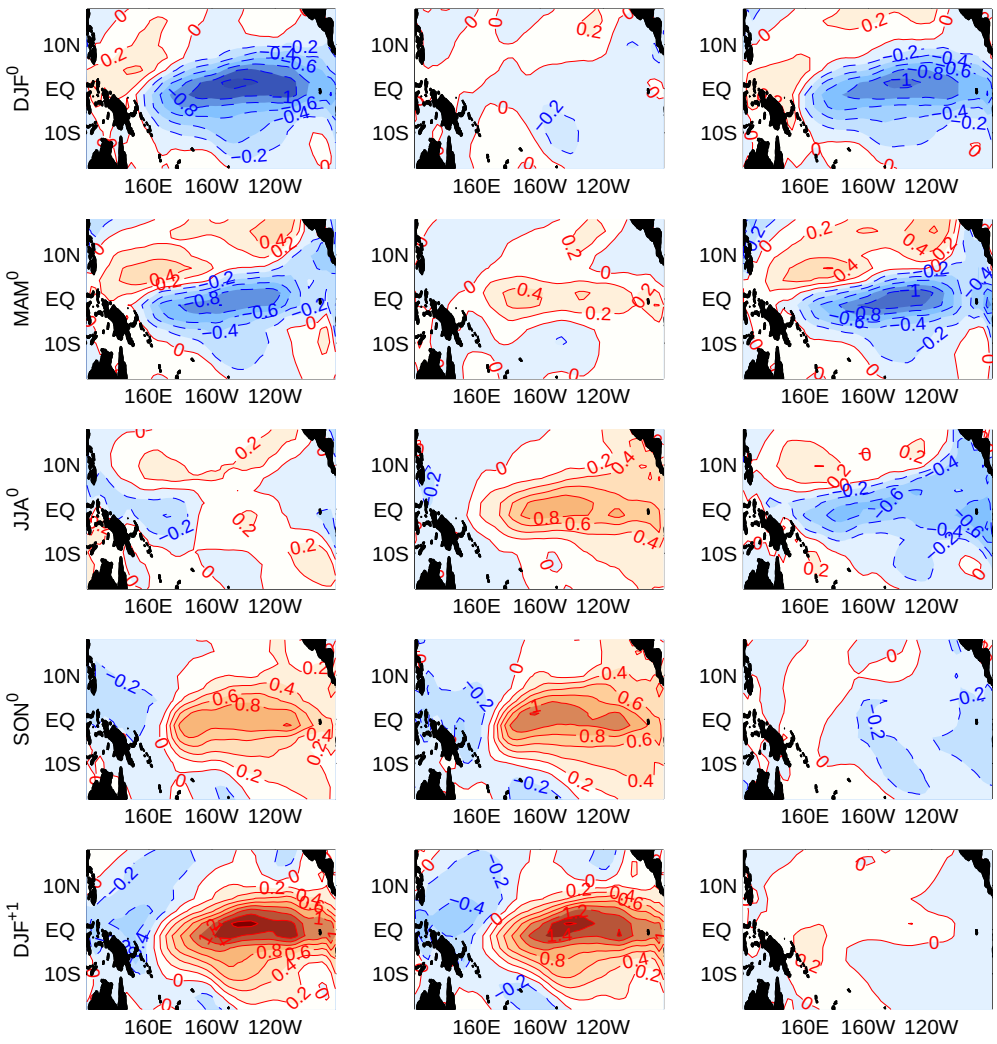

Fig. 23. Composites of seasonally averaged SST for MM-ENSO (left panel), ENSO-ONLY (middle panel) and MM-ONLY (right panel) from DJF^0 (the first row), MAM^0 (the second row), JJA^0 (the third row), SON^0 (the fourth row) and DJF^{+1} (the last row), respectively.

third row), SON^0 (the fourth row) and DJF^{+1} (the last row).

The difference in the onset of the events is quite obvious between MM-ENSO and ENSO-ONLY, as can be seen for DJF^0, MAM^0 and JJA^0 composites. For ENSO-ONLY, warm SST anomaly starts to appear in DJF^0 and by MAM^0 the whole equatorial zone is already quite warm with maximum warming in the west-central equatorial Pacific. In contrast, the SSTs in other two groups are still quite cold during these seasons. For MM-ENSO, the warming in the deep tropics does not start until JJA^0. In spite of this late start, the warm SST anomaly in MM-ENSO develops very rapidly into a mature El Niño in DJF^{+1}, so that the El Niños in MM-ENSO and ENSO-ONLY peak in the same season. Another interesting distinction is that the warm SST anomalies in MM-ENSO tend to develop along the South American coast, whereas in ENSO-ONLY they start to develop in the west-central Pacific. Similar differences are reported in the observed ENSO. For example, the El Niño events between 1976 and 1996 seemed to start in the equatorial western and central Pacific (Wang, 1995; Wang and An, 2002), while the warm SST anomalies associated with El Niño events between 1950 and 1976 first began along the South American coast and propagated westward (Rasmusson and Carpenter, 1982).

The difference between MM-ENSO and MM-ONLY lies mainly during and after the boreal summer, JJA^0. SST anomalies in both groups are almost identical during the boreal winter and boreal spring, but starting from boreal summer, the SST anomaly involves into El Niño in MM-ENSO, but not in MM-ONLY. This suggests that although the MM events lead to a similar condition in boreal winter and spring, the condition alone does not guarantee the development of an El Niño. It implies that either there is a difference in the subsurface ocean preconditioning between the two groups or the conditions in the boreal summer also matter.

Therefore, the issues at hand boil down to the following sets of questions:

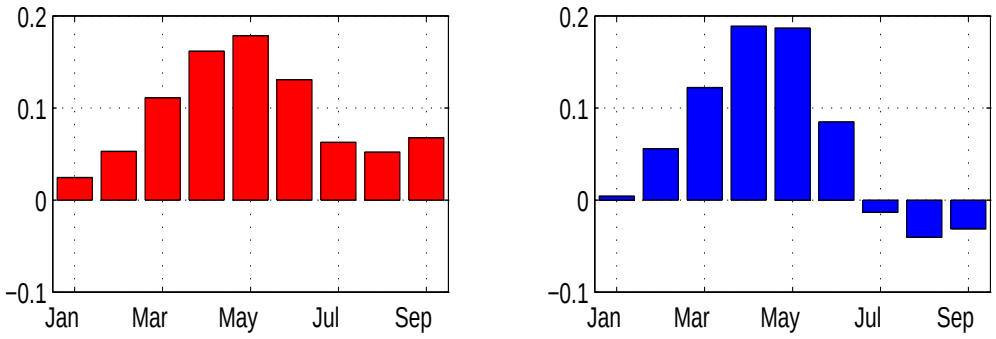

Fig. 24. Composites of the MM τ_x index for MM-ENSO (red) and MM-ONLY (blue).

1. Why can some Pacific MM events excite ENSO while some can not? Is this difference caused by the differences in subsurface ocean preconditioning or in summer conditions or both?

2. Why do some El Niños need the MM to kick off while the other do not? Is it because some El Niño behave more like a self-sustained oscillator than the others?

To address the first set of questions, a composite of the MM τ_x index is shown in Fig. 24 for MM-ENSO and MM-ONLY. This is done by averaging all the MM events as a function of calendar month within the years that these events occur in, MM-ENSO (left) and MM-ONLY (right), respectively. The major differences between the two groups are the persistence of the wind anomaly. In MM-ENSO, the winds appear to persist much longer, from late winter to summer without reversing sign, while the winds in MM-ONLY appear to be short lived, loses in strength dramatically and even reverses sign starting from July.

This can be further verified by the composites of SST (color), winds (vector), and surface net heat flux (contour) anomalies for MM-ENSO and MM-ONLY, respec-

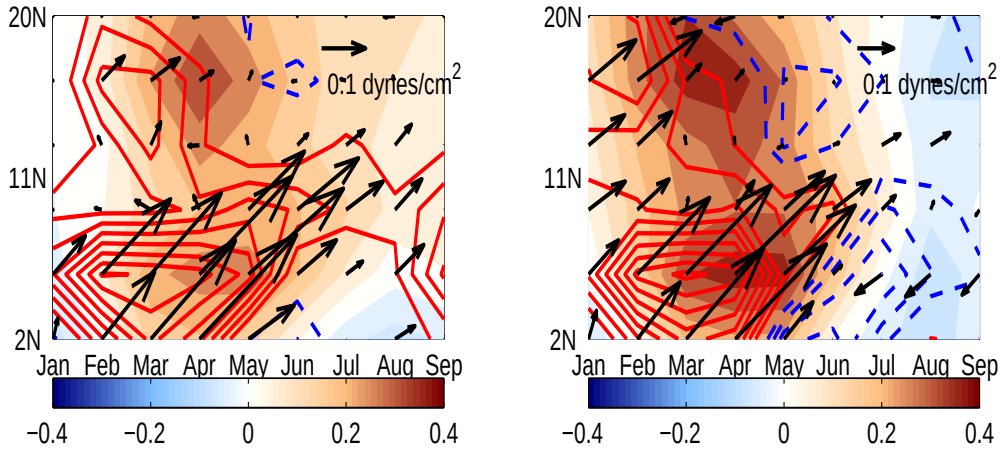

Fig. 25. Composites of residual SST (color), winds (vector), and surface net heat flux (contour) anomalies for MM-ENSO (left) and MM-ONLY (right), displayed as a function of latitude and calendar months. Red contour represents positive value and blue dashed contour represents negative value. The contour interval is 3 W m^{-2}). These residual fields are zonally averaged across the domain (150°E-90°W, 2°N-20°N).

tively, which are displayed as a function of latitude and calendar months in Fig. 25. These composites are done using the residual field zonally averaged across the domain (150°E-90°W, 2°N-20°N) , where the ENSO related variability has been removed by linear regression. Therefore, these composites serve the purpose of revealing the difference in the onset phase of ENSO. There is a prevailing positive heat flux anomaly from Jan. to Sep. in MM-ENSO, which may be responsible for the long persistence of SST and the southwesterly wind anomalies in this group. In contrast, the positive heat flux anomaly in MM-ONLY ends abruptly around May in MM-ONLY and a negative heat flux develops. This leads to a surface cooling and reversed winds in the summer. This suggests that the MM events in MM-ENSO involves stronger thermodynamic ocean-atmosphere feedback than those in MM-ONLY.

The longer persisted winds in MM-ENSO can produce a stronger warming in the subsurface ocean, as these winds can project onto a warm Kelvin wave (i.e. positive thermocline). This is illustrated by Fig. 26 which shows the composites of thermocline depth anomaly as a function of longitude and time at the equator for MM-ENSO (left) and MM-ONLY (middle) and the difference between them (right). Although the thermocline perturbations share similar structure from Aug^{-1} to $July^{0}$, there is a clear difference in the amplitude with the warm anomaly in MM-ENSO being nearly twice of the value of the anomaly in MM-ONLY. As a result, the subsurface oceanic warming in MM-ENSO can lead to surface warming and thus an El Niño, while the subsurface oceanic response in the MM-ONLY is not strong enough to trigger an El Niño.

Fig. 26 also shows that although the difference in thermocline depth anomalies between MM-ENSO and MM-ONLY is largest during the months of the strong MM activity Feb^{0} to Jun^{0}, there is a substantial difference in the earlier season. This suggests that subsurface ocean preconditioning also plays a role in these two different

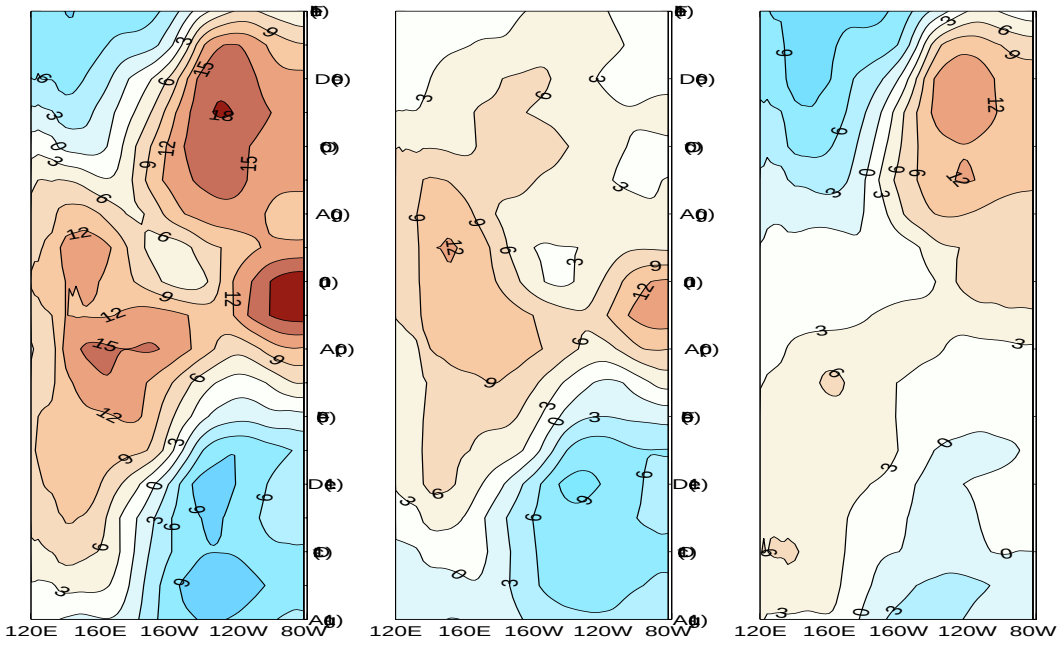

Fig. 26. Composites of thermocline depth anomaly as a function of longitude and time at the equator for MM-ENSO (left) and MM-ONLY (middle), and the difference between them (right).

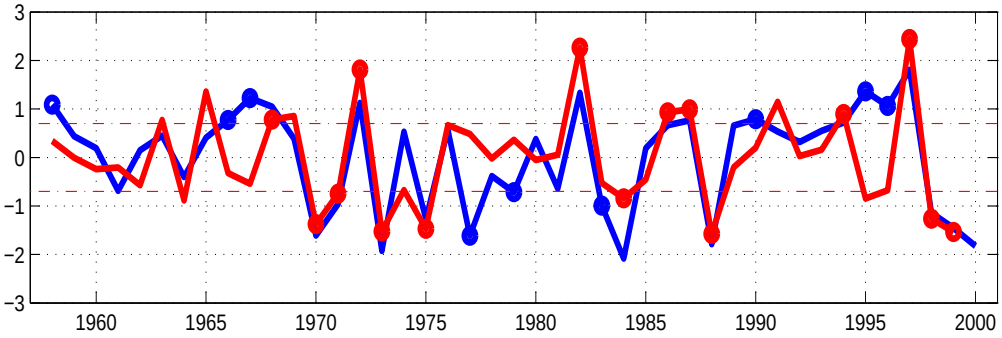

Fig. 27. The time series of FMAM MM τ_x (blue line) and DJF NINO3 index (red line) from the observations. MM-ENSO is indicated by the red dots and MM-ONLY by the blue dots.

types of events. We will revisit this issue in the next chapter.

Is there any observational evidence supporting the hypothesis that the difference in persistence of the MM may play a role in determining the onset of ENSO? To test this idea, we applied a similar analysis to the observed data. The same criterion was used to distinguish MM-ENSO and MM-ONLY events in the observations. The time series of FMAM MM τ_x (blue) and DJF NINO3 index (red) are shown in Fig. 27. Since the total number of El Niño events is limited, both El Niño and La Niña events were used here. There is a total number of 21 ENSO events during the period of 1958-2000. 15 of them are preceded by a MM event (MM-ENSO), indicated by the red dots in Fig. 27. 9 of 24 MM events are not followed by an ENSO event (MM-ONLY), indicated by the blue dots in Fig. 27. Composites of the observed MM τ_x index are shown in Fig. 28, for MM-ENSO and ENSO-ONLY, respectively. As in the model, these observed composites also show longer persisted MM events for MM-ENSO than MM-ONLY. In spite of large uncertainties in these composites because of a small sample size, this result does lend support to our reasoning that the duration of the MM events is a factor in determining whether a MM event can excite ENSO.

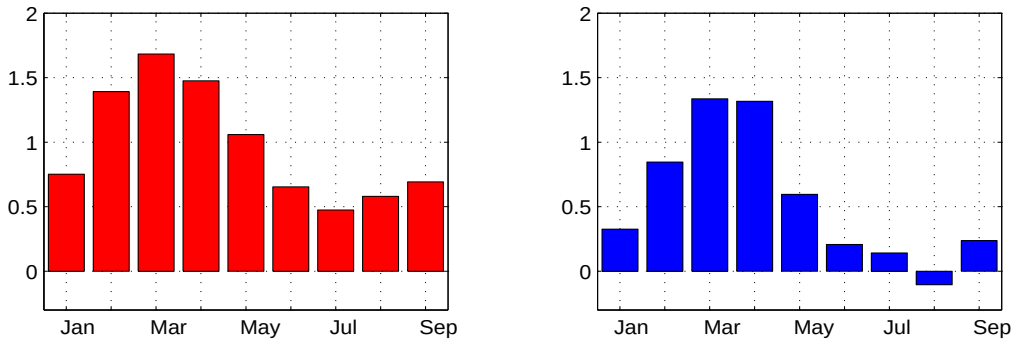

Fig. 28. Composites of the observed MM τ_x index for MM-ENSO (red) and for MM-ONLY (blue).

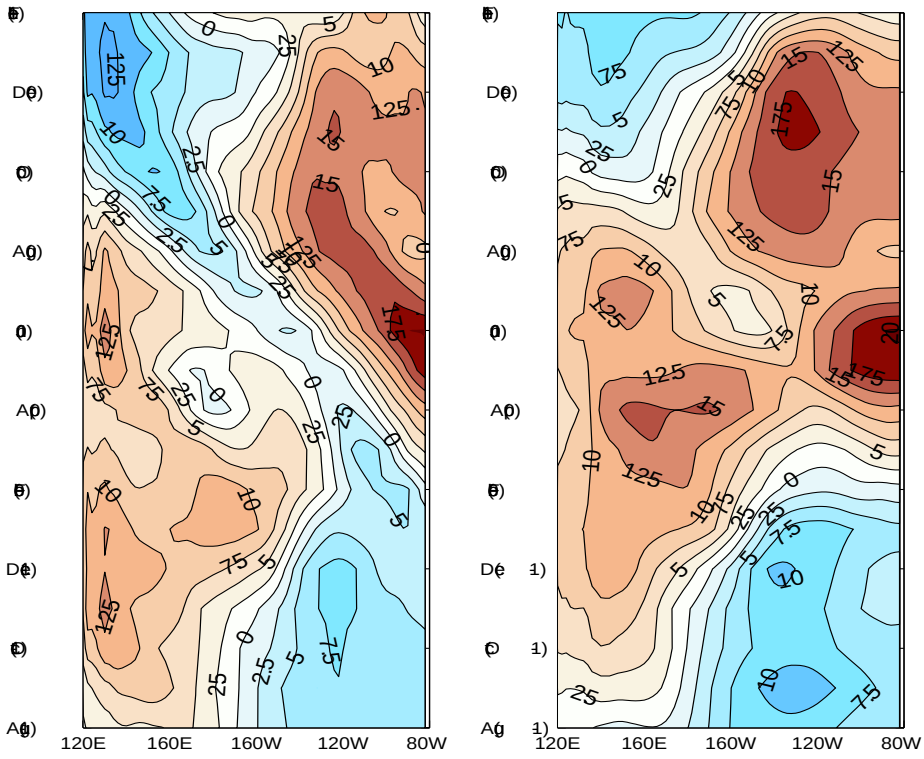

Fig. 29. The longitude-time Hovmöller diagrams for thermocline depth anomalies along 5°N (left panel) and along the equator (right panel) for MM-ENSO.

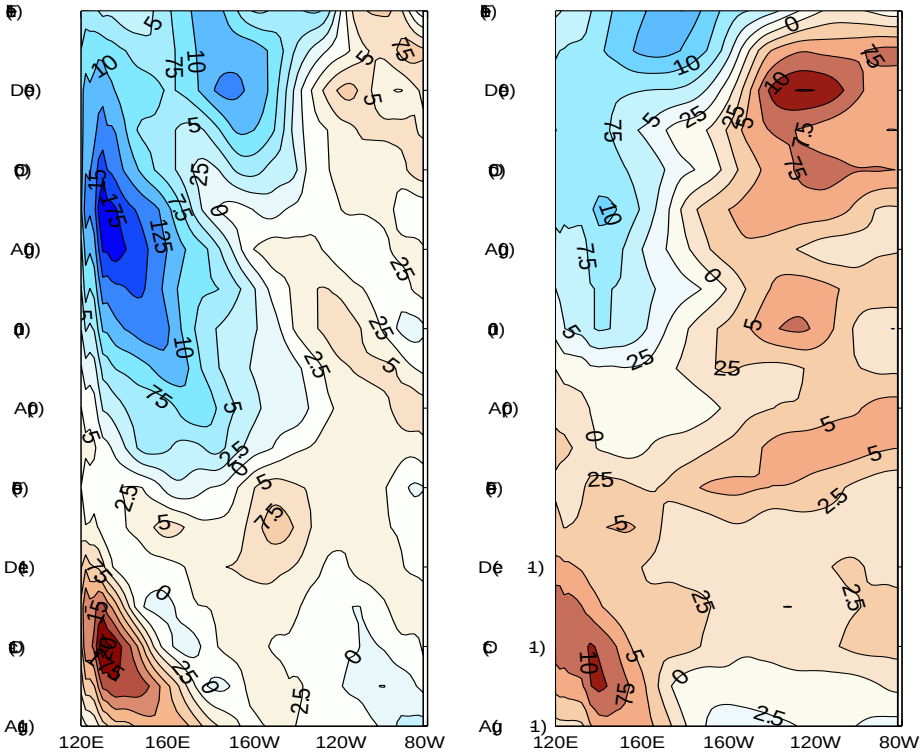

Fig. 30. The longitude-time Hovmöller diagrams for thermocline depth anomalies along 5°N (left panel) and along the equator (right panel) for ENSO-ONLY.

To address the second set of questions, the longitude-time Hovmöller diagrams for thermocline depth anomalies along the equator and along 5°N are shown in Fig. 29 and Fig. 30 for MM-ENSO and ENSO-ONLY, respectively. Both groups exhibit similar general characteristics, namely, the eastward migration tendency in the central Pacific along the equator. But the origin of the eastward propagation signals and their strength are quite different between the two groups.

The signal in MM-ENSO is stronger and seems to originate from west-central Pacific near in dateline. The signal in ENSO-ONLY is weaker and appears to be connected with off-equatorial signal via a wave reflection at the western boundary. There is clear evidence of westward propagation of thermocline depth anomaly associated with Rossby wave along 5°N in ENSO-ONLY, which is absent in MM-ENSO. This feature in ENSO-ONLY appears to be more consistent with the delayed oscillator theory or the recharged mechanism, whereas in MM-ENSO there is less evidence for westward propagating thermocline anomalies off the equator. Instead, a strong thermocline perturbation is generated near the dateline during the development of the MM event in the spring season. This finding suggests that the subsurface memory mechanism may operate better in ENSO events in ENSO-ONLY than in MM-ENSO, indicating that the ENSO events in ENSO-ONLY maybe more self-sustained than those in MM-ENSO.

Other interesting characteristics worth noting is the fact that the thermocline variation in ENSO-ONLY is much weaker than in MM-ENSO, even in the mature phase, but the SST anomaly in the mature phase is as strong as that in MM-ENSO. This raises the issue whether surface heat flux plays a more important role for ENSOs in ENSO-ONLY than MM-ENSO. To shed light on this issue, composites of wind (vector), SST (contour) and heat flux (color) anomalies are compared between the two groups and shown in Fig. 31. In MM-ENSO, it appears that the warming begins

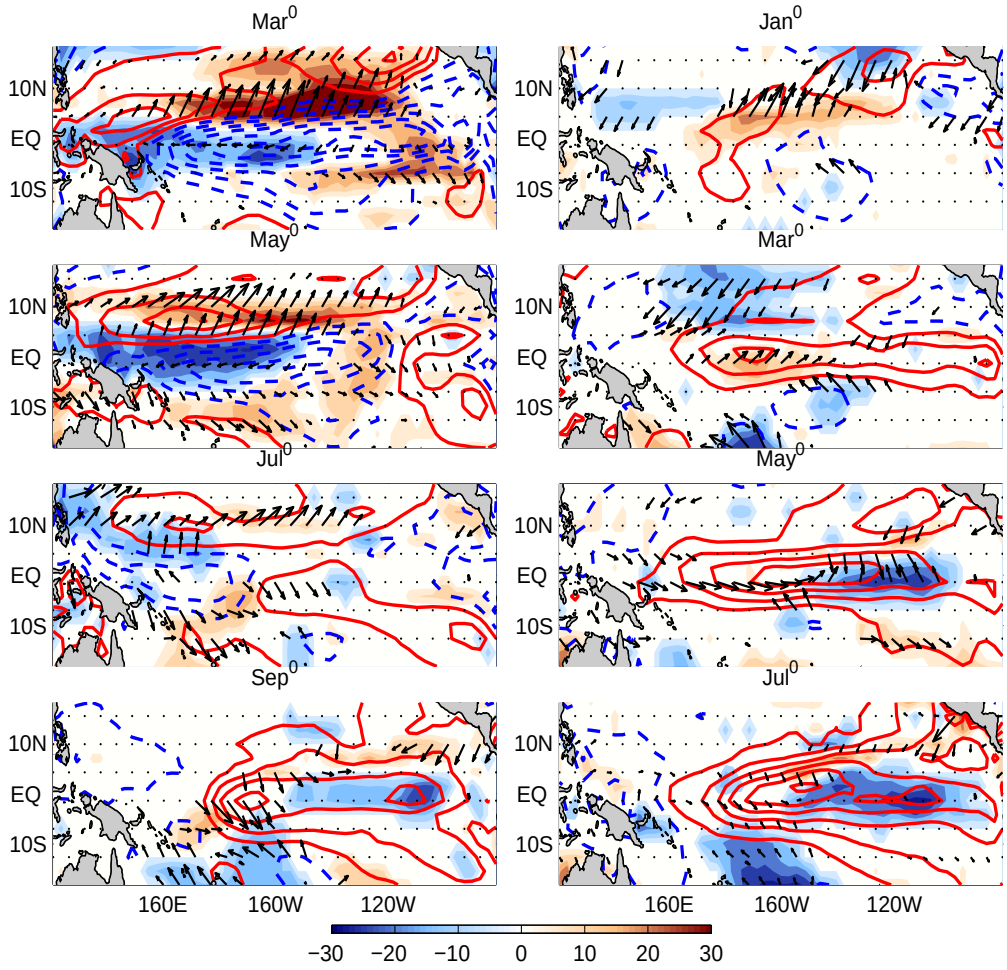

Fig. 31. Composites of wind (vector), SST (contour) and heat flux (color) anomalies for MM-ENSO (left panel) and ENSO-ONLY (right panel).

in the eastern equatorial region and then extends westward, consistent with the results in Fig. 26 which shows a substantial subsurface warming excited by the MM winds during the boreal spring and then propagate eastward, resulting surface warming. In this case, the surface heat flux anomaly near the equator always tries to cool the surface, especially in western Pacific during March to July, and in eastern Pacific in September. The situation is very different for ENSO-ONLY: in Jan^0, a positive heat flux anomaly begins to appear in west-central equatorial Pacific. This positive heat flux forces a positive SST in Mar^0 which then triggers a Bjerknes feedback, leading to the development of an El Niño. Therefore, the onset of El Niño in ENSO-ONLY seems to involve two processes: 1) subsurface ocean memory that brings the off-equatorial warming signal to the equatorial zone, and 2) surface heat flux forcing that initiates the warms in the west-central Pacific. Which of these two processes plays a more dominant role is unclear.

H. Summary and Discussion

In this chapter, we reviewed the observational evidence of the existence of the Pacific Meridional Mode during boreal spring and presented new promising observational evidence that the MM may work as a trigger of ENSO. This leads to the hypothesis that the MM is an important precursor of ENSO.

To test this hypothesis, a new coupled modeling tool consisting of an AGCM (CCM3.6) and a Zebiak-Cane type of reduced gravity ocean model is developed. This model includes realistic atmospheric physics for both coupled feedbacks and internal variability and essential equatorial ocean dynamics for Bjerknes feedback. A long coupled simulation demonstrates the capability of the model of capturing many salient features of the observed ENSO behavior, as well as the MM and its

relationship to the NPO. This good agreement between the model simulation and the observations provides confidence in that the model is able to correctly reproduce mechanisms responsible for ENSO variability.

Our modeling study strongly suggests that the Pacific MM, characterized by the cross-ITCZ SST anomaly gradient and anomalous surface circulation in the north-easterly trade regime with maximum variance in late winter and boreal spring, is inherent to thermodynamic ocean-atmosphere coupling in ITCZ latitudes. Therefore, its existence does not rely on ENSO dynamics, but the feedback between the atmosphere and ocean mixed layer via surface heat flux and SST.

As in the observations, there is a robust relationship between the MM and ENSO in the model simulation. About 66% of the simulated El Niño events are preceded by the MM, which compares well to the 70% of observed ENSO preceded by the MM. This indicates that the connection between the MM and ENSO is more than just coincidental, supporting the hypothesis that the MM works as an important triggering mechanism for the onset of ENSO. But as complicated as nature, not every MM event associates with ENSO, and conversely not every ENSO corresponds to an MM event. Over the 400-year coupled model simulation, we found: (1) 65 El Niño events out of 99 (66%) are preceded by MM events. The onset of this group of El Niños is triggered by the zonal wind anomaly associated with meridional mode just north of the equator that causes deepening of the thermocline and warming of the surface temperature in the eastern equatorial Pacific; (2) 34 El Niño events out of 99 (34%) are independent of MM. The onset of this group of El Niños obeys the delayed oscillator or the recharged oscillator mechanism, but surface heat flux anomaly forming in the west-central tropical Pacific also seems to play a role in triggering this group of El Niños. (3) 46 meridional mode events out of 111 do not lead to El Niño. These MM events seem to have shorter duration than other meridional mode events. This

combined with the fact that the subsurface ocean condition is less favorable for the development of surface warming makes these MM events ineffective of producing warming in the eastern equatorial Pacific.

The SST anomaly associated with the MM is most correlated with the southern component of the NPO, not so much with the northern one both in the model and in the observations. The relationship between the meridional mode and El Niño events appears to be much more robust than the direct relationship between the NPO and ENSO. This indicates that the NPO may provide one potential mechanism that excites the meridional mode, as postulated by (Vimont et al., 2003a,b; Chiang and Vimont, 2004). The meridional mode seems to work as a bridge connecting the internal atmospheric variability and ENSO. Other mechanisms may also exist.

The analysis used in this study to identify the meridional mode consist of removing those springs immediately following ENSO events, and then apply statistical analysis on the residual fields. However, the results change little of we used the linear regression technique as in (Chiang and Vimont, 2004). This insensitivity of the result to the analysis technique indicates the robustness of these findings.

The focus of the study in this chapter is the existence of the MM and identification of its relationship to ENSO. Although an extensive statistical analysis was used to explore the MM-ENSO relationship, the causality between them needs to be studied more carefully with the aid of more physically oriented model experiments. In particular, we have not been able to distinguish exactly what the effect of the ocean is in responding to the MM related atmospheric forcing, and whether this ocean response is capable of producing ENSO. Therefore, in the following chapter, we discuss results from additional ocean model-alone experiments and demonstrate the oceanic contribution in linking the MM to ENSO.

CHAPTER IV

INVESTIGATING PHYSICAL MECHANISMS FOR FORCING ENSO VIA INTERNAL ATMOSPHERIC VARIABILITY – THE ROLE OF OCEAN DYNAMICS

A. Introduction

Tropical ocean dynamics have been known to play an important role in ENSO. From an oceanic point of view, ENSO can be explained as the tropical ocean's response to changes in the winds. Numerous studies since 1970s have unambiguously demonstrated that equatorial ocean adjustment to changes in the trade winds is one key ingredient of ENSO physics (see Philander (1990) and JGR special volume, 1998 for a comprehensive review). The intent here is not to repeat what we already know, but to focus on the issues concerning the relationship between the MM and ENSO. One particular question to be explored is what role ocean dynamics has in the link between the MM and ENSO.

Recall that the results from the previous chapter show that the majority of El Niño events in the model and the observations are preceded by an MM event. However, not every MM event is followed by an El Niño. We speculate that the differences between these two groups of events are attributed to two factors: 1) The MM events that lead to the development of El Niño persist through the boreal summer, while the other MM events that are not followed by the development of El Niño are short-lived; 2) the subsurface ocean preconditioning gives a more favorable state for El Niño to develop in the former than in the latter. Both of these differences relate to how the ocean responds to the winds associated with the MM. Therefore, the objective of this chapter is to conduct a further investigation of the oceanic response via a set of

stand-alone ocean model experiments.

The rationale of using stand-alone ocean model is, assuming that a model forced by the wind stresses and surface heat fluxes from the coupled simulation can reproduce the oceanic variability of the coupled simulation, then we can decompose these forcing fields into two parts: ENSO and non-ENSO related forcing. Stand-alone ocean model runs are then conducted using the ENSO and non-ENSO related forcing. The response to the ENSO-related forcing describes the oceanic component of the Bjerknes feedback that is responsible for full development of ENSO cycle. The response to the non-ENSO forcing which contains the MM variability contains information about how ENSO is triggered. It is this latter part that will be analyzed in detail to compare the response of the ocean to different forcing in the two cases. As in the previous chapter and Chiang and Vimont (2004), we assume that the ENSO-related forcing is linearly related to NINO3 SST index, while the non-ENSO part is the residual between the total and the ENSO related forcing. This linear regression technique has been shown to work well in separating ENSO and non-ENSO variability in Chiang and Vimont (2004) and in the previous chapter. Therefore, we expect this technique will be effective for the stand-alone ocean model experiments.

In addition to these experiments, we further conduct the stand-alone ocean experiments using surface forcing fields from CCM3-ML and CCM3-SC simulations described in Section C of Chapter III. Since these runs contain no ENSO variability by definition, one does not need to be concerned with removing any ENSO related forcing. Therefore, these runs are ideal for addressing the issue of whether the non-ENSO related forcing can produce any El Niño-like variability, thereby providing an independent confirmation of the findings from previous experiments.

This chapter is organized as follows: Section B describes the model and the experiments that will be conducted. Section C demonstrates that the stand-alone

ocean model experiment can reproduce the coupled simulation and represents a detailed mixed-layer heat budget analysis of the ocean model experiment. Section D examines the ocean model response to the non-ENSO related forcing. Section E discusses the results from the ocean model experiments with forcing fields derived from CCM3-ML and CCM3-SC coupled simulations. Section F summarizes the major findings.

B. Ocean Model and Experiment Setup

The ocean model is identical to that used in CCM3-RGO coupled simulation and has the same parameter settings. The setup of the forcing fields is also identical to that of the coupled model, except that monthly mean values are used in the uncoupled experiments, while instantaneous values at every coupled step (once per day) are used in the coupled run. All the forcing fields used in the uncoupled ocean model runs are the monthly mean values derived from the coupled simulation, including surface wind stresses and surface heat fluxes.

The following is a brief description of each experiment:

1. Uncoupled-Control Run: 400-year ocean model simulation forced with wind stress and heat fluxes from the CCM3-RGO coupled simulation. This simulation is used to validate the model against the coupled simulation to examine the extent to which the uncoupled experiment can reproduce the coupled simulation. A mixed-layer heat budget analysis will be applied to gain understanding of the dominant oceanic processes in ENSO variability.

2. ENSO and non-ENSO Related Forcing Experiments (Hereafter ENSO-RGO and Residual-RGO Run, respectively): Identical setup to the Uncoupled-Control, except that the forcing fields for the ENSO-RGO Run contain the part that is

linearly related to the NINO3 SST, while the non-ENSO forcing is used for the Residual-RGO Run.

3. CCM3-ML Forcing Experiment (Hereafter CCM3-ML-RGO Run): 100-year ocean model simulation forced with wind stress and heat fluxes from the CCM3-ML coupled simulation. The CCM3-ML run completely eliminates any ENSO-related variability by design. Thus, this experiment allows a clean delineation of oceanic response to non-ENSO related forcing which includes the MM-related variability.

4. CCM3-SC Forcing Experiment (Hereafter CCM3-SC-RGO Run): 100-year ocean model simulation forced with wind stress and heat fluxes from the CCM3-SC coupled simulation. The variability simulated by the CCM3-SC run is entirely driven by the atmospheric internal dynamics. Therefore, this experiment gives an estimate of the oceanic response driven by internal atmospheric variability.

C. Uncoupled-Control Experiment

The Uncoupled-Control Run reproduces very well the simulated ENSO variability from the 400-year CCM3-RGO experiment. The correlation of NINO3 indices between the two experiments is 0.97 for the entire 400-year record. Fig. 32 shows composite of three types of events identified using the same criteria as in the CCM3-RGO coupled simulation. As can be seen, the Uncoupled-Control Run successfully reproduces the evolution of the events, with the exception that the amplitude of the SST anomaly is slightly larger in the uncoupled run than in the coupled run. This is expected because the lack of coupling between the ocean and atmosphere will tend to lead an overestimation of the variance by reducing thermal damping, as shown by Barsugli and Battisti (1998). But overall this effect is small in the ENSO region, as

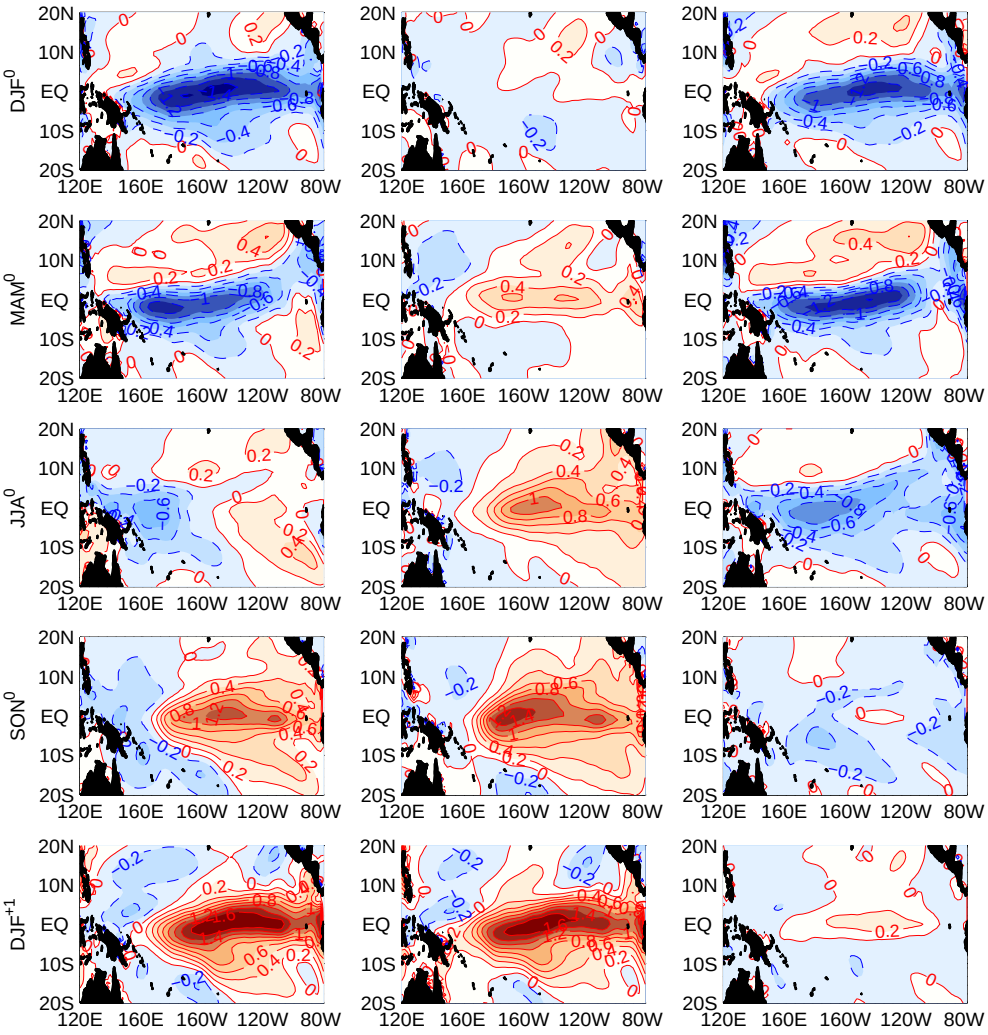

Fig. 32. Composite maps of seasonally averaged SST anomalies of the Uncoupled-Control Run for MM-ENSO (left panel), ENSO-ONLY (middle panel) and MM-ONLY (right panel) from DJF^0 (the first row), MAM^0 (the second row), JJA^0 (the third row), SON^0 (the fourth row) and DJF^{+1} (the fifth row), respectively.

shown by the composite. We therefore conclude that the uncoupled experiments can be used to diagnose dominant oceanic processes in ENSO evolution.

To identify the dominant oceanic processes in different types of events, we perform a mixed-layer heat budget analysis. The model SST tendency consists of contributions from horizontal and vertical advection, diffusion and heat-flux forcing,

$$\frac{\partial T}{\partial t} = Q_{x-adv} + Q_{y-adv} + Q_{z-adv} + Q_{diff} + Q_a. \tag{4.1}$$

where $Q_{x-adv} = -u\frac{\partial T}{\partial x}$, $Q_{y-adv} = -v\frac{\partial T}{\partial y}$ and $Q_{z-adv} = -w_e H(w_e)\frac{T-T_{sub}}{H_{mix}}$ are zonal, meridional and vertical advection of heat, $Q_{diff} = \kappa\nabla^2 T$ is the diffusion and $Q_a = \frac{Q}{\rho_0 C_p H_{mix}}$ is surface heat flux forcing from the atmosphere. where ρ_0 is the water density; C_p is specific heat of water at constant pressure; T_{sub} is the entrainment temperature beneath the base of the mixed layer H_{mix}; H is the Heaviside step function($H(x) = 1$ if $x > 0$, $H(x) = 0$, if $x < 0$); u and v are velocities of the upper ocean; and Q is the net heat flux going into the upper ocean.

The anomalous vertical advection $Q_{z-adv} - \bar{Q}_{z-adv}$, where $\bar{Q}_{z-adv}$ denotes the mean annual cycle, can be further divided into three terms:

$$Q_{z-adv} - \bar{Q}_{z-adv} = -{w_e}'\frac{\bar{T} - \bar{T}_{sub}}{H_{mix}} - \bar{w_e}\frac{T' - T'_{sub}}{H_{mix}} - {w_e}'\frac{T' - T'_{sub}}{H_{mix}}. \tag{4.2}$$

where the first term on the right hand side represents anomalous upwelling against mean vertical stratification; the second term represents mean upwelling against anomalous vertical temperature gradient, and the third term represents nonlinear contribution which is small in the model and will not discussed.

Composite analysis is applied to the SST tendency equation (4.1) over the NINO3 region for each of the three types of events. Since we are particularly interested the two cases where in one case the MM is followed by ENSO (MM-ENSO) and in the other it is not (MM-ONLY), we contrast the dominant oceanic processes contributing to

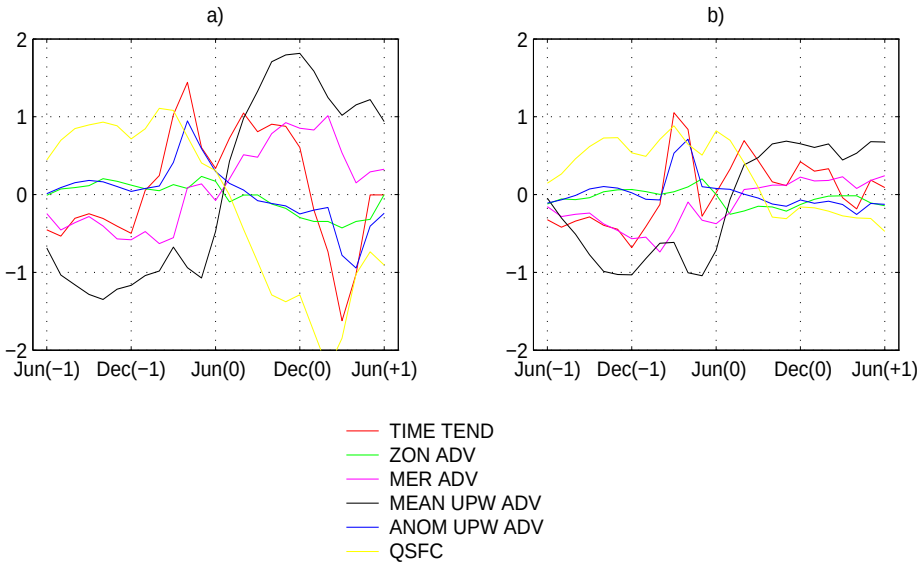

Fig. 33. Components of the heat budget averaged over the NINO3 region for MM-ENSO (a) and MM-ONLY (b). The thermodynamic terms shown represent temperature tendency (labeled TIME TEND), zonal advection (ZON ADV), meridional advection (MER ADV), advection by mean upwelling (MEAN UPW ADV), advection by anomalous upwelling (ANOM UPW ADV), and anomalous surface heat flux (QSFC). Units of the y-axis are $\times 10^{-7\circ} C/s$.

SST changes in Fig. 33. Prior to Dec(-1), the balance in the mixed layer heat budget appears to be similar in both cases. The most dominant oceanic contribution to the heat budget is the mean upwelling term (black) which maintains an anomalous cold ocean state. From Dec(-1) to Apr(0), there is an abrupt increase in the SST tendency (red) in both cases, which coincides with the onset of the MM events. The dominant oceanic contributions to this warming tendency are from anomalous upwelling (blue) and meridional advection (magenta).

Physically, this may be understood as follows: The southwesterly wind anomaly associated with the onset of the MM produces an equatorward and eastward Ekman flow which acts to reduce equatorial upwelling and at the same time transport the off-equatorial warm surface water into the cold tongue region. After Apr(0), the SST tendency behaves differently in the two cases. In the case where the MM is followed by an El Niño, the SST tendency remains positive through boreal summer, while in the case where the MM does not lead to an El Niño, the SST tendency drops below zero in May(0) and Jun(0) and then remains weak. This different behavior is consistent with the previous notion that the MM events persist longer in MM-ENSO than in MM-ONLY, so that they can maintain a positive SST tendency throughout the boreal spring and summer and produce a surface warming.

To further understand how anomalous upwelling advection works, we decompose the surface current into a geostrophic part (u_g) and an Ekman part (u_e). The geostrophic part results from large-scale oceanic adjustment to changes in the winds that can be located in a remote location and may take a longer time to become effective, while the Ekman part of the response is directly related to the local winds. The result shows that the anomalous upwelling is primarily controlled by the local wind driven Ekman flow with little contribution from the geostrophic currents.

Following the peak of the MM events in MAM(0), there is an abrupt increase

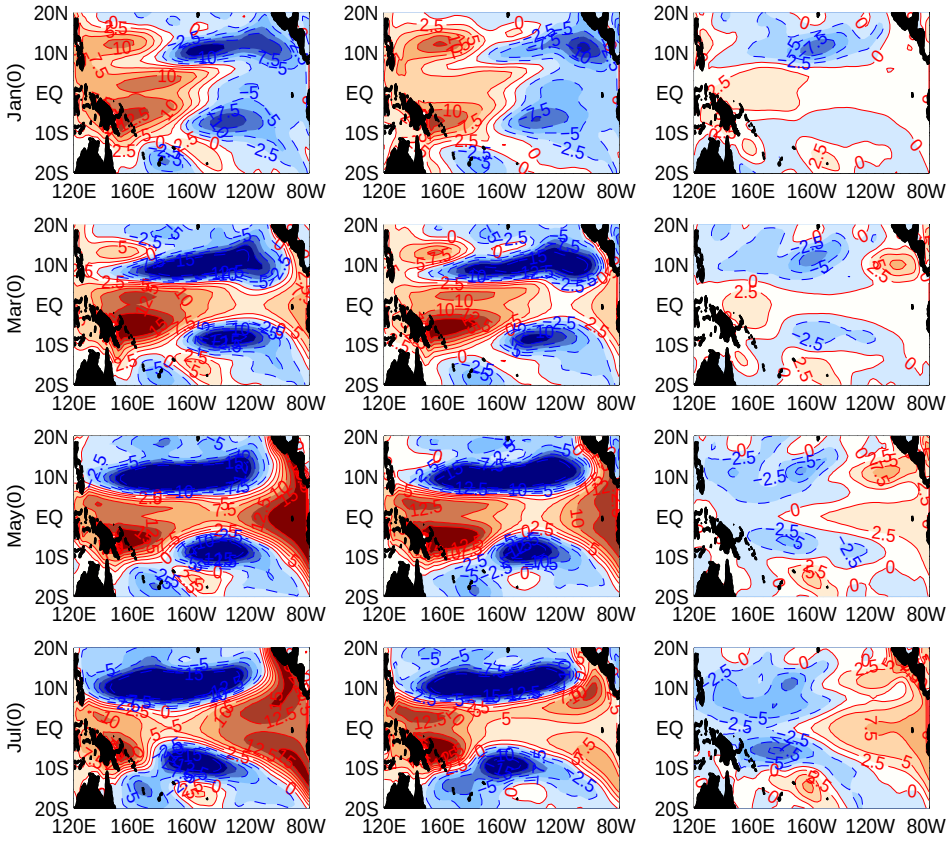

Fig. 34. Composites of thermocline anomaly for MM-ENSO (left) and MM-ONLY (middle), and the difference between them (right) in Uncoupled-Control experiment from Jan(0) (the first row), Mar(0) (the second row), May(0) (the third row) and Jul(0) (the last row).

in anomalous vertical heat advection due to changes in stratification, suggesting that the winds associated with the MM not only have an immediate effect on the local upwelling, w'_e, but also can induce a change in the thermocline depth with a longer delay. In fact, this process becomes the dominant oceanic term contributing to the positive SST tendency after Jul(0). Obviously, there is a marked difference in the amplitude of this oceanic processes in these two groups of events with the amplitude in MM-ENSO much larger than that in MM-ONLY. Physically, this difference may be attributed to a number of factors. First, the longer persisted westerly winds in MM-ENSO can cause a stronger thermocline perturbation, resulting in a stronger change in stratification. Second, there may be more heat build-up in the western tropical Pacific basin in MM-ENSO, so that the heat may be more readily released to the eastern equatorial basin. This difference in the ocean preconditioning effect is shown in Fig. 34. It is clear that the thermocline depth is anomalously deeper in western tropical Pacific basin in MM-ENSO than in MM-ONLY. Lastly, the spring warming in MM-ENSO can trigger the Bjerknes feedback, which primarily operates via the mean upwelling against the anomalous vertical temperature gradient. Therefore, a significant portion of the warming induced by the mean upwelling term can come from the Bjerknes feedback. To isolate the Bjerknes effect from the analysis, we next turn to the Residual-RGO experiment.

D. Residual-RGO Experiment

The canonical evolution of SST for the MM-ENSO and MM-ONLY types of events in the Residual-RGO experiment are shown Fig. 35. Since ENSO-related forcing has been removed, it is no surprise that the amplitude of the SST is weaker than that in the Uncoupled-Control Run. But even without the ENSO-related forcing,

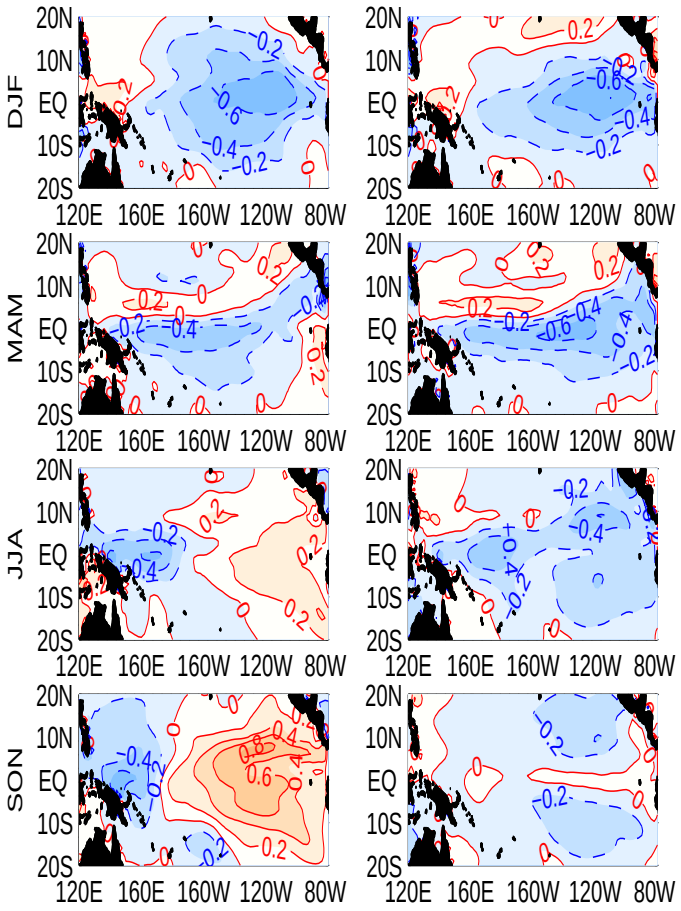

Fig. 35. Composites of seasonally averaged SST for MM-ENSO (left panel) and MM-ONLY (right panel) in Residual-RGO experiment from DJF^0 (the first row), MAM^0 (the second row), JJA^0 (the third row), and SON^0 (the last row), respectively.

the SST in MM-ENSO develops a warm SST anomaly off the coast of Ecuador and Peru in MAM(0). The most striking difference between the two cases occurs after JJA(0), where the MM-ENSO shows considerable warming in the eastern equatorial region, while the MM-ONLY barely shows any. A comparison between the SST anomalies in the Residual-RGO and the Uncoupled-Control experiments during these seasons shows a strong similarity between the two cases, suggesting that the warming of the sea surface in these season is predominantly attributed to the non-ENSO related forcing.

To further illustrate this, Fig. 36 shows the longitude-time Hovmöller diagrams for thermocline anomalies along the equator and the equatorial τ_x averaged over 5°S-5°N for MM-ENSO and MM-ONLY, respectively. During the development of the MM from Jan(0) to May(0), a positive τ_x anomaly appears across the basin in both cases, kicking off a positive, eastward propagating thermocline depth anomaly. The major difference between the two cases does not occur during the development phase of the MM, but during the decay phase of the MM. In the case of MM-ENSO, the positive τ_x anomaly near the dateline lingers through the boreal summer and fall, which causes the positive thermocline depth to persist through these seasons and produce warm SST anomalies. In contrast, the positive τ_x anomaly in MM-ONLY decays more rapidly and reverses its sign after May(0), thereby producing insignificant warming in equatorial SST. Therefore, the results of the Residual-RGO experiment supports the view that for the MM to excite ENSO, it is necessary that the associated westerly winds persist through the summer and fall, so that a substantial warm SST in the eastern equatorial region can be generated.

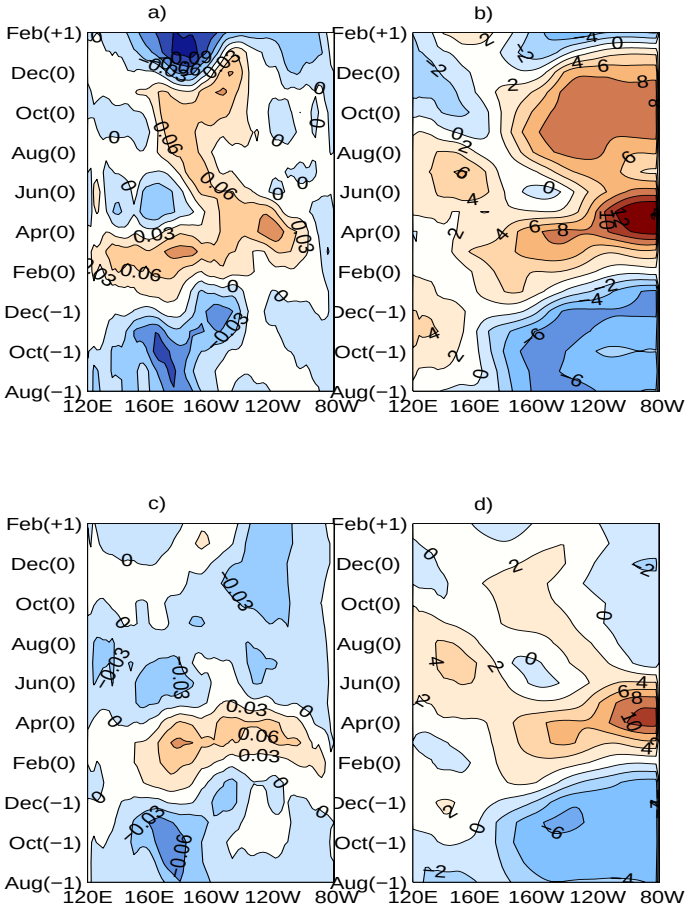

Fig. 36. Equatorial τ_x and thermocline anomaly in Residual-RGO Run as a function of longitude and time for the Pacific basin, a) τ_x and b) thermocline anomaly for MM-ENSO. c) and d): Same, but for MM-ONLY.

E. CCM3-ML-RGO and CCM3-SC-RGO Experiments

The previous experiment, based on the linear removal of ENSO, may draw criticism that ENSO-related variability can not be completely removed, thus contaminating the interpretation of the result. In particular, the long persistence of the MM in MM-ENSO could be due to the residual ENSO effect. To independently check this result, it is desirable to repeat the RGO experiment with a set of forcings where ENSO signal is eliminated by removing relevant physical processes, not by statistical techniques. For this reason, we conduct CCM3-ML-RGO and CCM3-SC-RGO experiments. From the previous discussion, we have learned that CCM3-ML coupled simulation captures the MM variability, while CCM3-SC simulation does not capture the MM, because the MM is inherent to thermodynamic ocean-atmosphere coupled system. Therefore, if the MM does lead to the development of ENSO, as shown in the Residual-RGO experiment, then we expect CCM3-ML-RGO experiment to produce ENSO-like variability. Furthermore, we expect that most of the ENSOs will follow the MM in this experiment. On the other hand, such a result is not anticipated from the CCM3-SC-RGO experiment, since MM activity is absent in the CCM3-SC simulation.

Fig. 37 shows the first SST EOF pattern and the associated time series along with its seasonal variation from the 100-year CCM3-ML-RGO simulation. It is evident that an ENSO-like variability is present. Furthermore, its phase-locking to the annual cycle appears to be in a very good agreement with the observed ENSO and the CCM3-RGO simulated ENSO, suggesting again that the MM plays an important role in determining the seasonality of ENSO. It may be worth noting that the amplitude of the SST anomaly is even larger than that of the CCM3-RGO simulation, despite the fact that the Bjerknes feedback is absent. This may be explained by the following

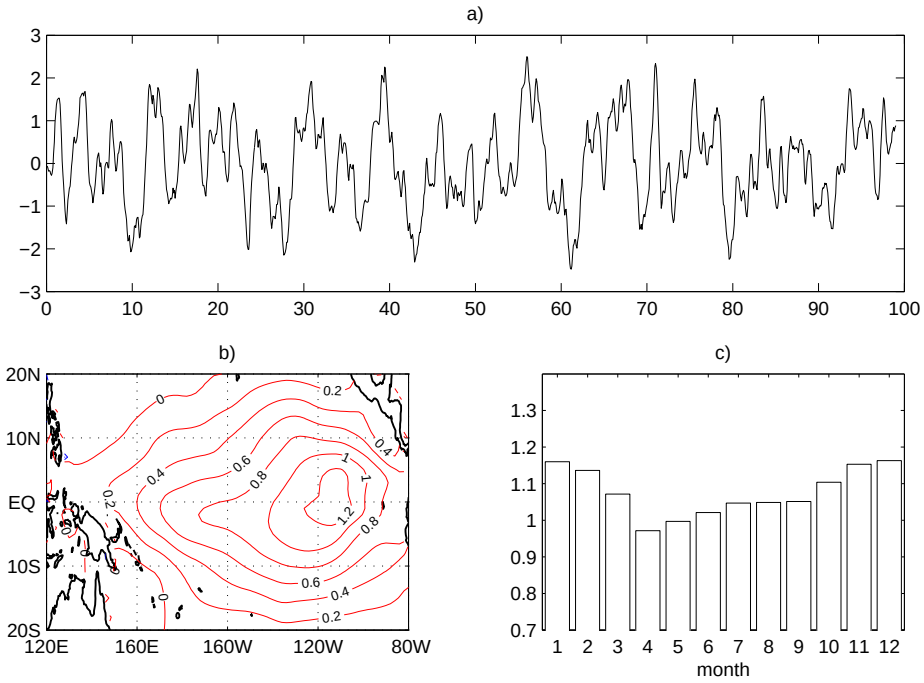

Fig. 37. (a) The time series associated with the first SST EOF from the CCM3-ML-RGO Run, (b) the first SST EOF pattern and (c) seasonal phase-locking of the NINO3 index.

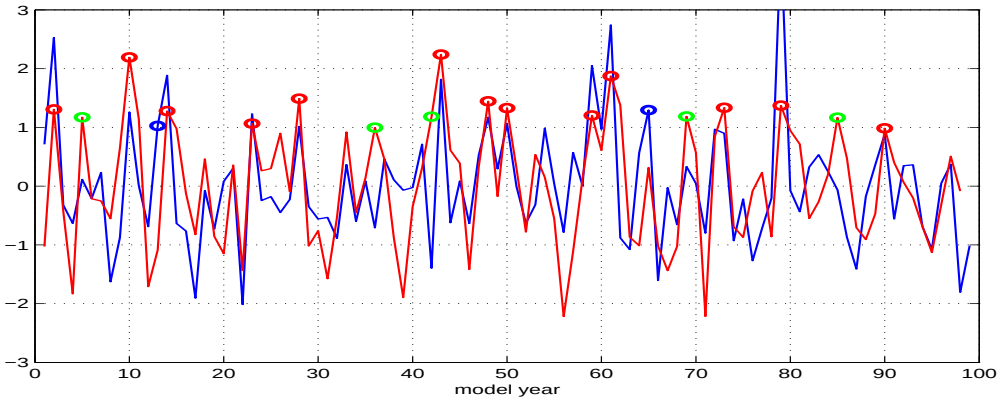

Fig. 38. Normalized time series associated with the first EOF of τ_y from CCM3-ML-RGO Run averaged over FMAM (blue line) and normalized NINO3 index averaged over DJF (red line). Red dots indicate MM-ENSO, green dots indicate ENSO-ONLY, and blue dots indicate MM-ONLY.

reasons: 1) the CCM3-ML simulation tends to overestimate the MM related SST and wind variance, because of the absence of oceanic heat transport that can act as a damping to SST, 2) the stand-alone ocean model simulation also tends to overestimate SST variability because of the absence of damping effect. The de-correlation time scale of the ENSO-like SST variability in the CCM3-ML-RGO simulation is about 12 months, this is longer than that simulated by the CCM3-RGO coupled run, indicating that the ENSO-like variability tends to have more energy in low-frequency bands. This may be caused by the red-spectrum response of the CCM3-ML coupled system.

To explore the relationship between the MM and ENSO in the CCM3-ML-RGO simulation, similar analysis used in the CCM3-RGO simulation is applied to the 100-year model data here. First, the time series of the first EOF of τ_y during FMAM is used as an index for the MM variability. As demonstrated in the previous chapter, this index gives a very good measure of the MM variability in the CCM3-ML coupled model (Fig. 38). The relationship between this MM index and the DJF NINO3 index

is then examined. As shown in Fig. 38, the two indices are highly correlated with a correlation value of 0.52 which significant at 99% level. If one uses the same criteria to classify the different types of ENSO and MM events as in CCM3-RGO simulation, then 72% of the El Niños are preceded by MM events and only 13% of the MM events (2 out of 15) are not followed by an El Niño. This result reveals an even tighter relationship between the MM and ENSO in the CCM3-ML-RGO simulation than in the CCM3-RGO simulation.

To demonstrate how ocean dynamics can modify the SST response of the CCM3-ML coupled system, we contrast the composite of SST evolution from the CCM3-ML and CCM3-ML-RGO simulation for all the MM-ENSO events in Fig. 39. In the absence of ocean dynamics, the SST anomaly in the CCM3-ML simulation shows a warm SST anomaly emanating from the northeastern part of Pacific basin into the tropics from DJF(0) to JJA(0). Accompanying this warm anomaly is a weak cold anomaly occupying much of the area south of the ITCZ. This pattern of SST resembles strongly the SST anomaly associated with the MM (Fig. 23 in the previous chapter), and it reaches its peak in MAM(0) as the MM does. In the absence of the ocean dynamics, these SST anomalies simply fade away in the following seasons. The situation is drastically different in the presence of ocean dynamics. As can be seen from Fig. 39, in response to the MM related wind forcing a warm SST anomaly begins to develop in the eastern equatorial region, expand westward and intensify as the season progresses. This evolution of SST is similar to that of the MM-ENSO events in the Residual-RGO simulation, except that amplitude of the SST anomaly is much stronger in the CCM3-ML-RGO simulation.

The similar RGO experiment with forcing derived from the CCM3-SC simulation reveals a different response. The SST EOF does not resemble anything and has negligible amplitude (Fig. 40b). The time series associated with the first EOF pattern

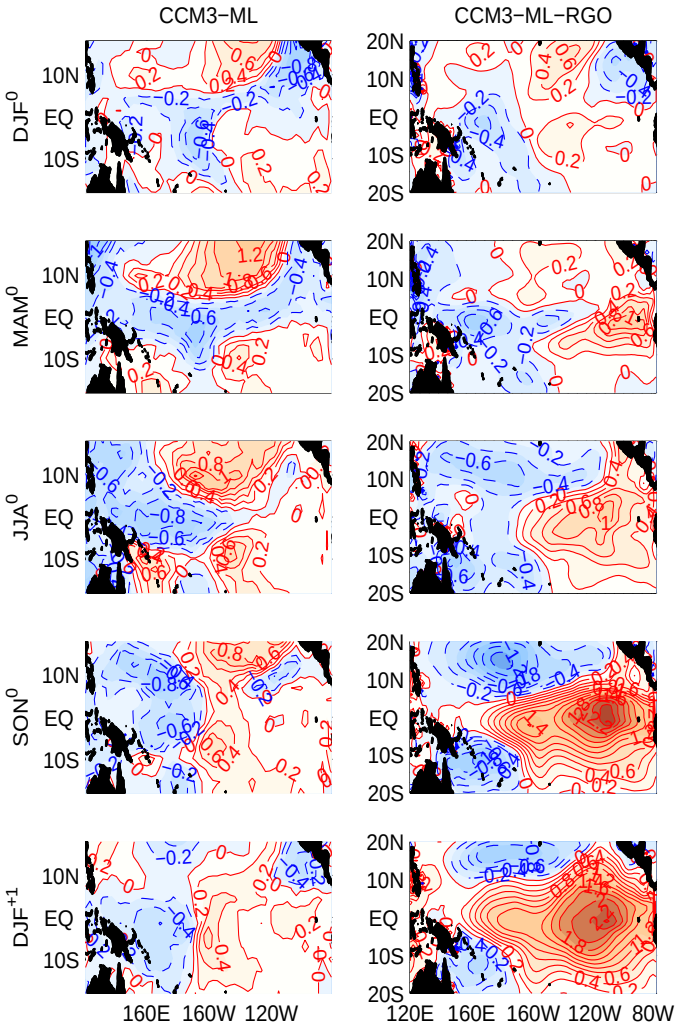

Fig. 39. Seasonally averaged SST anomalies of MM-ENSO for CCM3-ML run (left panel) and for CCM3-ML-RGO Run (right panel) from DJF^0 (the first row), MAM^0 (the second row), JJA^0 (the third row), SON^0 (the fourth row) and DJF^{+1} (the last row).

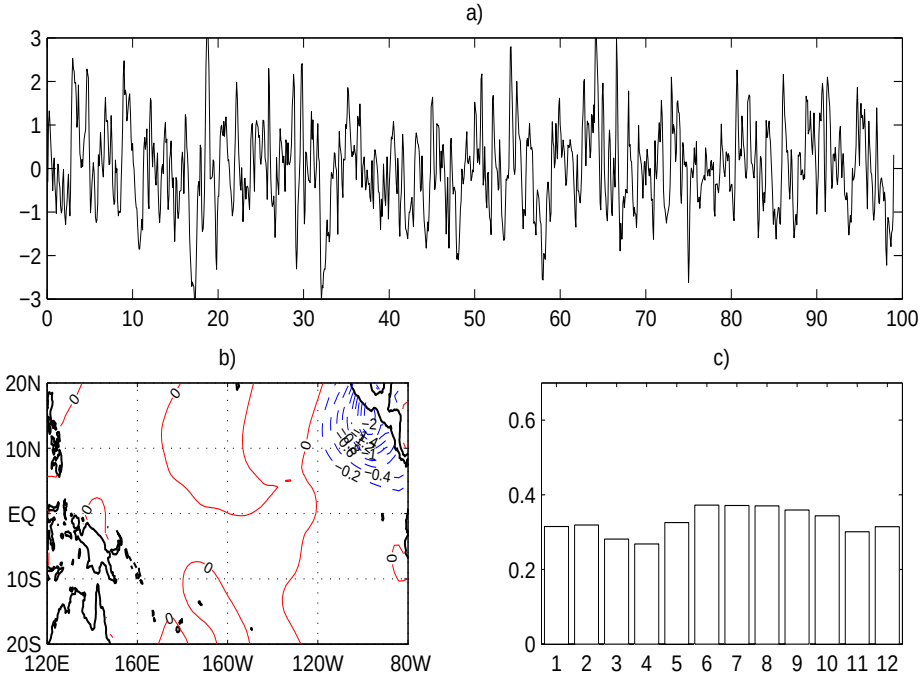

Fig. 40. a) The time series associated with the first SST EOF from the CCM3-SC-RGO Run, b) the first SST EOF pattern and c) seasonal phase-locking of the NINO3 index.

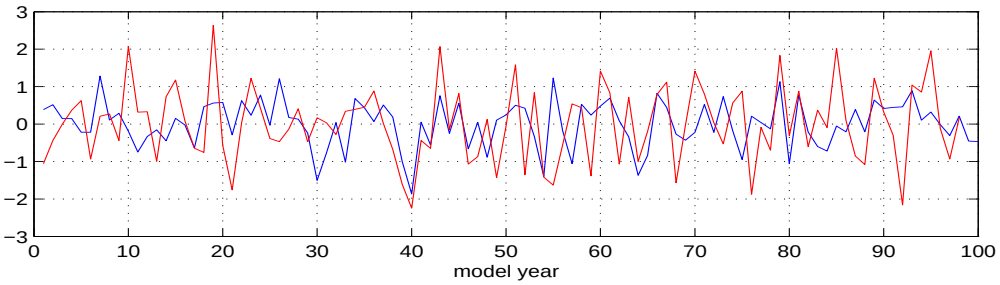

Fig. 41. Normalized time series associated with the first EOF of τ_y from CCM3-SC-RGO Run averaged over FMAM (blue line) and normalized NINO3 index averaged over DJF (red line).

of SST shows no evidence that the equatorial SST variability is phase-locked to the boreal winter (Fig. 40c). Using the time series of the first EOF of τ_y as an index for the MM, we find essentially no correlation (0.17) between this index and NINO3, as shown in Fig. 41, suggesting that the weak SST variability in this experiment is governed by different processes.

In summary, the results from these experiment provides independent supporting evidence that the MM can lead to the development of ENSO.

F. Summary and Discussion

The results presented in this chapter demonstrate that the stand-alone ocean model experiments forced with surface winds and heat fluxes from the coupled simulations provide a useful tool to gain further insight into the relationship between the MM and ENSO. The Uncoupled-Control experiment shows that the two dominant oceanic processes responsible for the MM induced SST change are the anomalous upwelling against mean vertical stratification and the mean upwelling against anomalous vertical temperature gradient. The former affects the SST immediately after the onset of the MM because it is related surface Ekman flow response, whereas the latter affects the SST with a longer delay because it relies on thermocline adjustment. The extent to which the latter can affect the SST depends on how long the event lasts. The Residual-RGO experiment show that the persistence of the MM is the key that distinguishes MM-ENSO events from MM-ONLY events. The longer persistence of the MM in MM-ENSO causes the thermocline perturbation to persist through the boreal summer and fall and produces sufficient surface warming for El Niño to develop. Further RGO experiments using surface forcing derived from the CCM3-ML and CCM3-SC simulation provide an independent confirmation that the

MM can indeed lead to the development of ENSO.

In addition to revealing the relationship between the MM and ENSO, there are other interesting findings from the stand-alone ocean model experiments that have not been discussed extensively in this chapter. For example, another set of experiments, with the ocean model forced with surface winds only and heat fluxes only from the coupled CCM3-RGO simulations, demonstrate that the experiment forced with surface winds only produces a broader SST pattern than the experiment forced with surface heat fluxes. This may suggest that the Ekman advection tends to broaden the SST response while the heat flux intends to make it more confined near the equator. Furthermore, an examination of the ENSO-related forcing experiment (ENSO-RGO experiment) indicates that the Bjerknes feedback starts to make a significant contribution to the development of El Niño in MM-ENSO from Aug(0) and its effect tends to be confined in the deep tropics within 10°S-10°N. Outside the deep tropics, the SST change associated with the Bjerknes feedback tends to work against that induced by the non-ENSO forcing. This suggests that the meridional extent of the SST anomaly may be determined by the relative strength of the Bjerknes feedback and non-ENSO related forcing. In terms of explained variance, assuming that SST variations induced by the ENSO related and non-ENSO related forcing are independent, then the ENSO-related forcing explains 42% of the total NINO3 SST variance. However, caution must be excised while interpreting these ocean model experiments, as nonlinearity and active ocean-atmosphere feedback have not been taken into consideration.

CHAPTER V

INVESTIGATING PHYSICAL MECHANISMS FORCING ENSO VIA INTERNAL ATMOSPHERIC VARIABILITY – UTILIZATION OF A NOISE FILTER

A. Introduction

As shown in the previous chapters, the majority of the El Niño events appear to be preceded by Pacific MM events. Since internal atmospheric variability is an important source of forcing that excites Pacific MM variability, it is natural to expect that the internal atmospheric variability can exert an influence on ENSO via its effect on the MM. This chapter further explores the role of atmospheric internal variability in maintaining the MM variability, and consequently ENSO. To fulfill this objective, we adopt a novel approach; we filter out internal atmospheric variability in the coupled model, so that we can further quantify its effect on ENSO.

We are assuming that the atmospheric variability can be divided into two parts: an internal part due to intrinsic atmospheric dynamics, independent of anomalous SST forcing (hereafter referred to as the "noise"), and an external part due to imposed boundary condition (SST anomalies) forcing (hereafter referred to as the "signal"). One major difficulty in using a CGCM for the study of the stochastic ENSO mechanism is how to isolate the "signal" part from the "noise" reliably so that the coupled feedback can be extracted and examined separately. It is challenging because 1) the "signal" and "noise" are integral parts of the atmospheric variability and 2) the forced response is often weak compared to the internal atmospheric variability allowing the "signal" to be easily contaminated by the noise (Chang et al., 2000). Until very recently, the available coupled GCMs do not have the ability to discriminate between the signal and the noise.

The traditional technique is to use an ensemble average of many atmospheric realizations, subject to the same boundary forcing, to isolate the forced signal from the "noise". In this approach, an ensemble of AGCM runs with slightly different initial conditions, forced for example with observed SST, is first performed, and then a first order estimate of the signal can be obtained by taking an ensemble average of these runs. The noise can be defined as the departure from the ensemble mean. This simple technique works well provided that the ensemble size is sufficiently large. A practical limitation of this method is that for a finite size ensemble, the ensemble mean provides a biased estimate of the signal. This noise contamination problem can be severe if the ensemble size is small.

Based on this idea, Kirtman and Shukla (2002) proposed to use an interactive coupled ensemble strategy within a CGCM to separate signal from noise fields. This procedure uses multiple realizations of the atmospheric GCM at each couple time step coupled to a single realization of the ocean model. Each atmospheric realization differs in their initial conditions but experiences the same SST forcing provided by the same OGCM. The OGCM, on the other hand, experiences surface fluxes that are the ensemble averaged over the AGCM realizations. The ensemble mean of the atmospheric GCM fluxes reduces the atmospheric internal variability in the coupled GCM. They show that the results seem to have relatively small sensitivity in terms of sample size of the AGCM realizations in their ENSO simulation, provided the size is larger than six.

Using such a modeling approach, Kirtman et al. (2004) tested the null hypothesis that ENSO resides in a stable dynamical regime and its low-frequency modulation is largely determined by stochastic processes in the atmosphere (Flügel and Chang, 1999), within the framework of a coupled GCM. They found that there are significant regions in the tropical Pacific where the SST variability can not be explained by the

null hypothesis, suggesting that the deterministic dynamics are important. While the study of Kirtman et al. (2004) represents the first of its kind in its use of a coupled GCM to test the null hypothesis, they caution that "these results may be model-dependent". Therefore, further studies in making use of coupled GCMs to study the role of internal atmospheric variability of ENSO are needed.

The study in this chapter deviates from Kirtman et al. (2004) in two ways. First, the scientific objective of this study is not simply to test the null hypothesis, but to examine the role of the MM in linking internal atmospheric variability and ENSO. Second, we employ a noise filtering procedure to extract the coupled signal, instead of using the interactive ensemble approach. The appealing feature of our filtering procedure is that it presents an unbiased estimate of the signal and thus gives a better treatment of signal/noise separation even when ensemble size is relatively small. It is also computationally more efficient because the filter is pre-determined based on AGCM AMIP runs.

This chapter is divided into five sections. Section B discusses the design of the noise filter and tests how effective the filter works. Section C describes the implementation of the noise filter with the coupled system and the noise filtered coupled experiment. Section D further examines the relative importance of dynamic and thermodynamic noise forcing. Section E is the summary and discussion.

B. Design and Testing of the Noise Filter

1. Concept of the Noise Filter

The concept of the noise filter is to find a projection vector (filter) such that the filter projects an individual ensemble member onto a set of signal-to-noise optimals and weights their contribution according to the signal-to-noise ratio. The high signal-

to-noise optimals get higher weights than the lower signal-to-noise ones, so that only the signal portion of variance in each ensemble member passes through the filter. The mathematical formulation of the filter was derived by Tippett and Chang (unpublished manuscript). Its concept was motivated by the signal-to-noise optimization analysis proposed by Allen and Smith (1997), and subsequently used by Venzke et al. (1999) and Chang et al. (2000) to identify dominant SST-forced atmospheric response from a moderate-size ensemble of AMIP runs.

Let $\mathbf{C}_M$ represent the ensemble mean covariance of a state vector $\mathbf{X}_M$ (ensemble mean) from an m-member ensemble of AGCM runs forced with historical SSTs, and $\mathbf{C}_N$ represent the noise (departure from ensemble mean) covariance. The ensemble mean covariance $\mathbf{C}_M$ consists of the covariance of the true signal $\mathbf{C}_S$ and noise contamination $\frac{1}{m}\mathbf{C}_N$, i.e.,

$$\mathbf{C}_M = \mathbf{C}_S + \frac{1}{m}\mathbf{C}_N. \tag{5.1}$$

Assuming the noise and the signal are uncorrelated, the best estimate of the true signal $\mathbf{X}_S$ at a particular time, according to least-squares estimate of the signal, is

$$\mathbf{X}_S = (\mathbf{C}_M - \frac{1}{m}\mathbf{C}_N){\mathbf{C}_M}^{-1}\mathbf{X}_M = (\mathbf{I} - \frac{1}{m}\mathbf{C}_N{\mathbf{C}_M}^{-1})\mathbf{X}_M. \tag{5.2}$$

This is a regression between the ensemble mean and the signal. As $m \to \infty$, $\mathbf{X}_S \to \mathbf{X}_M$, i.e., the ensemble mean is the true signal for a sufficiently large ensemble.

This signal estimate $\mathbf{X}_S$ minimizes the cost function

$$\mathsf{J}(\mathbf{X}_S) = m(\mathbf{X}_S - \mathbf{X}_M)^T{\mathbf{C}_N}^{-1}(\mathbf{X}_S - \mathbf{X}_M) + {\mathbf{X}_S}^T(\mathbf{C}_M - \frac{1}{m}\mathbf{C}_N)^{-1}\mathbf{X}_S. \tag{5.3}$$

The signal estimate projects mostly onto the signal covariance and its difference with the ensemble mean projects mostly onto the noise. As $m \to \infty$ the first term of the cost function dominates, requiring that $\mathbf{X}_S \to \mathbf{X}_M$.

The relation in the (5.2) is closely related to the generalized eigenvalue problem $\mathbf{C}_M\mathbf{F} = \mathbf{C}_N\mathbf{F}\lambda$, where $\mathbf{F}$ is the matrix of filter patterns and λ is the corresponding eigenvalues which define the signal-to-noise ratio. The eigenvectors , ordered by their eigenvalues from largest to smallest, are such that the leading eigenvector gives the projection vector $\mathbf{F}$ that maximizes the signal-to-noise ratio over all possible patterns, the second eigenvector maximizes the signal-to-noise ratio over all patterns unrelated to the leading pattern, and so on.

Suppose that the noise covariance $\mathbf{C}_N$ is singular with j nonzero eigenvalues and has the "economy" eigenvalue decomposition $\mathbf{C}_N = \mathbf{E}_N\lambda_N\mathbf{E}_N^T$, where the eigenvalue matrix λ_N is $\mathsf{j} \times \mathsf{j}$ and matrix $\mathbf{E}_N$ (noise EOFs) of eigenvectors is $\mathsf{n} \times \mathsf{j}$; n is the dimension of the full-space. Then the generalized eigenvalue problem can be written

$$\mathbf{C}_M\mathbf{F} = \mathbf{E}_N\lambda_N\mathbf{E}_N^T\mathbf{F}\lambda. \tag{5.4}$$

Define the $\mathsf{j} \times \mathsf{j}$ projection $\hat{\mathbf{C}}_M$ of the ensemble mean covariance on the noise EOFs by $\hat{\mathbf{C}}_M = \mathbf{E}_N^T\mathbf{C}_M\mathbf{E}_N$ and the $\mathsf{j} \times \mathsf{j}$ projected filter pattern $\hat{\mathbf{F}}$ by $\hat{\mathbf{F}} = \mathbf{E}_N^T\mathbf{F}$, in which $\mathbf{F}$ is assumed to be an $\mathsf{n} \times \mathsf{j}$ matrix and lies in the space spanned by the columns of $\mathbf{E}_N$; then (5.3) can be written $\hat{\mathbf{C}}_M\hat{\mathbf{F}} = \lambda_N\hat{\mathbf{F}}\lambda$, and be re-arranged as $\hat{\mathbf{C}'}_M\mathbf{G} = \mathbf{G}\lambda$, where the whitened projected ensemble mean covariance is $\hat{\mathbf{C}'}_M = \lambda_N^{-\frac{1}{2}}\hat{\mathbf{C}}_M\lambda_N^{-\frac{1}{2}}$ and the whitened projected ensemble mean EOFs are $\mathbf{G} = \lambda_N^{\frac{1}{2}}\mathbf{F}$.

Standard methods are used to find $\mathbf{G}$ and λ, such that $\hat{\mathbf{C}'}_M = \mathbf{G}\lambda\mathbf{G}^T$; $\mathbf{G}$ is a $\mathsf{j} \times \mathsf{j}$ orthogonal matrix. Solve for $\hat{\mathbf{F}} = \lambda_N^{-\frac{1}{2}}\mathbf{G}$. Define the projected physical pattern $\hat{\mathbf{P}} = \lambda_N^{\frac{1}{2}}\mathbf{G}$ so that $\hat{\mathbf{P}}\hat{\mathbf{P}^T} = \lambda_N$,$\hat{\mathbf{P}}\hat{\mathbf{F}^T} = \mathbf{I}$ and $\hat{\mathbf{P}}\lambda\hat{\mathbf{P}^T} = \hat{\mathbf{C}}_M$. Therefore,

$$\lambda_N\hat{\mathbf{C}}_M^{-1} = \hat{\mathbf{P}}\lambda^{-1}\hat{\mathbf{F}}^T. \tag{5.5}$$

Define

$$\begin{aligned}\hat{\mathbf{X}}_S &= (\hat{\mathbf{C}}_M - \frac{1}{m}\lambda_N)\hat{\mathbf{C}^{-1}}_M\hat{\mathbf{X}}_M \\ &= (\mathbf{I}_j - \frac{1}{m}\lambda_N\hat{\mathbf{C}}_M^{-1})\hat{\mathbf{X}}_M \\ &= \hat{\mathbf{P}}(\mathbf{I}_j - \frac{\lambda^{-1}}{m})\hat{\mathbf{F}}^T\hat{\mathbf{X}}_M.\end{aligned} \tag{5.6}$$

The quantity $\hat{\mathbf{X}}_S$ minimizes the cost function

$$\mathsf{J}(\hat{\mathbf{X}}_S) = m(\hat{\mathbf{X}}_S - \hat{\mathbf{X}}_M)^T{\lambda_N}^{-1}(\hat{\mathbf{X}}_S - \hat{\mathbf{X}}_M) + \hat{\mathbf{X}}_S^T(\hat{\mathbf{C}}_M - \frac{1}{m}\lambda_N)^{-1}\hat{\mathbf{X}}_S. \tag{5.7}$$

Therefore, $\hat{\mathbf{P}}(\mathbf{I}_j - \lambda^{-1})\hat{\mathbf{F}}^T$ is the sought-after noise filter. For example, the signal estimate of an individual ensemble member , say $\mathbf{X}_1$, can be obtained from (5.6) by setting $m = 1$, i.e.,

$$\mathbf{X}_{S1} = \hat{\mathbf{P}}(\mathbf{I}_j - \lambda^{-1})\hat{\mathbf{F}}^T\mathbf{X}_1. \tag{5.8}$$

In summary, the noise filtering procedure consists of three steps: 1) Solving for the eigenvalues (λ_N)/eigenvectors ($\mathbf{E}_N$) of the noise covariance matrix to obtain the noise EOFs; 2) Solving for the eigenvalues/eigenvectors of the whitened ensemble mean covariance matrix to obtain signal-to-noise optimals in the truncated state space of noise EOFs; 3) Using the signal-to-noise optimals to construct the filter. Once constructed, the signal estimate can be obtained by projecting an individual ensemble member onto the filter.

There are two EOF truncations made in the process: The first is determining how many of the noise EOFs that one needs to keep when solving the signal-to-noise optimals and the other is determining how many signal-to noise optimals one needs to keep when constructing the filter. We tested the sensitivity of the noise filter to truncation variations in a certain range of EOF modes, and took the patterns that are robust with respect to the truncations. It should be pointed out that the filter

is independent of time, so this noise filtering procedure does not apply to the time domain.

2. Test Noise Filter

The noise filter allows the removal of the noise when applied to an individual ensemble member of the AMIP runs. Therefore, once derived, it provides a good estimate of the SST forced response from a single realization of the AGCM. As an example to illustrate the effectiveness of the filter, an ensemble of ten CCM3 integrations, forced with monthly averaged observed SSTs (Smith et al., 1996) in the global ocean from January 1950 to December 1994, were used to construct an annual mean noise filter using the EOFs of the noise covariance of the zonal wind stress derived from these 45-year integrations. We then applied the filter to the zonal wind stress anomaly from an arbitrary ensemble member of the CCM3 runs.

Fig. 42 shows the leading EOF of the zonal wind stress in the tropical Pacific and the associated time series of the leading EOFs for the "signal" derived from the 10-member ensemble(top panel) using the technique of Allen and Smith (1997), and for one individual ensemble member (middle panel). The individual ensemble member hardly captures any structure in the tropics and the spatial pattern of the north Pacific is clearly dominant, compared with the signal pattern. The bottom panel of Fig. 42 depicts the same calculation of the signal estimate of the same individual ensemble member using the noise filter. It is clear that the leading EOF over the tropical Pacific basin exhibits a spatial pattern that is virtually identical to that of the "signal". The correlation of the time series associated with the first EOFs between the signal estimate (a) and the noise filtered estimate (c) is 0.71, while the correlation between the signal estimate and the individual ensemble member (b) is only 0.28. This suggests that the noise filter is capable of extracting the forced signal

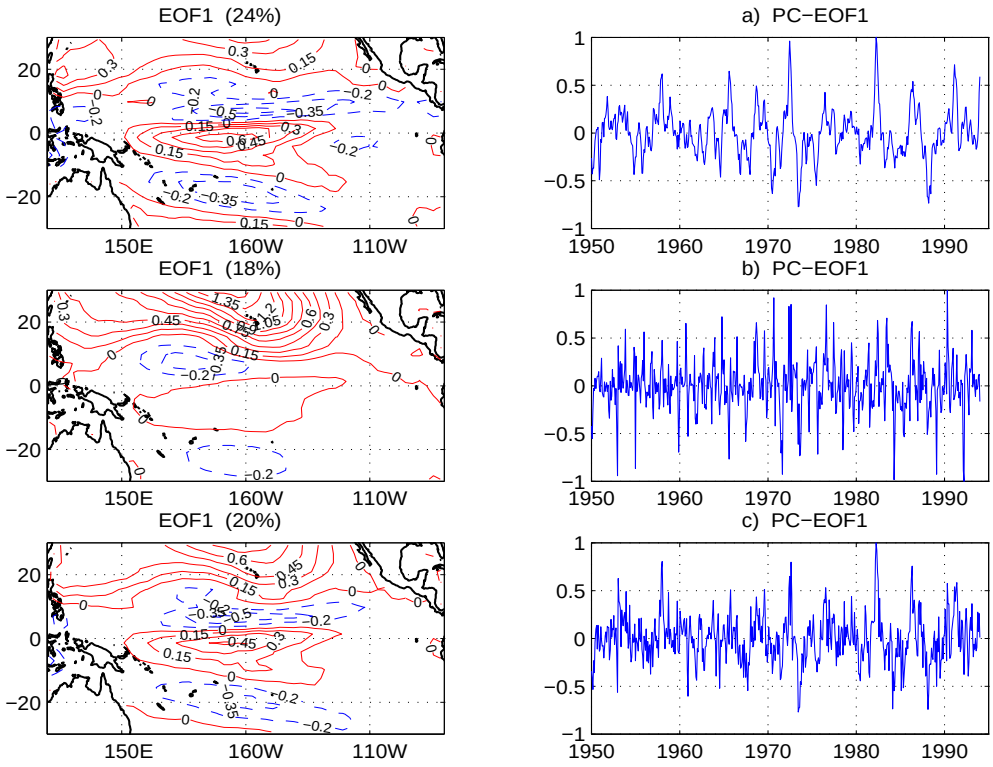

Fig. 42. Spatial and temporal patterns of the leading EOF of zonal wind stress in the tropical Pacific for the "signal" derived from a 10-member ensemble mean(top panel), for one individual ensemble member (middle panel) and for the signal estimate of the same individual ensemble member (bottom panel).

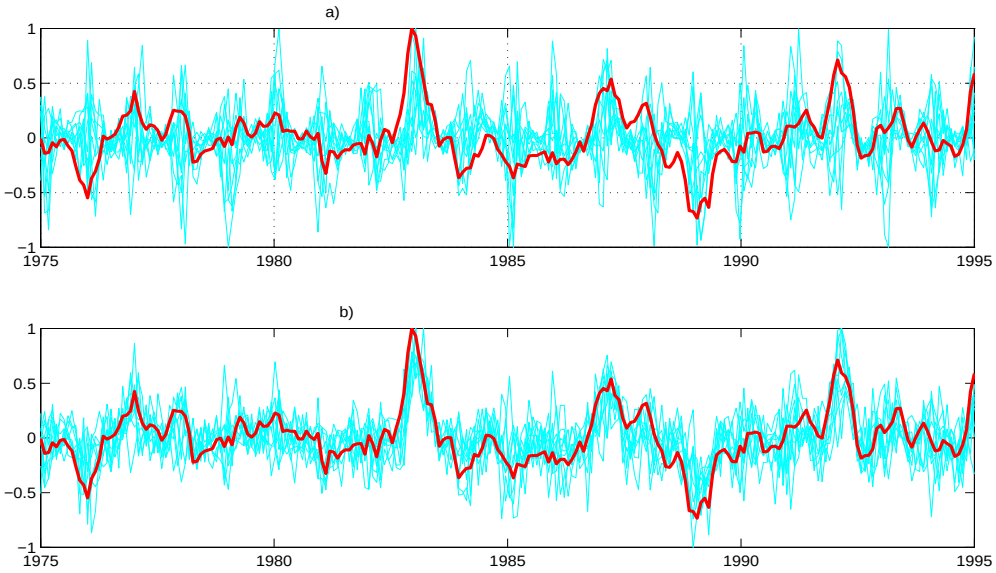

Fig. 43. The time series of the first EOFs of zonal wind stress for the 10 individual ensemble members (cyan lines in upper panel) and the corresponding noise filtered ones (cyan lines in lower panel), and the signal estimate (red line in both panels).

from the individual ensemble member.

To illustrate this point further, we show in Fig. 43 the time series associated with the leading EOFs of zonal wind stress for the 10 individual ensemble members (cyan lines in upper panel) and the corresponding noise filtered ones (cyan lines in lower panel), and the signal estimate (red line in both panels). It is evident that the 10 noise filtered signals generally agree much better with the the signal estimate than the unfiltered ones; there is a considerable spread among 10 unfiltered individual ensemble members (from 0.01 to 0.30). Careful readers may notice that the time series associated with the first EOFs of 10 individual ensemble members show weak seasonal cycle, which may indicate that the filter would work even better if we take seasonal variation into consideration.

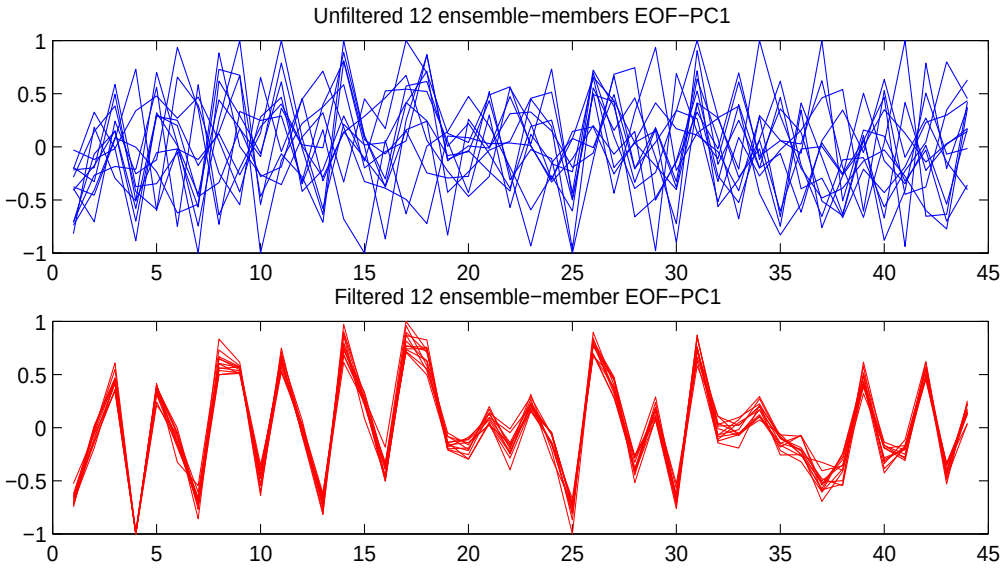

Fig. 44. The time series associated with the first EOFs of zonal wind stress for January before (top) and after (bottom) applying the noise filter.

To be more consistent with the CCM3-RGO model that is used for this study, the actual construction of the noise filter was based on an ensemble of twelve 45-year CCM3 integrations forced with a 45-year SST taken from the 400-year control simulation of the CCM3-RGO. To take into consideration of strong seasonal dependence, twelve filters, one for each of the calendar months, were constructed for each of the coupled variables, including wind stress (τ_x, τ_y) and surface heat flux.

Fig. 44 displays the time series associated with the first EOFs of the zonal wind stress for January before (top panel) and after (bottom panel) applying the noise filter. It is obvious that unfiltered members show a considerable spread and are barely correlated among each other. But the filtered members are strongly correlated among each other with average correlation value of 0.997.

In terms of the total "noise" variance that is removed by the filter, Fig. 45 compares the variance maps of the January zonal wind stress anomalies of one unfiltered

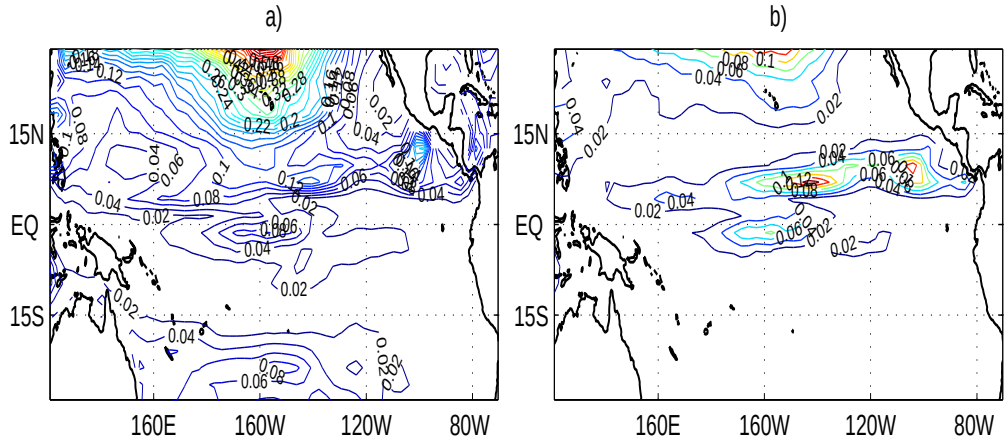

Fig. 45. Variance maps of the January zonal wind stress anomalies of one unfiltered (a) and filtered (b) individual ensemble member.

(Fig. 45a) and filtered (Fig. 45b) individual ensemble member. It clearly shows that much of the variance in the extratropics is reduced dramatically in the unfiltered case while within the tropical region most of the variance is retained. This is expected because the tropical atmosphere is much more sensitive to SST forcing than extratropics. Therefore, we would expect behavior of the control run to be different from the coupled experiments with filtered surface wind stress and heat flux.

C. Coupled Experiments With Noise Filter

As demonstrated in the previous section, the noise filter is effective in suppressing internal atmosphere variability, and is easily applied to the coupled CCM3-RGO model. Recall that four atmospheric variables (zonal and meridional wind stress, net heat flux and solar radiation) are passed to the ocean at each coupling step (once a day). The noise filter was implemented by simply applying the filter to all four variables at each coupling step (every day), and then combine these filtered fields

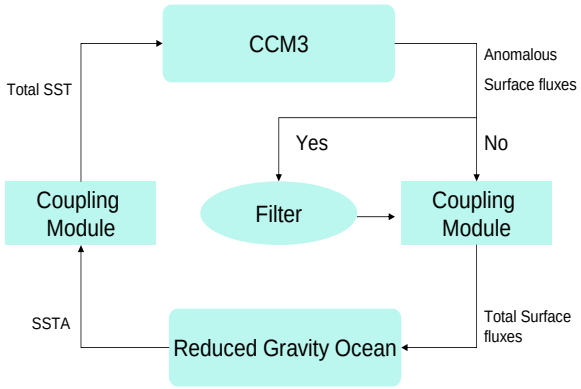

Fig. 46. Flowchart of CCM3-RGO model with (Yes) and without (No) noise filter.

with the corresponding observed climatology before passing them onto the ocean model. The way that the SST anomaly was passed to the atmosphere model remained unchanged. In so doing, the noise filter acts to reduce the effect of the internal atmospheric variability on the ocean-atmosphere coupling. The flowchart (Fig. 46) summarizes how the noise filter was applied to the coupled model.

A 200-year coupled simulation was conducted where the noise filter was applied to all coupled variables. Hereafter, we refer to this experiment as the fully-filtered run. The following discussion is devoted to the comparison between the first 100-year CCM3-RGO control run and the 100-year fully-filtered run.

1. ENSO Variance

The first issue to be addressed concerns with the role of atmospheric internal variability in maintaining ENSO variance.

For this, we compare the SST anomaly variance in the tropical Pacific region from the two experiments as shown in Fig. 47 . There is a major reduction in SST variance of the fully-filtered experiment in comparison with the control run. Furthermore, the

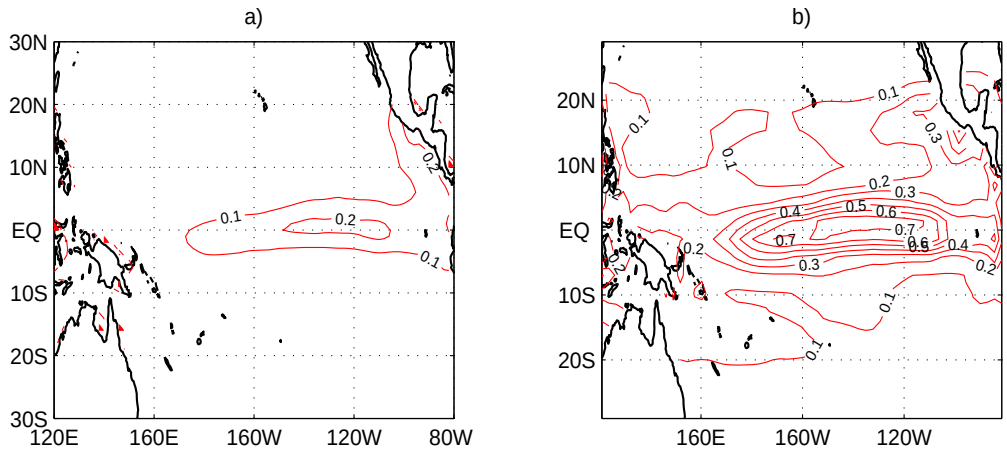

Fig. 47. SST anomaly variance in the tropical Pacific region from the fully-filtered run (a) and from the CCM3-RGO control run (b).

structure of SST variance in the Pacific becomes narrower and more confined to the equatorial zone in the fully-filtered run than in the control run.

This reduction in SST variance can be further seen in Fig. 48, where the time series, power spectra and auto-correlation of the NINO3 index are displayed for the first 100-year control run and the 100-year fully-filtered run. When the filter is applied, the peak-to-peak variation of the NINO3 index falls within one standard deviation of the control run (dashed line in Fig. 48a and b), though its periodicity does not change substantially (in Fig. 48c and d). Another interesting difference between the two runs is that the NINO3 SST index in the fully-filtered experiment (blue) shows a more regular oscillation than in the control run (red). This suggests that the ENSO in the coupled model may reside in a self-sustained oscillatory regime, and the role of the internal atmospheric variability is to enhance the variance of the ENSO and make it irregular.

Perhaps the most striking difference between the two runs lies in the change

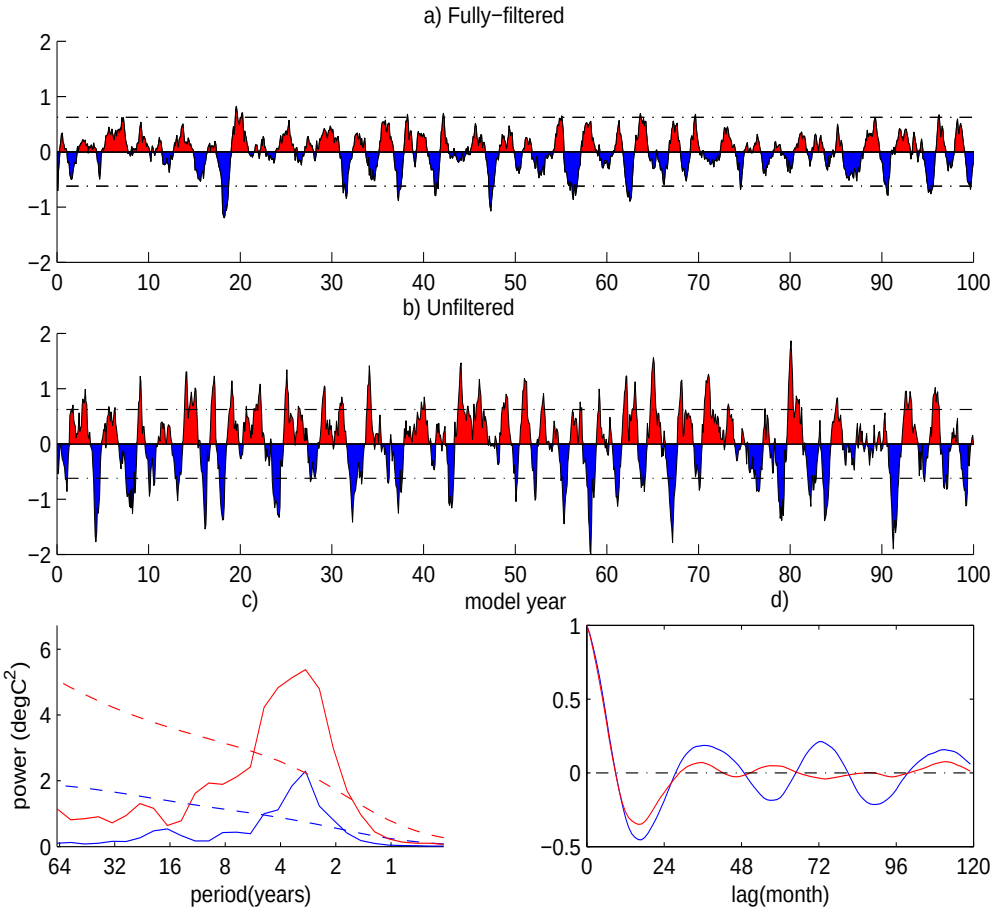

Fig. 48. The time series of the NINO3 index for the 100-year fully-filtered run (a) and for the first 100-year control run (b); Power spectra (c) and auto-correlation(d) of the NINO3 index for the control run (red line) and the fully-filtered run (blue line).

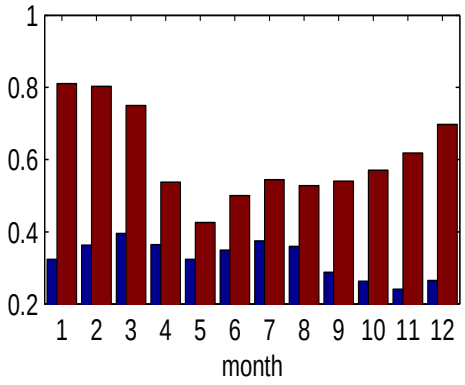

Fig. 49. Standard deviation of the NINO3 SST anomalies as a function of calendar month, for the first 100-year control run (dark red) and for the 100-year fully-filtered run (dark blue).

in seasonal phase-locking of ENSO. Fig. 49 compares the standard deviation of the NINO3 SST anomalies in the two cases as a function of calendar month. As can been seen, the seasonal phase-locking is substantially altered in the absence of internal atmospheric variability. The ENSO cycle is no longer phase-locked to the boreal winter. Instead, the filtered ENSO cycle does not show any strong seasonal preference. This suggests that atmospheric internal variability has a dramatic effect on the seasonal phase-locking of ENSO.

Fig. 50 illustrates the El Niño evolution in the fully-filtered (left panel) and unfiltered (right panel) experiments. Since the ENSO in the filtered experiment is no longer phase-locked to the annual cycle, a composite of the events was made by simply lining up the maximum value amplitude of each identified El Niño event, instead of using calendar months for the control run. However, the same criterion is being used as in the control run to identify El Niño events: the SST anomalies averaged over the NINO3 region exceed one standard deviation for at least three consecutive months. Over the 100-year record of the fully-filtered tun, there are a total number of 22 El

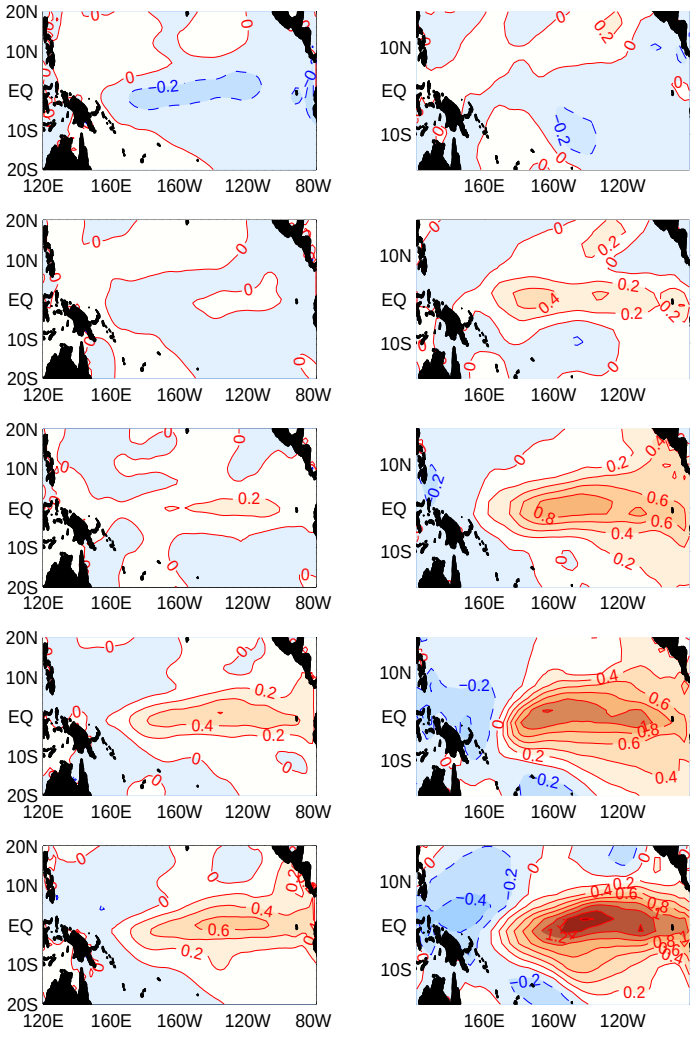

Fig. 50. El Niño evolution in the fully-filtered (left panel): from top to bottom are averaged -12 to -10 month, -9 to -7 month, -6 to -4 month, -3 to -1 month and 0 to 2 month, which corresponds to DJF^0, MAM^0, JJA^0, SON^0 and DJF^{+1} in the control simulation. This evolution behaves very similar to the ENSO-ONLY in the control simulation (shown in the right panel).

Niño events. The warm SST anomalies develop in the west-central Pacific 9 months before the peak of the event which corresponds to MAM^0 in the control run. Overall the canonical evolution of the El Niños in this case behaves very similar to the ENSO-ONLY El Niños in the control simulation that are independent of the MM (shown in the right panel). This implies that after filtering internal atmospheric variability, the number of El Niño events preceded by MM drops significantly so that the canonical El Niño behaves like the ENSO-ONLY events in the control simulation.

2. Meridional Mode and Its Relationship to ENSO

Does the Pacific meridional mode still exist in this filtered experiment? If the MM is a coupled mode, it should remain, but its variance should be reduced substantially as internal atmospheric variability acts as a major source of external forcing for the MM. To test this idea, we used a SVD analysis similar to that used in the previous chapter to identify the MM in the filtered run. Since ENSO in this run does not show a strong seasonal preference, it is difficult to use the approach based on non-ENSO spring data. Therefore, we used the approach of (Chiang and Vimont, 2004) where the SVD analysis is performed on the monthly residual data after linearly removing the ENSO signal. As pointed out previously, the two approaches yield similar findings. To directly compare with the results from the control simulation, the same SVD analysis is also applied to the first 100-year of the 400-year monthly data of the control run. Fig. 51 illustrates the spatial pattern of the leading SVD, along with the seasonal dependence of the corresponding wind stress expansion coefficient and the lag-correlation between the wind stress expansion coefficient and SST expansion coefficient, respectively, for the filtered experiment (upper panel) and the control run (lower panel). The MM's temporal characteristics in the two experiments are very similar with maximum variance in FMAM; and the highest correlation between

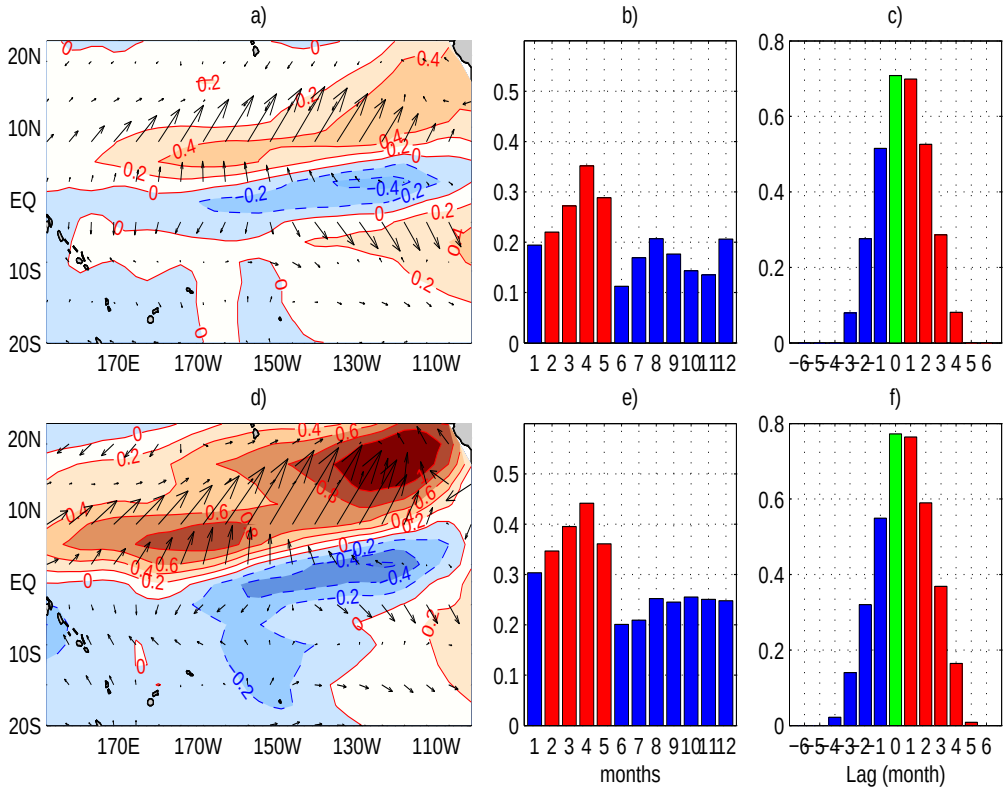

Fig. 51. Spatial (a,d) and temporal properties of the leading SVD mode between the residual wind stress and residual SST anomaly for the fully-filtered run (top panel) and for the 100-year control run (bottom panel), after linearly removing the ENSO signal. The seasonal dependence of the wind expansion coefficient in b and e. Lag-correlationship between the wind expansion coefficient and the SST expansion coefficient in c and f. Positive lag month signifies that the wind expansion coefficient leads.

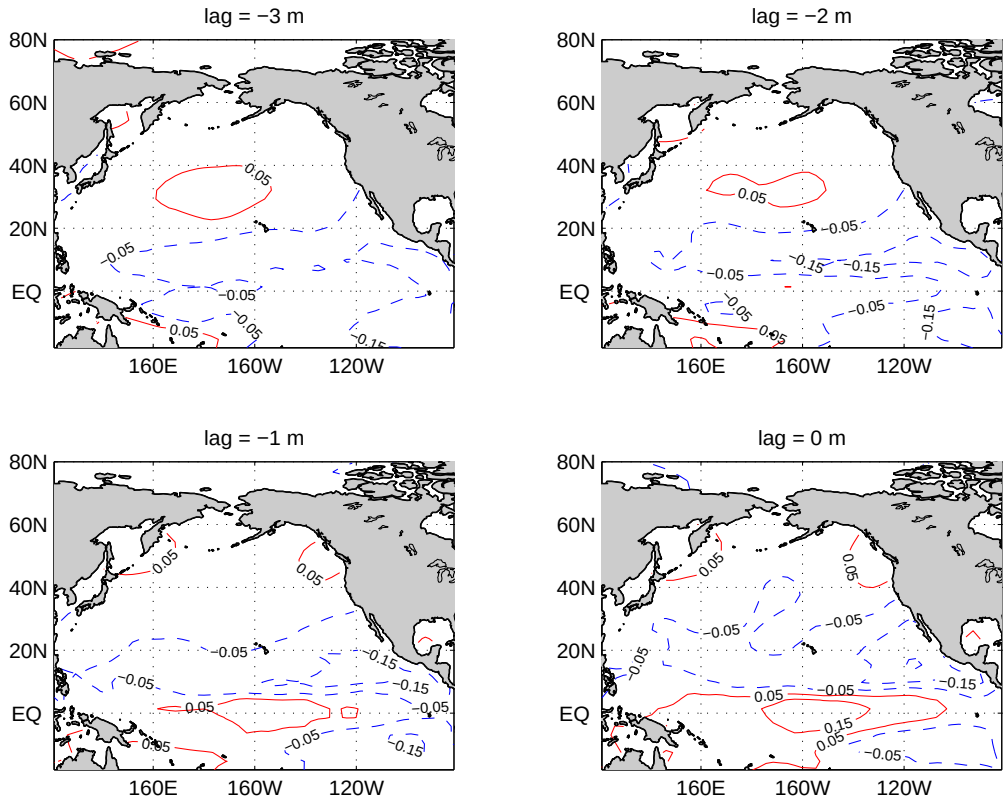

Fig. 52. Lag correlation between the monthly SLP anomaly and the SST expansion coefficient in fully-filtered run at different lags, with SLP leading the SST expansion coefficient by 3, 2, 1 and 0 months.

the two expansion coefficients occurs at zero lag. There is, however, a substantial reduction (about 30%) in amplitude of the MM of the filtered run, particularly during later winter and early spring (JFMA).

The spatial patterns of the MM from both experiments also share some similarities, but again the MM in the filtered case is much weaker than in the control case. The associated positive SST anomaly north of the mean ITCZ is much weakened and narrower in the filtered run than in the control run. Consequently, the gradient between the positive and negative SST anomaly gets weaker, so does the corresponding

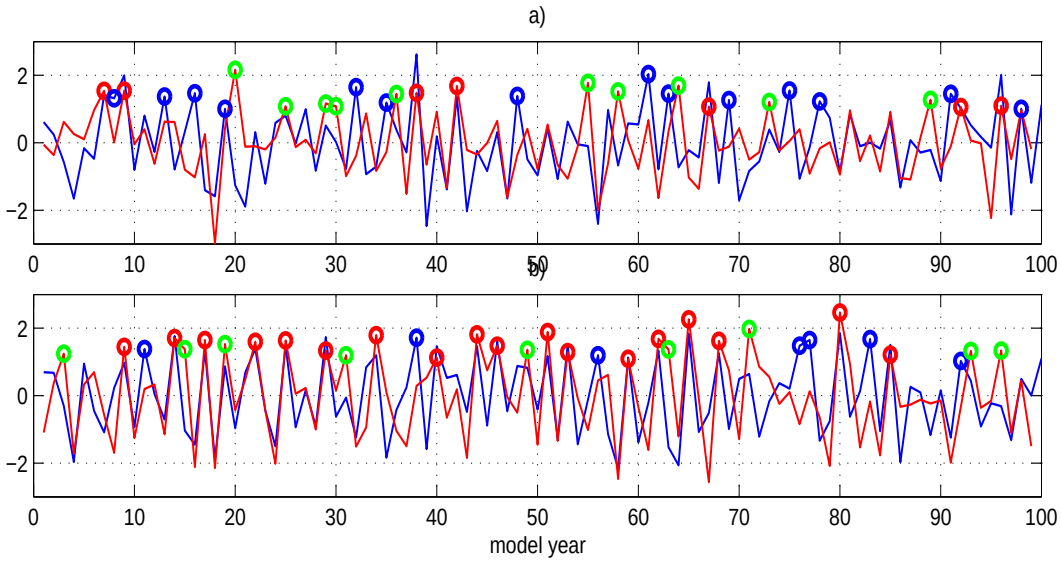

Fig. 53. Normalized FMAM wind expansion coefficient (blue line) and normalized DJF NINO3 index (red line) from the fully-filtered run (upper panel) and the control run (lower panel). Red dots indicate MM-ENSO, green dots indicate ENSO-ONLY, and blue dots indicate MM-ONLY.

wind stress anomaly associated with this MM. Though weakened, this result does suggest that the MM can exist in the absence of or with very little influence from internal atmospheric variability. To reconfirm this claim, we correlated the the SST expansion coefficient associated with the MM in the fully-filtered run to the SLP anomaly at different lags (Fig. 52) and found no significant correlation (correlation less than 0.15), which is in sharp contrast to the control case. This further supports the idea that the meridional mode is indeed a coupled mode and atmospheric internal variability plays a major role in exciting it and enhancing its variability.

What about the relationship between the MM and El Niño events when atmospheric internal variability is suppressed? To answer this question, the FMAM wind expansion coefficient (blue) and DJF NINO3 index (red) are plotted against each

other in Fig. 53 for both the fully-filtered (upper) and unfiltered (lower) runs. Each time series has been normalized by its own standard deviation. The correlation between these two is 0.36 for the filtered case, which is substantially lower than the value of the control run (0.56). Using the same criterion as for the control run to classify all the El Niño and MM events in the filtered run, we found that 33% of the El Niño events (7 out of 21), indicated as red dots, are led by MM events; 67% of the El Niño events (14 out of 21), indicated as green dots, are independent of MM events and 59% of the MMs events (10 out of 17) do not lead to ENSO, denoted as blue dots. In comparison, the population of the El Niños and MMs in each of these categories based on the first 100-year of the control simulation are: 73% of the El Niños events (19 out of 26) are tied to the MMs; 27% of the El Niños events (7 out of 26) are independent of the MMs and 30% of the MMs events (8 out of 27) do not lead to ENSO. Therefore, there is a significant difference in population distribution among the three groups of El Niño and MM events in the two experiments. The population in MM-ENSO drops dramatically in the filtered case, compared with the control run, while the populations in ENSO-ONLY and MM-ONLY increase markedly. There is also a decrease in the total number of the MM events and El Niño events in the filtered run.

So what do these statistics tell us? They confirm that atmospheric internal variability does play an important role in determining the strength and occurrence of the MM events, consequently having an impact on the relationship between the MM and ENSO. When atmospheric internal variability is present, the MM events are strong and frequent. Therefore, the MMs are very effective in affecting ENSO and the correlation between the two is high. One sees that the majority of ENSO events follow a MM event. On the other hand, when atmospheric internal variability is suppressed, the MM variability is weakened, making it more difficult to affect

ENSO. Therefore, the correlation between the two is relatively low. A majority of ENSO events become independent of the MMs, which results in an increase in the population of ENSO-ONLY. As a result of this change, the seasonal phase-locking of ENSO is altered.

D. Relative Importance of Dynamic and Thermodynamic Noise Forcing

Internal atmospheric variability can affect coupled feedbacks in the tropics via its impact on surface wind stress and/or surface heat flux exchanges. But which of these exchanges is more important in terms of affecting ENSO?

To address this question, two additional filtered experiments are carried out: 1) Only surface heat flux is filtered, so that only the signal of the surface heat flux is passed to the ocean during the coupling. The result of this experiment will tell us the extent to which internal atmospheric variability in wind stress only can affect ENSO; 2) Only wind stress is filtered, so that only the signal of the wind stress is passed to the ocean during the coupling. The result of this experiment will shed light on to the extent to which internal atmospheric variability in the heat flux can influence ENSO. Like the other filtered experiment, each of these experiments has 100-year integration. Hereafter, we will refer to these experiments as the filtered-flux and filtered-wind experiments.

1. ENSO Variance

The variance of the SST anomaly from the filtered-flux experiment in the Pacific region is shown in Fig. 54a and the variance from the filtered-wind experiment is shown in Fig. 54b. For the filtered-flux experiment, the SST variance outside the deep tropics is reduced markedly, while the reduction within the deep tropics is small. For

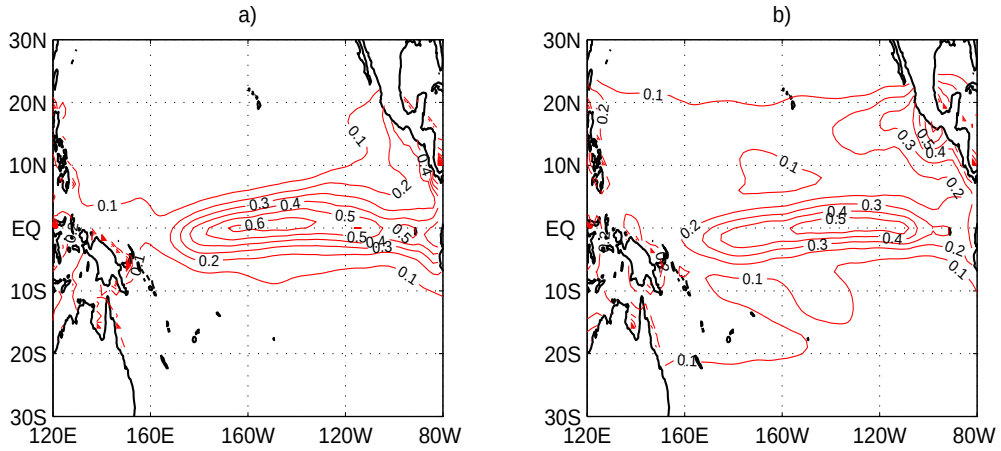

Fig. 54. SST anomaly variance in the tropical Pacific region from the filtered-flux run (a) and from the filtered-wind run (b).

the filtered-wind experiment, the reduction in the deep tropics is more severe than that outside of the tropics and the overall structure remains more similar to that of the control run (Fig. 47b). This suggests that filtering the noise in the surface heat flux has a stronger impact on the SST variance in the extratropics, while filtering the noise in the wind stress has a stronger impact on the SST variance in the deep tropics. This is consistent with the ENSO dynamics: the SST variability within the deep tropics is more controlled by the ocean dynamics which is closely related to wind stress fluctuations. Outside the deep tropics, the SST changes are controlled more by mixed layer dynamics which is predominantly driven by surface heat flux.

Let us now take a further look at the model ENSO variability in each of these experiments. Fig. 55 and Fig. 56 show the time series, power spectra and phase-locking of the NINO3 index for the filtered-flux and the filtered-wind experiment, respectively. A marked change is observed for the phase-locking of ENSO which in this case shows no seasonal preference, as in the fully-filtered run (Fig. 47). Another

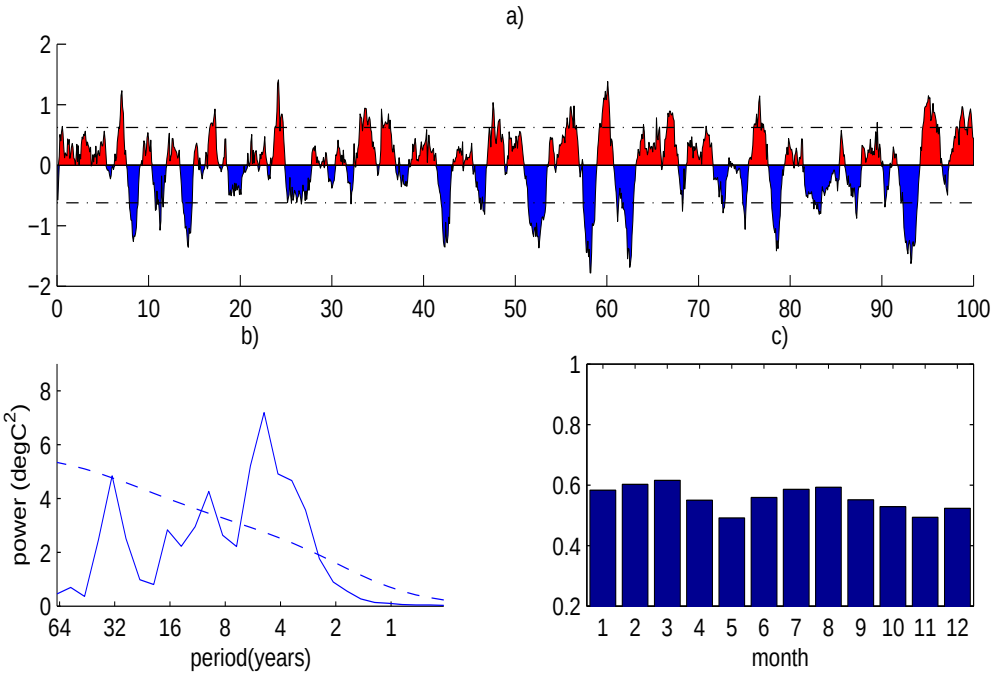

Fig. 55. The time series (a), power spectra (b) and seasonal dependence of standard deviation (c) of the NINO3 index for the filtered-flux run.

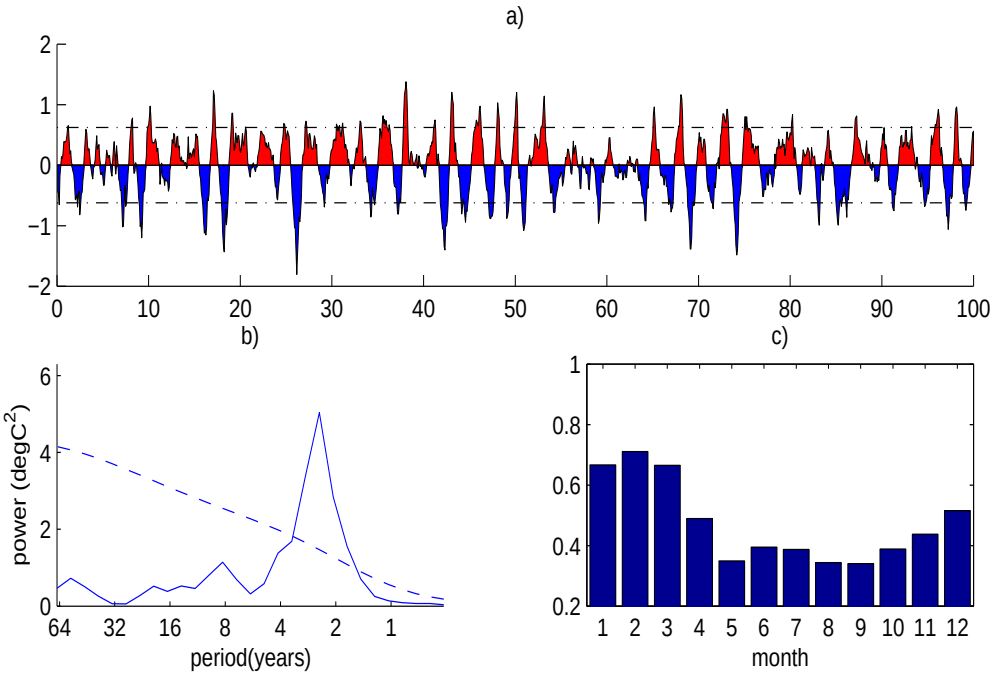

Fig. 56. The time series (a), power spectra (b) and seasonal dependence of standard deviation (c) of the NINO3 index for the filtered-wind run.

change is that the period of the ENSO cycle is somewhat longer, around 4-5 years, compared with the control run. In the experiment where only wind stress is filtered, the phase-locking of ENSO does not change substantially (Fig. 56c), compared to the control run. The ENSO cycle seems to occur more frequently, every 2-3 years, than in the filtered-flux experiment. This tells us that noise in wind stress plays a role in shifting the frequency of ENSO towards the lower frequency end of the spectrum. A comparison of the NINO3 spectra of the two cases also indicates that the noise in the wind stress also tends to broaden the spectral peak while shifting it towards the lower frequency. This effect of noise in the wind stress has been noted previously by Blanke et al. (1997) and others.

2. Meridional Mode and Its Relationship to ENSO

What about the Pacific meridional mode? Similar to the fully-filtered run, SVD analysis was performed to the monthly data of the two filtered experiments after linearly removing ENSO. Fig. 57 depicts the spatial pattern of the first SVD analysis, the seasonal dependence of the corresponding wind expansion coefficient and the lag-correlation between the wind expansion coefficient and SST expansion coefficient, respectively, for the filtered-flux experiment (upper panel) and the filtered-wind experiment (lower panel). The expansion coefficients display similar seasonality and lag-correlation structures, except that the filtered-wind case has a cleaner boreal spring phase-locking and shows higher correlation at longer lags, particularly when SST leads the winds, suggesting a possibly stronger feedback. The spatial patterns also share some similarities, but the MM in the filtered-flux case is clearly weaker than in the filtered-wind case, especially for the positive SST anomaly north of the mean ITCZ region and the associated southwesterly wind anomaly. Overall, the MM in the filtered-wind experiment resembles more closely that of the control run (Fig. 51d),

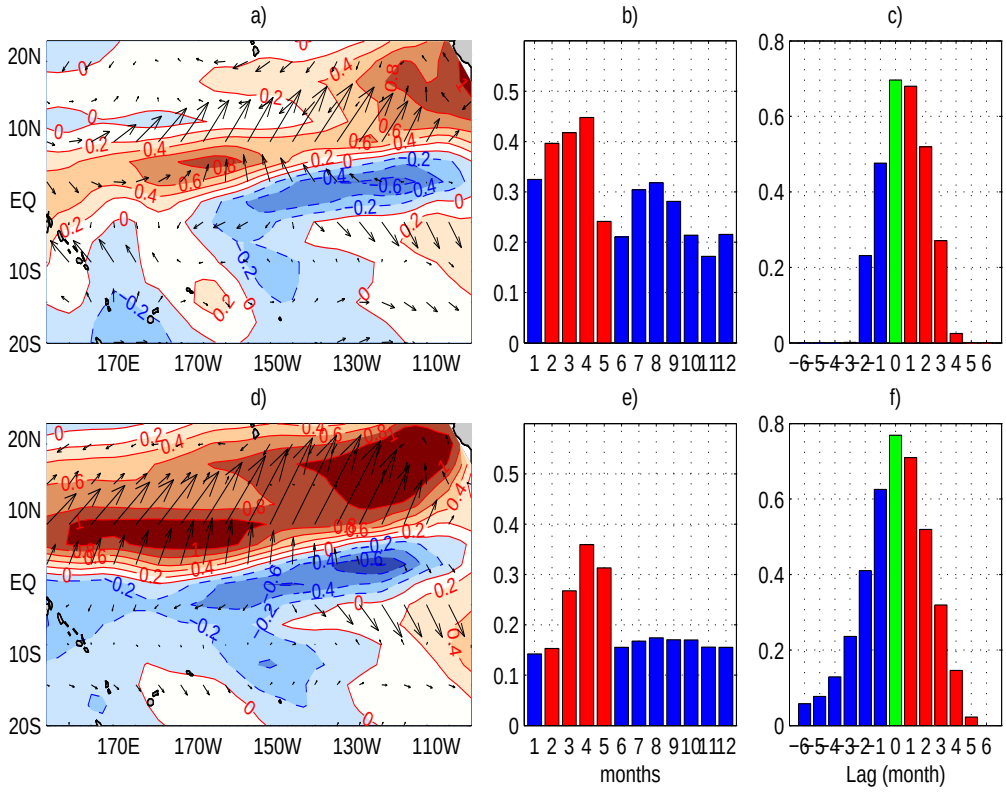

Fig. 57. Spatial (a,d) and temporal properties of the leading SVD mode between the residual wind stress and residual SST anomaly for the filtered-flux run (top panel) and for the filtered-wind run (bottom panel), after linearly removing the ENSO signal. The seasonal dependence of the wind expansion coefficient in b and e. Lag-correlationship between the wind expansion coefficient and the SST expansion coefficient in c and f. Positive lag month signifies that the wind expansion coefficient leads.

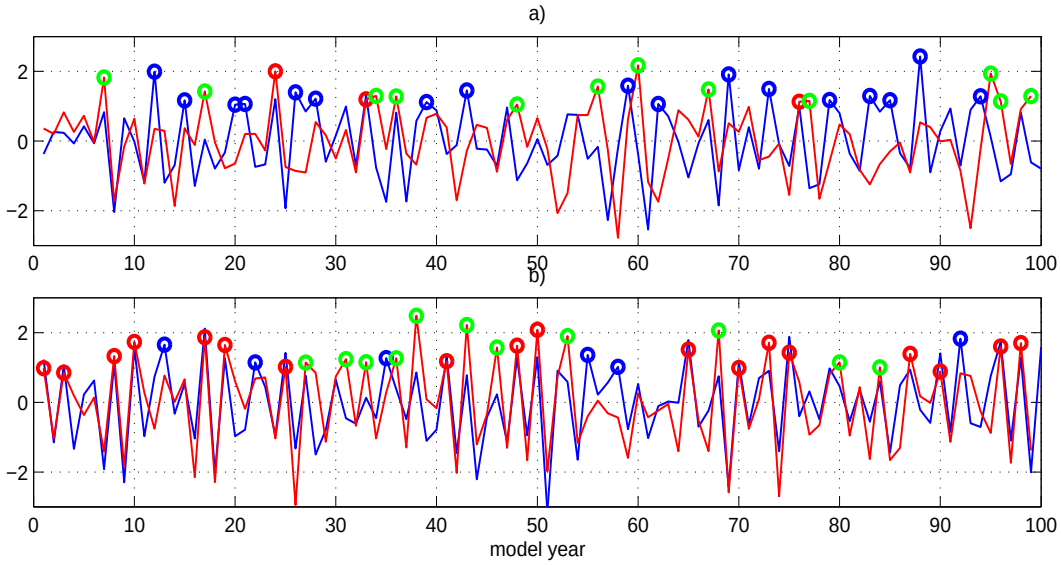

Fig. 58. Normalized FMAM wind expansion coefficient (blue line) and normalized DJF NINO3 index (red line) from filtered-flux run (upper panel) and the filtered-wind run (lower panel). Red dots indicate MM-ENSO, green dots indicate ENSO-ONLY, and blue dots indicate MM-ONLY.

while the one in the filtered-flux run resembles more the fully-filtered run (Fig. 51a). This suggests that it is the noise in heat flux that plays a more important role in maintaining the MM which in turn affects the onset of ENSO.

Consequently, one would expect that the relationship between the MM and El Niño events in the filtered-flux experiment be less tightly correlated than in the filtered-wind experiment. The FMAM wind expansion coefficient (blue) and DJF NINO3 index (red) from the two experiments are plotted in Fig. 58 with the upper panel for filtered-flux experiment and lower panel for filtered-wind experiment. Each time series has been normalized by its own standard deviation. The correlation between the wind expansion coefficient and the NINO3 index is 0.20 and 0.75, respectively, for the filtered-flux experiment and for the filtered-wind experiment. Using the same classification criteria for the control run, we found 20% of El Niños (3 out of 15), indicated as red dots, in the filtered-flux experiment are led by the MMs; 80% of El Niños (12 out of 15), indicated as green dots, are independent of the MMs and 85% of the MMs (17 out of 20) do not lead to ENSO denoted as blue dots. Therefore, majority of El Niño events in the filtered-flux experiment are independent of the MMs.

In the filtered-wind experiment, 62% of El Niños (18 out of 29) are tied to the MMs; 38% of El Niños (11 out of 29) are independent of the MMs and 25% of the MMs (6 out of 24) do not lead to ENSO. Therefore, the populations of the El Niños for MM-ENSO and ENSO-ONLY are very similar to those for the control run, suggesting again that the noise in the wind stress does not have a strong impact on the MM and its relationship to ENSO.

The results of the filtered-flux and the filtered-wind experiments reveal different effects of the noise in the wind stress and heat flux on ENSO. The noise in the wind stress does not have a significant impact on the MM and its relationship to

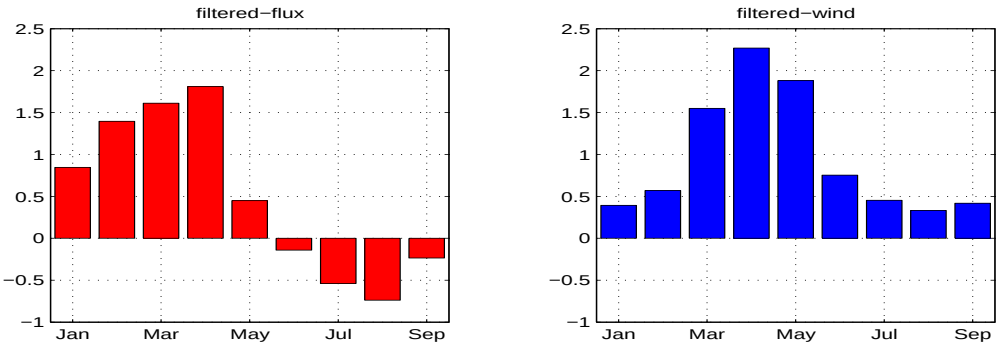

Fig. 59. Composites of the wind expansion coefficient for the filtered-flux run (red) and for the filtered-wind run (blue).

ENSO. Therefore, filtering wind stress noise yields a similar seasonal phase-locking of ENSO. This type of noise, however, does have an influence on ENSO's frequency and regularity; it tends to broaden the spectral peak while shifting it towards lower frequencies. The noise in the heat flux, on the other hand, has a direct impact on the strength of the MM and consequently its ability to influence ENSO. Reducing the effect of heat flux noise yields substantially weakened MM activity and its relationship to ENSO, which leads to altered seasonal phase-locking characteristics.

This finding is further supported by a composite of the wind expansions coefficient of the first SVD analysis for the filtered-flux experiment and for the filtered-wind experiment, shown in Fig. 59, respectively. This is done by averaging all the MM events as a function of calendar month within the years that these events occur in the filtered-flux experiment (red) and the filtered-wind experiment (blue), respectively. The major difference between the two experiments is the persistence of the wind anomaly. In the filtered-wind experiment, the winds appear to persist much longer, from late winter to summer without reversing sign, while the winds in the filtered-flux experiment appear to be short lived, lose strength dramatically and even

reverse sign starting in June. This further demonstrates that the noise in heat flux has a very important role in maintaining the MM, whose persistence is crucial for determining whether a MM event can excite ENSO.

E. Summary and Discussion

In this chapter, we demonstrated the use of a specially designed noise filter to remove internal atmospheric variability in our coupled CCM3-RGO model. We showed that the noise filter can effectively reduce the internal atmospheric variability in the air-sea fluxes and thereby can be used as an effective tool to study the role of internal atmospheric variability in ENSO.

Three experiments each a century in length were conducted: 1) fully filtered run where internal atmosphere variability in both the surface wind stress and heat flux is filtered, 2) filtered-flux run where only internal atmospheric variability in surface heat flux is filtered and 3) filtered-wind run where only internal atmospheric variability in surface wind stress is filtered. These experiments indicate that reducing the effect of internal atmospheric variability or "noise" can alter the characteristics of ENSO in a number of ways, including its regularity, frequency and seasonal phase-locking characteristics. Although different types of noise affects the ENSO in different ways, filtering noise in both wind stress and heat flux (fully filtered run) did not completely suppress the ENSO cycle in the model, suggesting that the model ENSO may reside in the self-sustained regime. The resultant ENSO cycle, however, is substantially weakened, more regular, and no longer shows strong seasonal phase-locking. The latter is perhaps the most provocative discovery of this study, suggesting that ENSO's seasonal phase-locking is tied to the internal atmospheric variability.

This finding is at odds with previous studies that attribute the seasonal phase-

locking to interactions between the tropical annual cycle and ENSO (Jin et al., 1996; Chang et al., 1996; Blanke et al., 1997; Tziperman et al., 1998). In fact, many (Jin et al., 1996; Chang et al., 1996; Blanke et al., 1997) of these studies show that the inclusion of atmospheric noise does not strongly alter ENSO's phase-locking. A more recent study by Roulston and Neelin (2000), while still attributing the seasonal phase-locking to the nonlinear interaction between the ENSO cycle and annual cycle, finds that the phase-locking dynamics are more complex than what is indicated in previous studies and there is considerable variation in ENSO's phase-locking behavior. This variation can be caused by deterministic dynamics due to competition between the inherent ENSO frequency and the tendency to phase-lock to a preferred season and/or stochastic dynamics due to internal atmospheric variability. Therefore, these previous studies indicate that the atmospheric noise has either little or a negative effect on ENSO's phase-locking behavior. What causes the results of this study to be different?

A key dynamic difference between this study and previous studies is that thermodynamic coupling via feedback between surface heat flux and SST which has been either ignored or oversimplified in the previous studies is treated rigorously in this study. The added coupled dynamics allow for the existence of the Pacific MM. The MM's strength is strongly affected by surface heat flux fluctuations induced by boreal winter internal atmospheric variability. The stochastic heat-flux forcing causes stronger MM activities during boreal spring, and thus triggers stronger thermodynamic coupling that makes the events last longer, so that they can play a role in forcing the onset of ENSO. Therefore, it is through the MM that internal atmospheric variability and ENSO are connected. This result is confirmed by the comparison between the fully filtered and filtered-flux experiments.

Our study is consistent with the previous studies in finding that the noise in the surface wind stress has an effect on ENSO irregularity and its frequency, but not so

much on its seasonal phase-locking characteristics. This result is seen clearly in the filtered-wind experiment. In the absence of noise in the winds, the ENSO cycle tends to be more regular and have a shorter period compared to those in the CCM3-RGO control run, but its seasonal phase-locking characteristics remains unchanged. The latter is consistent with the argument that the MM is a thermodynamicly coupled mode and is not directly affected by the noise in surface wind stress. Therefore, the relationship between the MM and ENSO is not changed substantially by suppressing the noise in the wind stress. The result, that the noise in surface wind stress can enhance the irregularity of ENSO, is easily understood and shown in the previous study. However, the result that the noise in surface wind stresses can lead to a longer periodicity of ENSO cycle is not well understood. Blanke et al. (1997) attribute this result to nonlinear effects in the system. Chang et al. (2004) shows that maximum spectral peaks of a linear dynamic system forced stochastically by white noise generally tend to occur at lower frequencies than the frequencies of the leading eigenmode. Which of these two arguments is more effective in explaining the low-frequency shift in the ENSO spectral peak remains to be explored.

One caveat in our noise filtering approach is its implied linearity. Our approach assumes that the noise is additive. Some recent studies have pointed to the multiplicative nature of the noise (Sura and Penland, 2002) and argued that the nonlinear nature of the noise can be a quite important factor for stochastic ENSO theory. The result of Blanke et al. (1997), on the other hand, suggests that accurate treatment of the multiplicative noise is a less burning issue in ENSO study. Also our noise filtering approach is based on ergodic assumption. Some noise may still exist after noise filtering procedure. One way to test our noise filtering approach is to compare it with the interactive ensemble approach of Kirtman and Shukla (2002) and Kirtman et al. (2004), which does not depend on the linearity assumption, but is computationally

more expensive. We plan to carry out a comparison study of these two different approaches in the future.

CHAPTER VI

SUMMARY

A. Major Conclusions

First, the hypothesis that the low-frequency variation of ENSO predictability may be caused by stochastic processes is tested using an ICM. Three "perfect model scenario" prediction experiments are carried out, each of which consists of a large ensemble of predictions. In the first case (reference case), the model is forced solely by stochastic forcing without any explicit decadal-varying background (decade changes in the thermocline depth). In the other two experiments, decadal-varying backgrounds with different amplitudes are introduced into the ICM in addition to the stochastic forcing. By comparing the low-frequency variations of ENSO predictability in these experiments, it is found that only when the amplitude of the decadal-varying background is unrealistically strong, is the effect on ENSO predictability comparable to or larger than the stochastically induced low-frequency ENSO predictability variation. Therefore, to the extent that this simple coupled model system can represent reality, it seems that one can not simply reject the null hypothesis that the decadal variation of ENSO predictability may be stochastically induced.

Second, a new coupled modeling tool consisting of an AGCM (CCM3) and a Zebiak-Cane type of RGO model is developed to test the hypothesis that the Pacific MM is an important precursor of ENSO. This hypothesis is based on two pieces of observational evidence: (1) The MM appears as a dominant mode of variability during the boreal spring when ENSO is absent; and (2) There is a tangible connection between the MM and ENSO: about 70% of the observed ENSOs over the last 40 years are preceded by the MM. To test this hypothesis, we first demonstrate that

this coupled model is able to capture many salient features of the observed ENSO, as well as the MM. We then show, using a 400-year coupled simulation, that: 1) the MM is inherent to thermodynamic ocean-atmosphere coupling, independent of ENSO dynamics, but has a robust relationship to ENSO; 2) roughly 66% of the simulated El Niños are preceded by MM events; 3) the other 34% of simulated El Niños obey the delayed oscillator mechanism, but the surface heat flux anomaly forming in the west-central tropical Pacific may also play a role in initiating these events; and 4) the SST anomaly associated with the MM is most correlated with the southern lobe of the NPO both in the observations and in the model, suggesting that the NPO, induced by internal atmospheric dynamics, may provide one mechanism that excites the MM, and further affects ENSO.

Additional ocean model experiments reconfirm the coupled model result that the MM can lead to the development of ENSO. They further show that the long persistence of the MM is required for it to act as an effective trigger of ENSO. Only for these long persisted events does the associated zonal wind anomaly just north of the equator cause a prolonged deepening of the thermocline and sufficient warming of the SST in the eastern equatorial Pacific that can trigger ENSO events.

Third, a novel noise filter is designed and tested. This filter can effectively reduce internal atmospheric variability. Three coupled experiments, where the filter is utilized to suppress internal atmospheric variability in surface wind stresses and surface heat fluxes simultaneously or separately, yield the following findings : 1) the seasonal phase-locking of ENSO is strongly tied to the internal atmospheric variability, especially in surface heat fluxes; 2) internal atmospheric variability affects ENSO through the MM; when internal atmospheric variability is suppressed, the MM becomes weaker and less effective in triggering ENSO, which in turn results in much weakened ENSO variability; and 3) noise in the surface wind stress can have an effect

on ENSO's frequency and irregularity, but has little effect on ENSO seasonality.

B. Discussion

The existence of the MM and the relationship between the MM and ENSO events, in both observations and model simulation, raise several questions related to previous studies.

How does this work relate to previous studies? The concept of the MM is generally consistent with the optimal initial SST (Penland and Sardeshmukh, 1995) and with the optimal stochastic forcing (Flügel et al., 2004). The MM related meridional SST gradient is similar to optimal initial SST pattern derived by Penland and Sardeshmukh (1995), and the MM related wind stress bears resemblance with optimal stochastic forcing pattern obtained by Flügel et al. (2004). The emphasis of this work is on the underlying physical processes of the MM and its connection to ENSO. The concept of the MM is also generally consistent with the SFP hypothesis (Vimont et al., 2003b), except that the emphasis here is on the connection between the MM and ENSO, but not on the NPO and ENSO. The NPO in this work mainly acts as external forcing to excite the coupled feedback and to allow the MM to strengthen, persist and then excite ENSO. This work also emphasizes the importance of the thermodynamic aspect of ENSO physics, which is less studied and less understood than the dynamic aspect of ENSO physics.

How do these findings differ from the hypothesis of ENSO being triggered by MJO and WWBs? The MM is inherent to thermodynamic coupling, while MJO and WWBs are generally regarded as originating from internal atmospheric dynamics; The MM works as a conduit for extratropical influence on ENSO, whereas MJO and WWBs are normally considered as tropical phenomenon; The MM is a large

scale phenomenon and has a long de-correlation time scale, therefore it may be more predictable in view of its long persistence, while WWBs are short-lived and considered to be a high-frequent atmospheric transient. MJO and WWBs are of different spatial and temporal scales than the MM. We stress that our results here do not preclude the effects of WWBs on ENSO; indeed, our model is not suitable to study for WWBs and MJO.

Finally, it is worth noting that the result presented here may be model dependent. The robustness of the result needs to be further tested.

C. Future Work

What are the potential implications of this study? If the MM works as an important triggering mechanism for ENSO, then it should have important implications for ENSO prediction. Questions that remain to be addressed are: 1) How predictable is the MM? What are the predictable dynamics of the MM? 2) Can ENSO prediction be improved, particularly during the spring barrier if the MM can be predicted? and 3) Can coupled model predictive skill be improved by suppressing the model's internal variability?

In our noise-filtering experiment, we assume that the noise is additive. To test whether this approach can contaminate our result, we plan to carry out another set of experiments, using the interactive ensemble approach (Kirtman and Shukla, 2002; Kirtman et al., 2004), which do not depend on the linearity assumption. This comparison will lead to better understanding of the role of internal atmospheric variability on ENSO dynamics. But this approach is computationally more expensive, because multiple realizations of AGCM have to been conducted simultaneously and averaged before passing to ocean model at each coupled step.

The model simulation also demonstrates the decadal variation of the relationship between the MM and ENSO. That is, events in both the MM-ENSO and the MM-ONLY groups seem to cluster together. For instance, MM-ENSO dominates in the periods of model years 10-70, 310-330, and 310-400; while there are more ENSO-ONLY events in the periods of model years 90-150 and 330-360 (Fig. 16). We speculate that this phenomenon may be related to the decadal variability of ENSO, and needs to be further investigated.

REFERENCES

Allen, M. and L. Smith, 1997: Optimal filtering in singular spectrum analysis. *Phys. Lett.*, **234**, 419–428.

Balmaseda, M., M. Davey, and D. Anderson, 1995: Decadal and seasonal dependence of enso prediction skill. *J. Climate*, **8**, 2705–2715.

Barnett, T., D. Pierce, M. Latif, D. Dommenget, and R. Saravana, 1999: Interdecadal interactions between the tropics and the midlatitudes in the pacific basin. *Geophys.Res.Lett.*, **26**, 615–618.

Barsugli, J. and D. Battisti, 1998: The basic effects of atmosphere-ocean thermal coupling on midlatitude variability. *J. Atmos. Sci.*, **55**, 477–493.

Battisti, D. A. and A. C. Hirst, 1989: Interannual variability in a tropical atmosphere-ocean model: Influence of the basic state and ocean geometry. *J. Atmos. Sci.*, **46**, 1687–1712.

Bjerknes, J., 1969: Atmospheric teleconnections from the equatorial pacific. *Mon.Wea.Rev.*, **97**, 163–172.

Blanke, B., J. Neelin, and D. Gutzler, 1997: Estimating the effect of stochastic wind stress forcing on enso irregularity. *J. Climate*, **10**, 1473–1486.

Busalacchi, A. and J. O'Brien, 1981: Interannual variability of the equatorial pacific in the 1960's. *J. Geophys. Res.*, **86**, 10,901–10,907.

Cane, M., S. Zebiak, and S. Dolan, 1986: Experimental forecasts of el niño. *Nature*, **321**, 827–832.

Chang, P., 1994: A study of the seasonal cycle of sea surface temperature in the tropical pacific ocean using reduced gravity models. *J. Geophys. Res.*, **99**, 7725–7741.

Chang, P., L. Ji, H. Li, and M. Flügel, 1996: Chaotic dynamics versus stochastic processes in el niño-southern oscillation in coupled ocean-atmosphere models. *Physica D*, **98**, 301–320.

Chang, P., R. Saravanan, L. Ji, and G. Hegerl, 2000: The effect of local sea surface temperature on atmospheric circulation over the tropical atlantic sector. *J. Climate*, **13**, 2195–2216.

Chang, P., R. Saravanan, F. Wang, and L. Ji, 2004: Predictability of linear coupled systems. part ii: An application to a simple model of tropical atlantic variability. *J. Climate*, **17**, 1487–1503.

Chen, D., M. Cane, A. Kaplan, S. Zebiak, and D. Huang, 2004: Predictability of el niño over the past 148 years. *Nature*, **428**, 733–736.

Chen, D., S. Zebiak, A. Busalacchi, and M. Cane, 1995: An improved procedure for el niño forecasting: Implications for predictability. *Science*, **269**, 1699–1702.

Chiang, J. and D. Vimont, 2004: Analogous pacific and atlantic meridional modes of tropical atmosphere-ocean variability. *J. Climate*, **17**, 4143–4158.

Clarke, A. and S. V. Gorder, 1999: On the connection between the boreal spring southern oscillation persistence barrier and the tropospheric biennial oscillation. *J.Climate*, **12**, 610–620.

— 2001: Enso prediction using an enso trigger and a proxy for western equatorial pacific warm pool movement. *Geophy. Res. Lett.*, **28**, 579–582.

Clarke, A. and L. Shu, 2000: Quasi-biennial winds in the far western equatorial pacific phase-locking el niño to the seasonal cycle. *Geophy. Res. Lett.*, **27**, 771–774.

Czaja, A., P. der Varrt, and J.Marshall, 2002: A diagnostic study of the role of remote forcing in tropical atlantic variability. *J. Climate*, **15**, 3280–3290.

Delcroix, T., B. Dewitte, Y. duPenhoat, F. Masia, and J. Picaut, 2000: Equatorial waves and warm pool displacement during the 1992-1998 el niño southern oscillation events: Observation and modeling. *J. Geophys. Res.*, **105**, 26,045–26,062.

Delcroix, T., G. Eldin, M. McPhaden, and A. Morliere, 1993: Effects of westerly wind bursts upon the western equatorial pacific ocean, february-april 1991. *J. Geophys. Res.*, **98**, 16,379–16,385.

Eckert, C. and M. Latif, 1997: Predictability of a stochastically forced hybrid coupled model of el niño. *J. Climate*, **10**, 1488–1504.

Fedorov, A., 2002: The response of the coupled tropical ocean-atmospherie to westerly wind bursts. *Q.J.R.Meteorol.Soc.*, **128**, 1–23.

— 2003: How predictable is el niño? *Bull. Am. Meteorol. Soc.*, **84**, 911–919.

Fink, A. and P. Speth, 1997: Some potential forcing mechanisms of the year-to-year variability of the tropical convection and its intraseasonal (25-70 day) variability. *Int. J. Climatol.*, **17**, 1513–1534.

Flügel, M. and P. Chang, 1996: Impact of dynamical and stochastic processes on the predictability of enso. *Geophys. Res. Let.*, **23**, 2089–2092.

— 1998: Does the predictability of enso depend on the seasonal cycle. *J. Atmos. Sci.*, **10**, 1488–1505.

— 1999: Stochastically induced climate shift of el niño-southern oscillation. *Geophys. Res. Lett.*, **26**, 2473–2476.

Flügel, M., P. Chang, and C. Penland, 2004: The role of stochastic forcing in modulating enso predictability. *J. Climate*, **17**, 3125–3140.

Galanti, E., E. Tziperman, M. Harrison, A. Rosati, and Z. Sirkes, 2003: A study of enso prediction using a hybrid coupled model and the adjoint method for data assimilation. *Mon. Weather Rev.*, **131**, 2748–2764.

Giese, B. and J. Carton, 1999: Interannual and decadal variability in the tropical and midlatitude pacific ocean. *J. Climate*, **12**, 3402–3418.

Giese, B. and D. Harrison, 1991: Eastern equatorial pacific response to 3 composite westerly wind types. *J. Geophys. Res.*, **96**, 3239–3248.

Giese, B., S. Urizar, and N. Fuckar, 2002: Southern hemisphere origins of the 1976 climate shift. *Geophys. Res. Lett.*, **29**, doi: 10.1029/2001GL013268.

Graham, N., 1994: Decadal-scale climate variability in the tropical and north pacific during the 1970s and 1980s: Observations and model results. *Climat. Dyn.*, **10**, 135–162.

Gu, D. and S. Philander, 1997: Interdecadal climate fluctuations that depend on exchanges between the tropics and extratropics. *Science*, **275**, 805–807.

Gutzler, D. and D. Harrison, 1986: The structure and evolution of seasonal wind anomalies over the near-equatorial eastern indian and western pacific oceans. *Mon. Wea. Rev.*, **115**, 169–192.

Hendon, H., B. Liebmann, and J. Glick, 1998: Oceanic kelvin waves and the madden-julian oscillation. *J.Atmos.Sci.*, **55**, 88–101.

Hurrell, J., J. Hack, B. Boville, D. Williamson, and J. Kiehl, 1998: The dynamical simulation of the ncar community climate model version 3. *J. Climate*, **11**, 1207–1236.

Ji, M., A. Leetmaa, and V. Kousky, 1996: Coupled model predictions of enso during the 1980's and the 1990's at the national centers for environmental prediction. *J. Climate*, **9**, 3105–3120.

Jin, F.-F., 1997: An equatorial ocean recharge paradigm for enso. part i: Conceptual model. *J. Atmos. Sci.*, **54**, 811–829.

Jin, F.-F., D. Neelin, and M. Ghil, 1994: El niño on the devil' s staircase: Annual subharmonic steps to chaos. *Science*, **246**, 70–72.

— 1996: El niño/southern oscillation and the annual cycle: Subharmonic frequency locking and aperiodicity. *Physica D.*, **98**, 442–465.

Kalnay, E., M. Kanamitsu, R. Kistler, W. Collins, D. Deaven, L. Gandin, M. Iredell, S. Saha, G. White, J. Woollen, Y. Zhu, A. Leetmaa, B. Reynolds, M. Chelliah, W. Ebisuzaki, W. Higgins, J. Janowiak, K. Mo, C. Ropelewski, J. Wang, R. Jenne, and D. Joseph, 1996: The ncep/ncar 40-year reanalysis project. *Bull.Amer.Meteorol.Soc.*, **77**, 437–471.

Kaplan, A., M. Cane, Y. Kushnir, A. Clement, M. Blumenthal, and B. Rajagopalan, 1998: Analyses of global sea surface temperature 1856-1991. *J. Geophys. Res.*, **103C**, 18,567–18,589.

Keen, R., 1982: The role of cross-equatorial cyclone pairs in the southern oscillation. *Mon. Wea. Rev.*, **110**, 1405–1416.

— 1988: Equatorial westerly and the southern oscillation. *U.S. TOGA western Pacific air-sea interaction workshop*, R. Lukas and P. Webster, eds., U.S. TOGA Rep. USTOGA-8, Univ. Corp. of Atmos. Res., Honolulu, 121–140.

Kerr, R., 1998: Does a global-girdling disturbance jigger el niño? *Science*, **285**, 322–323.

Kessler, W., 2002: Is enso a cycle or a series of events? *Geophys. Res.Lett.*, **29(23)**, doi:10.1029/2002GL015924.

Kessler, W. and R. Kleeman, 2000: Rectification of the madden-julian oscillation into the enso cycle. *J. Climate*, **13**, 3560–3575.

Kessler, W., M. McPhaden, and K. Weickmann, 1995: Forcing of intraseasonal kelvin waves in the equatorial pacific. *J. Geophys. Res.*, **100**, 10,613–10,631.

Kiehl, J., J. Hack, G. Bonan, B. Boville, D. Williamson, and P. Rasch, 1998: The national center for atmospheric research community climate model: Ccm3. *J. Climate*, **11**, 1131–1149.

Kirtman, B., K. Pegion, and S. Kinter, 2004: Internal atmospheric dynamics and climate variability. *J. Atmos. Sci*, in press.

Kirtman, B. and P. Schopf, 1998: Decadal variability in enso predictability and prediction. *J. Atmos.Sci.*, **11**, 2804–2822.

Kirtman, B. and J. Shukla, 2002: Interactive coupled ensemble: A new coupling strategy for cgcms. *Geophys.Res.Lett.*, **29**, doi: 10.1029/2002GL014834.

Kleeman, R., J. McCreary, and B. Klinger, 1999: A mechanism for generating enso decadal variability. *Geophys.Res.Lett.*, **24**, 1743–1746.

Kleeman, R. and A. Moore, 1997: A theory for the limitation of enso predictability due to stochastic atmospheric transients. *J. Atmos.Sci.*, **54**, 753–767.

Landsea, C. and J. Knaff, 2000: How much skill was there in forecasting the very strong 1997-98 el niño. *Bull. AM. Meteorol. Soc.*, **81**, 2107–2119.

Latif, M., D. Anderson, T. Barnett, M. Cane, R. Kleeman, A. Leetmaa, J. O'Brien, A. Rosati, and E. Schneider, 1998: A review of the predictability and prediction of enso. *J. Geophys. Res.*, **103**, 14,375–14,393.

Latif, M. and T. Barnett, 1994: Causes of decadal climate variability over the north pacific and north america. *Science*, **266**, 634–637.

Lau, K.-M., 1985: Elements of a stochastic dynamical theory of the long-term variability of the el niño-southern oscillation. *J. Atmos. Sci.*, **42**, 1552–1558.

Lau, K.-M. and P. Chan, 1986: The 40-50 day oscillation and the el niño-southern oscillation. *Bull. Amer. Meteor. Soc.*, **67**, 533–534.

— 1988: Intraseasonal and interannual variations of tropical convection: A possible link between 40-50 day oscillation and enso. *J. Atmos. Sci.*, **45**, 506–521.

Lau, K.-M., C.-P. Chang, and P. Chan, 1986: Short-term planetary-scale interactions over the tropics and midlatitudes. part ii: Winter monex period. *Mon. Wea. Rev.*, **111**, 1372–1388.

Lim, H. and C.-P. Chang, 1981: A theory for midlatitude forcing of tropical motion during the winter monsoon. *J. Atmos. Sci.*, **38**, 2377–2392.

Luther, D., D. Harrison, and R. Knox, 1983: Zonal winds in the central equatorial pacific and el niño. *Science*, **222**, 327–330.

Madden, R. and P. Julian, 1972: Description of global-scale circulation cells in the tropics with a 40-50 day period. *J. Atmos. Sci.*, **28**, 1109–1123.

— 1994: Observations of the 40-50-day tropical oscillation - a review. *Mon. Wea. Rev.*, **122**, 814–837.

McPhaden, M., 1999: Genesis and evolution of the 1997-1998 el niño. *Science*, **283**, 950–954.

McPhaden, M. and X. Yu, 1999: Equatorial waves and the 1997-1998 el niño. *Geophys.Res.Lett.*, **26**, 2961–1964.

Moore, A. and R. Kleeman, 1999a: The nonnormal nature of el niño and intraseasonal variability. *J. Climate*, **12**, 2965–2982.

— 1999b: Stochastic forcing of enso by the intraseasonal oscillation. *J. Climate*, **12**, 1199–1220.

Neelin, J., D. Battisti, A. Hirst, F.-F. Jin, Y.Wakata, T. Yamagata, and S. Zebiak, 1999: Enso theory. *J. Geophys. Res.*, **103**, 14,261–14,290.

Penland, C., 1996: A stochastic model of indopacific sea surface temperature anomalies. *Physica D.*, **98**, 534–558.

Penland, C., M. Flügel, and P. Chang, 2000: Identification of dynamical regimes in an intermediate coupled ocean-atmosphere model. *J. Climate*, **13**, 2105–2115.

Penland, C. and P. Sardeshmukh, 1995: The optimal growth of tropical sea surface temperature anomalies. *J. Climate*, **8**, 1999–2024.

Perigaud, C. and C. Cassou, 2000: Importance of oceanic decadal trends and westerly wind bursts for forecasting el niño. *Geophys.Res.Lett.*, **27**, 389–392.

Philander, S., 1981: The response of equatorial oceans to a relaxation of the trade winds. *J. Phys. Oceanogr.*, **11**, 176–189.

— 1985: El niño and la niña. *J. Atmos. Sci.*, **42**, 2652–2662.

— 1990: *El Niño, La Niña, and the Southern Oscillation*. Academic Press, San Diego, CA.

— 1999: A review of tropical ocean-atmosph ere interactions. *Tellus*, **51A-B**, 71–90.

Philander, S. and A. Fedorov, 2003: Is el niño sporadic or cyclic. *Annu.Rev.Earth Planet.Sci.*, **31**, 579–594.

Pierce, D., T. Barnett, and M. Latif, 2000: Connections between the pacific ocean tropics and midlatitudes on decadal timescales. *J. Climate*, **13**, 1173–1194.

Rasmusson, E. and T. Carpenter, 1982: Variations in tropical sea surface temperature and surface wind fields associated with the southern oscillation/el niño. *Mon. Weather Rev.*, **110**, 354–384.

Rasmusson, E., X. Wang, and C. Ropelewski, 1990: The biennial component of enso variability. *J.Mar.Systems*, **1**, 71–96.

Reynolds, R. and T. Smith, 1994: Improved global sea surface temperature analyses using optimum interpolation. *J. Climate*, **7**, 929–948.

Rogers, J., 1981: The north pacific oscillation. *J. Climatol.*, **1**, 39–57.

Roulston, M. and J. Neelin, 2000: The response of an enso model to climate noise, weather noise and intraseasonal forcing. *Geophys. Res. Lett.*, **27**, 3723–3726.

Saravanan, R., 1998: Atmospheric low frequency variability and its relationship to midlatitude sst variability: Studies using the ncar climate system model. *J. Climate*, **11**, 1386–1404.

Seager, R., S. Zebiak, and M. Cane, 1988: A model of the tropical pacific sea surface temperature climatology. *J.Geophys.Res.*, **93(C2)**, 1265–1280.

Servain, J., I. Wainer, J. WcCreary, and A. Dessier, 1999: Relationship between the equatorial and meridional modes of climatic variability in the tropical atlantic. *Geophys.Res.Lett.*, **26**, 485–488.

Slingo, J., D. Rowell, K. Sperber, and F. Nortley, 1999: On the predictability of the interannual behavior of the madden-julian oscillation and its relationship with el niño. *Q.J.R.Meteorol.Soc.*, **125**, 583–560.

Smith, T., R. Reynolds, R. Livezey, and D. Stokes, 1996: Reconstruction of historical sea surface temperatures using empirical orthogonal functions. *J. Climate*, **9**, 1403–1420.

Suarez, M. and P. Schopf, 1988: A delayed action oscillator for enso. *J.Atmos.Sci.*, **45**, 3283–3287.

Sura, P. and C. Penland, 2002: Sensitivity of a double-gyre model to details of stochastic forcing. *Ocean Modelling*, **4**, 327–345.

Thompson, C. and D. Battisti, 2000: A linear stochastic dynamical model of enso. part i: Model development. *J. Climate*, **13**, 2818–2832.

— 2001: A linear stochastic dynamical model of enso. part i: Analysis. *J. Climate*, **14**, 445–466.

Torrence, C. and G. Compo, 1998: A practical guide to wavelet analysis. *Bull. Amer. Meteor. Soc.*, **79**, 61–78.

Tourre, Y. and W. White, 1995: Enso signals in global upper-ocean temperature. *J. Phys.Oceanogr.*, **25**, 1317–1332.

Tziperman, E., M. Cane, S. Zebiak, Y. Xue, and B. Blumenthal, 1998: Locking of el niño's peak time to the end of the calendar year in the delayed oscillator picture of enso. *J. Climate*, **11**, 2191–2199.

Vallis, G., 1988: Conceptual models of el niño and the southern oscillation. *J. Geophys. Res.*, **93**, 13,979–13,991.

Venzke, S., M. Allen, R. Sutton, and D. Rowell, 1999: The atmospheric response over the north atlantic to decadal changes in sea surface temperature. *J. Climate*, **12**, 2562–2584.

Vimont, D., D. Battisti, and A. Hirst, 2001: A seasonal connection between the tropics and mid-latitudes. *Geophy.Res.Lett.*, **28**, 3923–3926.

— 2002: Pacific interannual and interdecadal equatorial variability in a 1000-yr simulation of the csiro coupled general circulation model. *J.Climate*, **15**, 160–178.

— 2003a: The seasonal footprinting mechanism in the csiro general circulation models. *J.Climate*, **16**, 2653–2667.

Vimont, D., J. Wallace, and D. Battisti, 2003b: The seasonal footprinting mechanism in the pacific: Implications for enso. *J.Climate*, **16**, 2668–2675.

von Storch, H., G. Bürger, R. Schnur, and J. von Storch, 1995: Principal oscillation patterns. *J. Climate*, **8**, 377–400.

Wang, B., 1995: Interdecadal changes in el niño onset in the last four decades. *J.Climate*, **8**, 267–285.

Wang, B. and S. An, 2002: A mechanism for decadal changes enso behavior: Roles of background wind changes. *Clim. Dyn.*, **18**, 475–486.

Wang, B., A. Barcilon, and Z. Fang, 1999: Stochastic dynamics of el niño-southern oscillation. *J.Atmos.Sci.*, **56**, 5–23.

Wang, B., R. Wu, R. Lukas, and S.-I. An, 2001: A possible mechanism for enso turnabouts. *Dynamics of Atmospheric and Oceanic Circulations and Climate-Celebration of the 80th Birthday of Prof. ZHU Baochen*, T. I. of Atmospheric Physics of Chinese Academy of Sciences, ed., China Meteorlogical Press, 552–578.

Weiss, J. and J. Weiss, 1999: Quantifying persistence in enso. *J. Atmos. Sci.*, **56**, 2737–2760.

Woolnough, S., J. Slingo, and B. Hoskins, 2000: The relationship between convection and sea surface temperature on intraseasonal timescales. *J. Climate*, **13**, 2086–2104.

Yasunari, T., 1985: Zonally propagating modes of the global west circulation associated with the southern oscillation. *J. Meteor. Soc.*, **63**, 1013–1029.

— 1990: Impact of indian monsoon on the coupled atmosphere/ocean system in the tropical pacific. *Meteor. Atmos. Phys*, **44**, 29–41.

Yeh, S., J. Jhun, I. Kang, and B. Kirtman, 2004: The decadal enso variability in a hybrid coupled model. *J. Climate*, **17**, 1225–1238.

Yu, L. and M. Rienecker, 1998: Evidence of an extratropical atmospheric influence during the onset of the 1997-98 el niño. *Geophys.Res.Lett.*, **25**, 3537–3540.

Yu, L., R. Weller, and W. Liu, 2003: Case analysis of a role of enso in regulating the generation of westerly wind bursts in the western equatorial pacific. *J. Geophys. Res.*, **108(C4)**, doi:10.1029/2002JC001498.

Zebiak, S., 1989: On the 30-60 day oscillation and the prediction of el niño. *J.Climate*, **2**, 1381–1387.

Zebiak, S. and M. Cane, 1987: A model el niño-southern oscillation. *Mon. Weather Rev.*, **115**, 2262–2278.

Zhang, C., H. Hendon, W. Kessler, and A. Rosati, 2001: A workshop on the mjo and enso. *Bull. Amer. Meteor. Soc.*, **82**, 971–976.

Zhang, L., M. Flügel, and P. Chang, 2003: Testing the stochastic mechanism mechanism for low-frequency variations in enso predictability. *Geophys. Res. Lett.*, **30**, doi:10.1029/2003GL017505.

Zhang, Y., J. Wallace, and D. Battisti, 1997: Enso-like interdecadal variability: 1900-93. *J.Climate*, **10**, 1004–1020.

VITA

Li Zhang received her B.S. degree in atmospheric science from Beijing University in July, 1996. Following graduation she worked for four years in the National Marine Environmental Forecasting Center. She then went to the Texas A&M University to pursue her Ph.D. degree in oceanography, and received her Ph.D. in August, 2005. She can be reached at Department of Oceanography, Texas A&M University, College Station, TX 77843-3146.